5-2021

NON-CONTACT TECHNIQUES FOR HUMAN VITAL SIGN DETECTION AND GAIT ANALYSIS

Farnaz Foroughian
Electrical Engineering and Computer Science Department, fforoug1@vols.utk.edu

To the Graduate Council:

I am submitting herewith a dissertation written by Farnaz Foroughian entitled "NON-CONTACT TECHNIQUES FOR HUMAN VITAL SIGN DETECTION AND GAIT ANALYSIS." I have examined the final electronic copy of this dissertation for form and content and recommend that it be accepted in partial fulfillment of the requirements for the degree of Doctor of Philosophy, with a major in Electrical Engineering.

Aly E. Fathy, Major Professor

We have read this dissertation and recommend its acceptance:

Hairong Qi, Ozlem Kilic, Jared M. Porter

Accepted for the Council:

Dixie L. Thompson

Vice Provost and Dean of the Graduate School

(Original signatures are on file with official student records.)

NON-CONTACT TECHNIQUES FOR HUMAN VITAL SIGN DETECTION AND GAIT ANALYSIS

A Dissertation Presented for the
Doctor of Philosophy
Degree
University of Tennessee, Knoxville

Farnaz Foroughian
May 2021

Dedication

To my parents, Fereydun Foroughian and Fariba Ghayedan, my husband, Shahram Hatefi Hesari, and my sister and brother, Faranak and Faraz Foroughian because of their support and encouragement.

ACKNOWLEDGEMENTS

I take this opportunity to extend my sincere gratitude and appreciation to all those who made this Ph.D. dissertation possible.

Foremost, I would like to express my heartfelt appreciation to my advisor Prof. Aly E. Fathy for the continuous support of my Ph.D. study and research, for his patience, motivation, enthusiasm, and immense knowledge. Whenever I lost my way, he was always there to put me right back on track. On the academic level, Prof. Fathy taught me fundamentals of conducting scientific research, how to work through a problem, and the art of academic writing. I am indebted to him for all my accomplishments during my graduate studies, and could not have imagined having a better advisor and mentor for my Ph.D. study. Besides my advisor, I would like to thank the rest of my dissertation committee members (Prof. Hairong Qi, Prof. Ozlem Kilic, and Dr. Jared M. Porter) for their great support and invaluable advice.

I would like to express my deepest gratitude to my family and friends, for their warm love, continued patience, and unconditional support. I am grateful to my ever-supporting mother and father, who have provided me through moral and emotional support throughout my life. I cannot stress enough the support my husband Shahram Hatefi Hesari provided during the difficult times we had to endure together to make all this possible. This dissertation would not have been possible without his love, and sacrifices. I am also so thankful to my friends Melika Roknsharifi, Samaneh Morovati, Ava Hedayatipour, Shaghayegh Aslanzadeh, Razieh Kaviani, Minoo Oliaee, Ramin Nabati, and Ramin Arvin.

I would also like to thank my lab mates and other academic collaborators for their continued support in various research projects. I would specially mention my former lab partners Ahmadreza Ghahremani, Lingyun Ren, Haofei Wang, MatthewRichardson, Fugui Qi, Wei Ren, Farhan Quaiyum, and Kellen Oleksak, and current colleagues Toan Vo Dai, Tsotne Kvelashvili, Chandler Bauder, Abdel Karim Moadi, Marvin Joshi, and Peter Alley with whom I had worked on a number of successful projects. Special thanks to Dr. J. E. Piou from the MIT Lincoln Laboratory for their support with the signal processing algorithm development utilized in this work.

I am also grateful to my industrial collaborators. More specifically, I spent the summer and fall of 2020 working at Intel as a RF/EMC Engineer Intern where I had the opportunity to work with fantastic researchers and mentors (Ana M. Yepes, Pujitha Davuluri, Steven G. Gaskill, and Jaejin Lee), and would like to thank them for their significant impact in my growth in this field.

Thanks are also due to MaXentric Technologies for their initial financial support for this project without which I would not have been able to undertake my research endeavors. Specifically, thanks to Paul Theilmann and Bardia Ghajari for their support during various stages of my Ph.D. with word substitutes.

ABSTRACT

Human vital signs including respiratory rate, heart rate, oxygen saturation, blood pressure, and body temperature are important physiological parameters that are used to track and monitor human health condition. Another important biological parameter of human health is human gait. Human vital sign detection and gait investigations have been attracted many scientists and practitioners in various fields such as sport medicine, geriatric medicine, bio-mechanic and bio-medical engineering and has many biological and medical applications such as diagnosis of health issues and abnormalities, elderly care and health monitoring, athlete performance analysis, and treatment of joint problems. Thoroughly tracking and understanding the normal motion of human limb joints can help to accurately monitor human subjects or patients over time to provide early flags of possible complications in order to aid in a proper diagnosis and development of future comprehensive treatment plans.

With the spread of COVID-19 around the world, it has been getting more important than ever to employ technology that enables us to detect human vital signs in a non-contact way and helps protect both patients and healthcare providers from potentially life-threatening viruses, and have the potential to also provide a convenient way to monitor people health condition, remotely. A popular technique to extract biological parameters from a distance is to use cameras. Radar systems are another attractive solution for non-contact human vital signs monitoring and gait investigation that track and monitor these biological parameters without invading people privacy.

The goal of this research is to develop non-contact methods that is capable of extracting human vital sign parameters and gait features accurately.

To do that, in this work, optical systems including cameras and proper filters have been developed to extract human respiratory rate, heart rate, and oxygen saturation. Feasibility of blood pressure extraction using the developed optical technique has been investigated, too. Moreover, a wideband and low-cost radar system has been implemented to detect single or multiple human subject's respiration and heart rate in dark or from behind the wall. The performance of the implemented radar system has been enhanced and it has been utilized for non-contact human gait analysis. Along with the hardware, advanced signal processing schemes have been enhanced and applied to the data collected using the aforementioned radar system. The data processing algorithms have been extended for multi-subject scenarios with high accuracy for both human vital sign detection and gait analysis. In addition, different configurations of this and high-performance radar system including mono-static and MIMO have been designed and implemented with great success. Many sets of exhaustive experiments have been conducted using different human subjects and various situations and accurate reference sensors have been used to validate the performance of the developed systems and algorithms.

TABLE OF CONTENTS

LIST OF TABLES

LIST OF FIGURES

CHAPTER ONE
INTRODUCTION AND MOTIVATION

1.1 Human Vital Signs

Human physiological factors of respiratory rate (RR), heart rate (HR), oxygen saturation (SpO_2), blood pressure (BP), and body temperature (BT) are used for health assessment and are known as human vital signs. There are conventional and traditional contact methods to monitor these factors such as electrocardiography (ECG), that uses contact electrodes on the surface of human body, finger clip or earlobe-clip pulse sensors, belt sensors, photoplethysmography (PPG), wrist or cuff blood pressure sensors and etc. to measure and monitor the vital signs. Figure 1.1 shows some of these conventional methods. However, these sensors need to be in touch with human body to estimate and measure vital signs parameters. In this way, they cause discomfort and epidermal stripping for example in daily elderly care. Especially, in the situations when the patient has burn injuries or significant wounds, or very sensitive skin such as premature infants in intensive care units, it is almost impossible to use these contact techniques to monitor vital signs. Moreover, there are specific situations such as war or earthquake that there are alive people under the debris and are not accessible to contact these sensors to their bodies. Therefore, we need to emphasize here the importance of non-contact human vital sign techniques that can be utilized in various scenarios. In this work our focus is to extract human vital signs including RR, HR, SpO_2, and BP. Basically, there are two major non-contact techniques we are addressing in this work for human vital sign detection: camera-based imaging photoplethysmography (iPPG) and radar (radio detection and ranging) techniques.

Figure 1.1 Examples of contact sensors for human vital sign monitoring.

In the first one, vital signs can be measured using cameras. iPPG is an optical method that measures the small changes in skin color that are the result of changes in blood volume in arteries and capillaries caused by the cardiac cycle. iPPG utilizes imaging devices such as cameras to measure these changes and provide information on cardiovascular status. iPPG is based on the principle that blood absorbs more light than its surrounding tissues. Therefore, by measuring variations in reflected light, as caused by variations in blood volume, we may be able to ascertain vital signs. Hence, variations in blood volume affect light transmission/reflection [1.1] and are related to HR and RR. In [1.2], the feasibility of HR and RR detection using a simple webcam was demonstrated.

Moreover, a method has been developed to measure SpO_2 at optical frequencies using two cameras under regular lighting conditions [1.1]. Two cameras capture two PPG signals simultaneously at two different wavelengths, and these signals are successfully utilized to measure SpO_2.

The second non-contact method is radar technique. In this way, an electromagnetic signal is sent to a target using radar transmitter, reflects back from the target, and is received by radar receiver.

For radars, several accurate non-contact methods using various types of Doppler radar have been proposed recently for the remote triage monitoring of HR and RR [1.3-1.28].

1.2 Human Gait Analysis

Another important parameter of human health is human gait. Human gait analysis is very important and is investigated in this work. The targeted biological and medical applications of this work are diagnosis of health issues and abnormalities [1.29-1.31], elderly care and

health monitoring [1.32], athlete performance analysis [1.33], and treatment of joint problems.

There are many methods for human gait analysis. There are many types of sophisticated equipment have been in the market to monitor, track, record, and analyze patients' motions like spinal cord analysis machines, adaptive motion trainers, and stretch trainers. There are also ultrasonic systems in wearable instrumented shoes [1.34], multiple cameras for motion sensing and analysis, pressure sensors in floor mats or shoes.

However, these types of equipment are not widely used because they are either invasive (required to be imbedded in the patient's body) or need contact (require touching the patient), and can often be expensive or hard to setup. For example, multi-camera systems are very expensive to setup, require line of sight and huge data storage, and intrude subjects' privacy. Ultrasound techniques have limited range and usually need long processing time. In use of pressure sensors, we need individual sensors for each organ, which makes it very inconvenient to wear all. Floor mat sensors are contact methods that are able to analyze only lower body parts (lower legs) and have limited ranges depend on the size of the mat. Therefore, there is a need to employ a non-contact and non-invasive method for human gait analysis that is not very expensive and can be used long-term, without invading the privacy. Considering these properties, radar techniques are very attractive candidates. Radars are non-invasive, non-contact methods that can cover long range, are used in indoor and outdoor environment, and are relatively low cost.

In this work we focus on extracting the gait features from a moving subject in normal walking scenarios using radar techniques. However, among different gait parameters

including step length, stance/swing length, step time, cadence, average speed, joint angles, force on muscles, body posture, and joint velocities, the focus of this work is on extraction of joint velocities that has clinical, sports, and security applications [1.35].

1.3 Radar Architectures

Several radar technologies have been applied already with some success to extract human vital signs and various gait features of human subjects, including the impulse radar [1.17], the continuous-wave (CW) radar [1.36-1.39], the frequency-modulated continuous-wave (FMCW) radar [1.40], [1.22], and stepped-frequency continuous-wave (SFCW) radar [1.24-1.28]. However, the CW radar system does not provide range information of the subjects, which limits its application in subject detection. Although, CW radar using dual frequency is capable of estimating the target's direction-of-arrival, it is still susceptible to multipath effects. On the other hand, it is relatively expensive and complicated to implement wideband FMCW and pulse compression radars. Alternatively, ultra-wideband (UWB) impulse Doppler radar has numerous advantages, such as relatively low proto type cost, less power consumption, and high-resolution range profile (HRRP) using a range–time–frequency representation. UWB impulse radar transmits a wideband signal, such as a narrow pulse in time domain, providing both range and accurate Doppler information of the target. However, the transmitted power of UWB radar is limited and is accompanied by relatively high noise accumulated over its wideband causing a low signal-to-noise ratio (SNR), making it difficult to detect. Additionally, UWB impulse radar requires high-speed analog-to-digital converters (ADCs), which inevitably increases its complexity in system design and hardware cost.

Alternatively, FMCW radar, which overcomes both the drawbacks of CW and UWB impulse radars, can be used [1.40], [1.22]. Since it transmits a CW signal, a relatively high power can be transmitted with high SNR and without a need for high-speed ADCs. However, it still requires calibration to compensate for the nonlinearities in frequency sweeping [1.41], [1.42]. On the other hand, SFCW radar has been utilized for short-range vital sign monitoring. Compared with a CW radar system, SFCW radar is capable of localization, thereby allowing for multiple subjects monitoring in real time. Generally, SFCW can be designed to have similar performance as UWB pulses in the frequency domain; hence should provide comparable capabilities as UWB systems. However, it utilizes low-speed ADCs because of its narrow instantaneous bandwidth. Furthermore, some of its frequencies can be skipped or even randomly selected, which enables compressive sensing implementation for even faster detection [1.28]. SFCW transmits relatively long duration signals; hence, their received signals are significantly stronger than UWB radar and should have higher SNRs in vital signs detection. Furthermore, compared with FMCW radar, it is easier to calibrate signal distortion caused by any imperfection of the SFCW radar system hardware. In this work, we develop a high-performance SFCW radar system for both human vital sign detection and gait analysis purposes.

1.4 Organization of Dissertation

In Chapter Two, we develop a camera-based iPPG system for human vital sign detection including RR, HR, and SpO_2. However, the feasibility of BP extraction using the aforementioned iPPG system is investigated and initial results is demonstrated. Then, we investigate human vital sign detection using SFCW radar system and a comparison study

of non-contact human vital sign detection using SFCW radar system and IPPG in different experimental scenarios is shown. At the end, mono-static and real-time SFCW radar systems are developed.

In Chapter Three, we investigate human gait analysis by addressing the main challenges of non-contact human gait analysis and the existing reports and works.

In Chapter Four, we explain the development a high-performance SFCW radar system required for human gait analysis, step by step.

Chapter Five is dedicated to signal processing algorithm developed for accurate human gait analysis and extraction of human gait features in detail.

In Chapter Six, the experimental setup for human gait analysis using high-performance SFCW radar system and the developed signal processing schemes are explained and the results for single- and multi-subject scenarios are shown. Moreover, in this chapter, the results are compared with other major existing works and several problem and challenges are addressed.

In Chapter Seven, we extend the high-performance SFCW radar system in conjunction with the signal processing algorithm employed for human gait analysis to human vital sign detection. This investigation is then extended to multi-subject vital sign detection. Afterwards, at the end of this chapter, multi-input multi-output (MIMO) SFCW radar system is developed and combination methods is discussed.

Finally, Chapter Eight concludes this work, shows the accomplishments, and futuristic view of this work.

CHAPTER TWO
NON-CONTACT HUMAN VITAL SIGN DETECTION

With the spread of the coronavirus, it is more important than ever before to explore techniques to measure various vital signs without touching the patient. Non-contact vital sign measurement techniques can help protect both patients and medical professionals from potentially life-threatening viruses, and have the potential to also provide a fast-screening solution to test masses of people. A popular technique to extract vital signs from a distance is to use cameras. However, in cases that the light is not adequate, or we cannot see the patient (e.g. when patient is behind the wall), or the privacy is important camera is not a suitable technique for human vital sign detection. Under these conditions, radar systems are attractive alternatives that can be utilized to extract human vital signs from a far distance, in dark, or from behind a wall.

In this chapter, first we talk about detection of vital signs using optical techniques and the specific vital signs that are detectable using cameras. Then, we explain radar techniques to retrieve human vital signs in detail.

2.1 Human Oxygen Saturation Detection using Optical Technique

2.1.1 Human Oxygen Saturation (SpO_2) Detection

As mentioned before, one of the most important human biological parameters or vital signs is oxygen saturation (SpO_2) which shows the level of oxygen in blood and is a risk factor for chronic diseases of circulatory and respiratory system.

Traditionally, SpO_2 is measured in a non-invasive but contact method using conventional pulse oximeters which are clipped generally to a subject's fingers or earlobes. This non-

invasive method is suitable for many situations. However, there are circumstances where direct skin contact must be avoided, for example patients with serious burns or premature infants. Imaging photoplethysmography (iPPG) has solved this problem. According to photoplethysmography theory, which is based on blood absorption of visible light, the changes of blood in capillaries underneath the skin due to the cardiac pulse can be detected from very small variations in skin color. Visible light imaging devices such as cameras can be used to detect these small changes and extract the PPG signal [2.1].

2.1.2 Detection Method and Challenges

Traditionally, the SpO_2 level, which indicates the intensity of oxygen in blood, can be expressed as

$$SpO_2 = \frac{HbO_2}{HbO_2+Hb} \times 100\% \quad (2.1)$$

where HbO_2 and Hb indicate oxygenated and deoxygenated hemoglobin, respectively. Therefore, according to the above formula, oxygen saturation is defined as the ratio of number of oxygenated hemoglobin to the total number of hemoglobin including oxygenated and deoxygenated ones.

In order to detect oxygen saturation, we need two PPG signals at two different wavelengths. In 2007, Kenneth Humphreys et al., for the first time, demonstrated a non-contact SpO_2 measurement system which detects two PPG signals at two different wavelengths [2.2]. However, passive measurement (i.e. using ambient light) is more practical.

Most pulse oximeters work based on the Beer–Lambert law and the theory of light transmission/reflection to extract SpO_2 from two PPG signals. According to the absorption

spectrum of HbO_2 and Hb displayed in Figure 2.1, if we choose two distinct wavelengths, we will be able to extract SpO_2 using (2.2)

$$SpO_2 = A\frac{I_{AC}^{\lambda_1}/I_{DC}^{\lambda_1}}{I_{AC}^{\lambda_2}/I_{DC}^{\lambda_2}} + B = A.R + B \tag{2.2}$$

Where I_{AC} represents the intensity of the AC signal from the light at two wavelengths caused by pulsation (peak-to-peak value of iPPG signal) and I_{DC} denotes the maximum intensity of two beams of light (average value of iPGG signal). In (2.2), A and B are empirical constants determined by calibration. The two wavelengths should be selected such that the absorption coefficients of HbO_2 and Hb at one of the wavelengths differ greatly, but are approximately equal at the other wavelength.

Conventional finger-clip pulse oximeters usually use 660 nm and 940 nm wavelengths. Although these two wavelengths meet the requirements to extract SpO_2, we cannot use these two wavelengths for iPPG based method which uses two cameras since the reflected light from the skin at these two wavelengths is very weak and we need to consider camera response. Therefore, we need to select two other wavelengths. In [1.1], Lingqin Kong and et al. used 520 nm and 660 nm filters for their experiments. However, one of the limitations of using a 660 nm filter is that the PPG signal at this wavelength is weak and noisy. The noise source of the 660 nm signal is not easy to predict. One reason is that the color of blood is red, which is close to 660 nm. Thus, the reflected signal from the blood is very strong, on the other hand, the variation of SpO_2 signal at 660 nm is very weak.

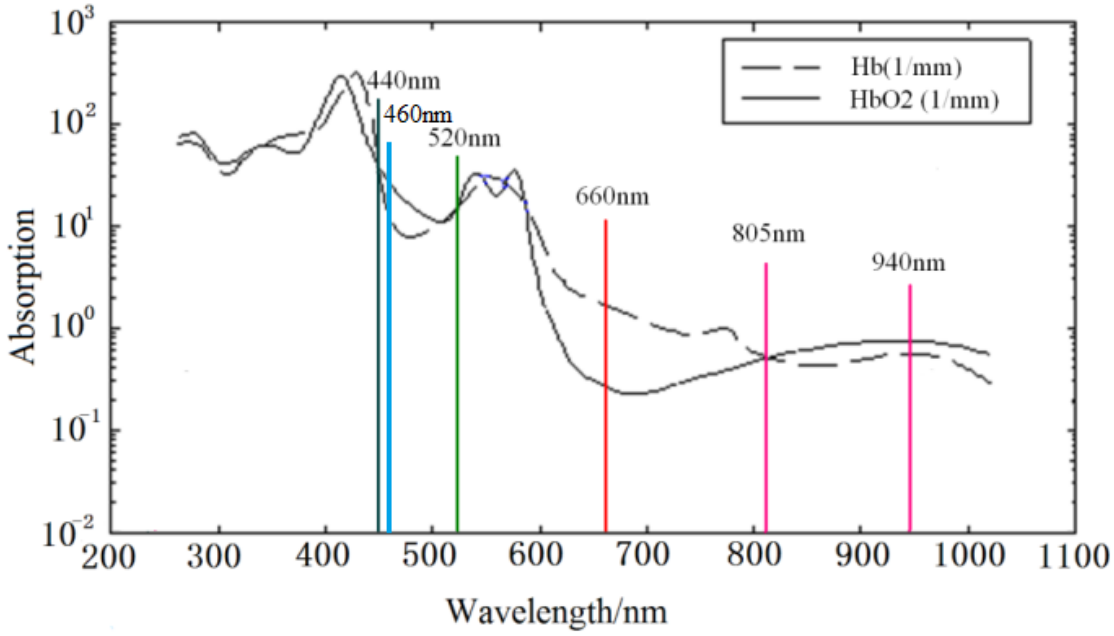

Figure 2.1 The absorption spectrum of HbO2 and Hb [1.1].

The weak signal implies that even small noise sources will greatly reduce the signal to noise ratio of a measurement. Moreover, sun light has a very strong 660 nm component, overwhelming the PPG signal. These limitations make the 660 nm filter an impractical choice for all but the most controlled environments. Thus, we decided to use a 460 nm filter instead of 660 nm filter. Therefore, we used two iPPG signals one at 520 nm and the other at 460 nm wavelengths to measure oxygen saturation. Figure 2.1 shows the absorption spectrum of HbO_2 and Hb.

As it is clear from Figure 2.1, the absorption spectrums of HbO_2 and Hb have the same values at the wavelength of 520 nm, while they differ significantly at the wavelength of 460 nm. Therefore, these two wavelengths meet the requirement to be used to calculate SpO_2. Moreover, the reflected light intensity from the skin surface at these two wavelengths is strong enough to be detected by the camera and both wavelengths are immune to the sunlight. Hence, we chose these two new wavelengths to calculate SpO_2.

However, in order to extract calibration coefficients A and B in (2.2) for the new filters (wavelengths), we need to do many experiments under different conditions and with different human subjects with various skin tones and different levels of blood oxygen levels. In this way we need to use a reliable pulse oximeter as a reference sensor or ground truth to be able to extract calibration coefficients.

2.1.3 Experimental Setup and Results

First, in the regular light of the room (standard lab fluorescent lighting), we setup two monochrome CCD cameras (from Imaging Source, model: DMK 23U618) [2.3] with adapters and lenses (from Thorlabs) [2.4], [2.5] each mounted with a narrowband-pass (460

nm and 520 nm) filter (from Omega Optical) [2.6] about one meter from the volunteer. The cameras were focused on the volunteer's face. We selected the area below eyes as the region of interest (ROI). We also used a finger-clip pulse oximeter (BVP sensor) (from TI, model: AFE4490SPO2) [2.7] as a reference. Data was captured from the oximeter and cameras simultaneously. The experiment was run for 20 seconds and video was captured at 40 frames/second. Figure 2.2 shows the experimental setup.

Then, we use an image processing algorithm implemented in MATLAB to extract PPG signals from each video. The algorithm we used first splits the ROI into lots of small regions, each region is 10 × 10 pixels. We average the value of each region and apply a 0.5Hz-5Hz band-pass to the signal. Finally, we summed up the effective signal and obtained the time (PPG) and frequency domain signals. From these PPG signals we are able to detect heart rate and respiratory rate. If we apply a band-pass filter to these PPG signals to remove the respiratory signal, we will obtain two clean PPG signals which are ready for oxygen saturation extraction as shown in Figure 2.3.

In Figure 2.3 we can see the time domain and frequency domain signals after de-noising and band-pass filtering. The red and black traces show the PPG signals at 520 nm and 460 nm, respectively. As we can see from the frequency domain signal, the two PPG signals have the same frequency. Next, we can extract I_{DC} and I_{AC} at each wavelength from the two PPG signals. The DC components are computed as the average value of the PPG signals over the corresponding time periods. The peak-to-peak value extracted from the PPG signal in each cycle shows the AC component, which also varies when the blood saturation remains unchanged, because of heartbeat or pulsation.

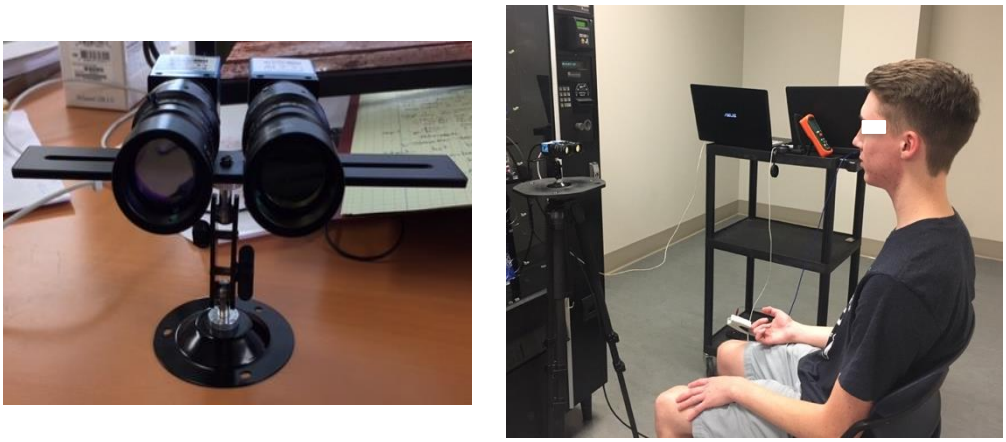

Figure 2.2 (a) Two CCD cameras mounted with the band-pass filters (460-nm and 520-nm filters); (b) Experimental setup in an indoor lab with ambient light.

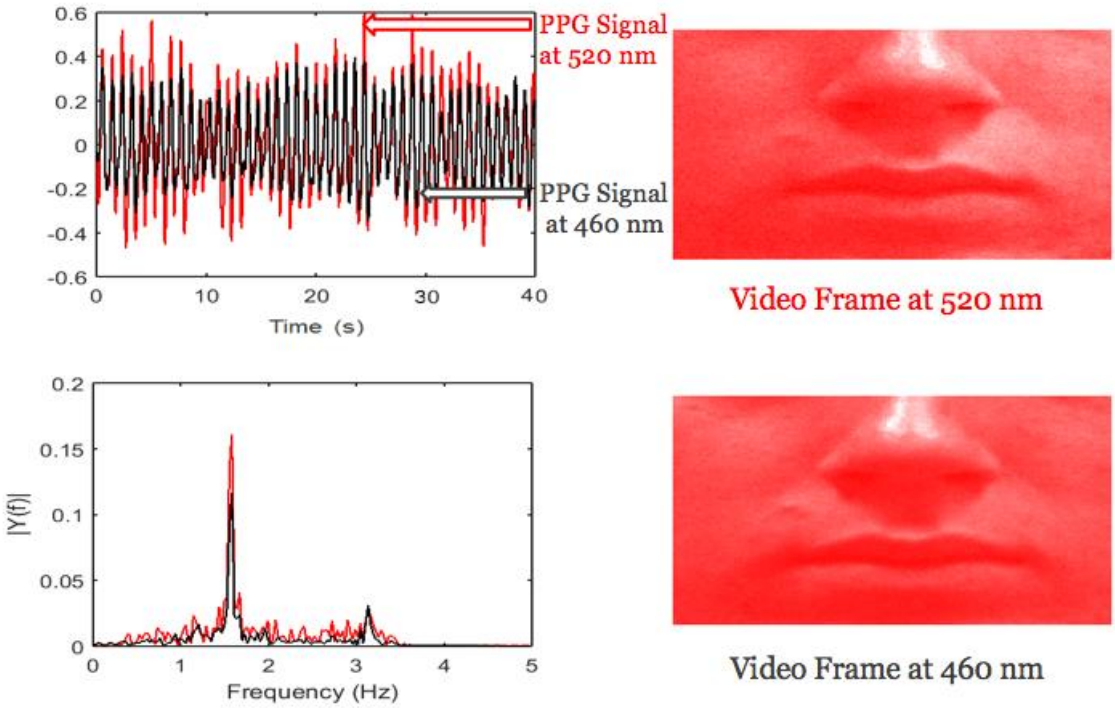

Figure 2.3 The iPPG signals after band pass filtering (top curve), and the spectrum of iPPG signal (bottom curve) [2.8].

In order to accurately extract calibration coefficients (A and B) we need to conduct sets of experiments with a robust population of subjects at different ages and with varying blood oxygen levels measured from a reference sensor. After several groups of breath holding comparison tests with different volunteer subjects in the same environment temperature and light conditions, A and B were extracted.

$$SpO_2 = 128 - 44.R \tag{2.3}$$

The error in ambient light (about 500 lx) is 2% when the subject is at 1-m distance from the two cameras.

2.2 Human Respiratory and Heart Rate Detection using Optical Technique

As explained above, iPPG signal is a variation of the skin color due to the small changes in the blood volume in arteries and capillaries underneath the skin caused by heartbeat and therefore, is proportional to the human pulsation. In fact, the reflected optical signal from the skin has a low-frequency component that slowly varies due to the respiration rate (RR). Meanwhile, its high-frequency component, which shows pronounced change, is related to the blood volume change during the systolic and diastolic phases of the cardiac cycle and therefore, can be used to calculate heart rate (HR).

Although we used two cameras with two different wavelengths to measure human SpO_2, one of the cameras is enough to extract RR and HR. In this case, when we use one camera, the proper wavelength to extract RR and HR using iPPG is 520 nm (green light) due to the blood's absorptivity and skin penetrating ability of the light at this wavelength. In addition, it is not sensitive to the sunlight noise.

2.2.1 Methodology

In order to retrieve RR and HR using optical techniques, like the previous section, we take a video from the face of the human subject using a CCD camera mounted with a proper band-pass filter (520 nm filter). Then we select ROI (the area below the eyes). Basically, there are two major challenges to get a clean iPPG signal from the video:

1. extremely low signal strength of the color-change signal, particularly for darker skin tones and/or under low lighting conditions; and

2. motion artifacts due to an individual's movement in front of the camera.

There are many methods and techniques to overcome these challenges such as DistancePPG [2.9], MRC (Maximum Ratio Combination), weighted averaging, region-based motion tracking algorithm, and Sophia (Skin-Oxygen PPG Image Analysis) [2.10]. However, we can divide all these methods into two major techniques: average-based methods and using independent component analysis (ICA)-based methods. In average-based methods, we take the spatial average from all the pixel intensity within the selected face region, and then filter it for de-noising. On the other hand, in ICA-based methods, we decompose the different camera channels (e.g. red, green, and blue or cyan, orange, and green) into independent source signals and then extract the desired PPG signal from one of these independent sources.

Although ICA-based techniques have shown promising results, they usually have expensive computational cost and therefore much longer processing time due to the implementation of PPG extraction algorithm on multiple channels and signals.

However, for our purposes (extracting RR and HR), taking average of all pixels in the ROI for each frame of the taken video helps in cancelling out the unrelated signal due to the head motion or light changing on the surface of the subject's skin.

Therefore, by plotting these average values vs. time (associated with frame number), we obtain a clean iPPG signal, showing the pulsation. This iPPG signal has two components; the low-frequency component reflects RR (since human RR is between 0.1 Hz and 0.5 Hz), while the high-frequency component shows HR (human HR is between 0.7 Hz and 3 Hz). Therefore, after extracting iPPG signal which is a periodic signal, we apply Fast Fourier Transform (FFT) to this signal to get the spectrum or frequency-domain signal. Afterwards by applying suitable filter we can extract the peaks associated with RR and HR and by multiplying the peak values (in Hz) by 60 we can retrieve RR and HR (in bpm (beat per minute)).

Figure 2.4 shows the spectrum of vital signs including RR and HR from a camera with 520-nm filter when illumination level on the surface of the subject's skin is 500 lx and the results from the contact sensors as references.

As seen from Figure 2.4, the results from camera match well with the contact sensor.

We have summarized the whole procedure of retrieving RR, HR, and SpO_2 in Figures 2.5 to 2.7, and Figure 2.8 shows the pulse sensor as the reference.

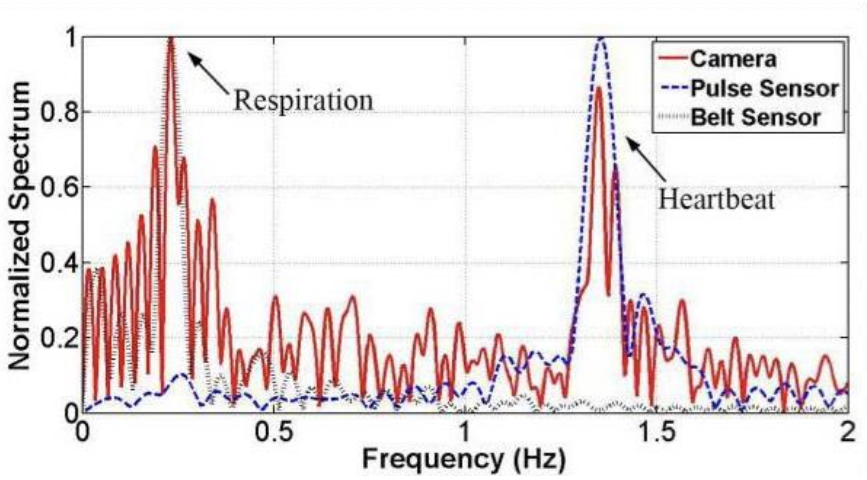

Figure 2.4 Spectrum of vital signs including RR and HR from a camera with a 520-nm filter when illumination level on the surface of the subject's skin is 500 lx and the results from the contact sensors as our reference [2.11].

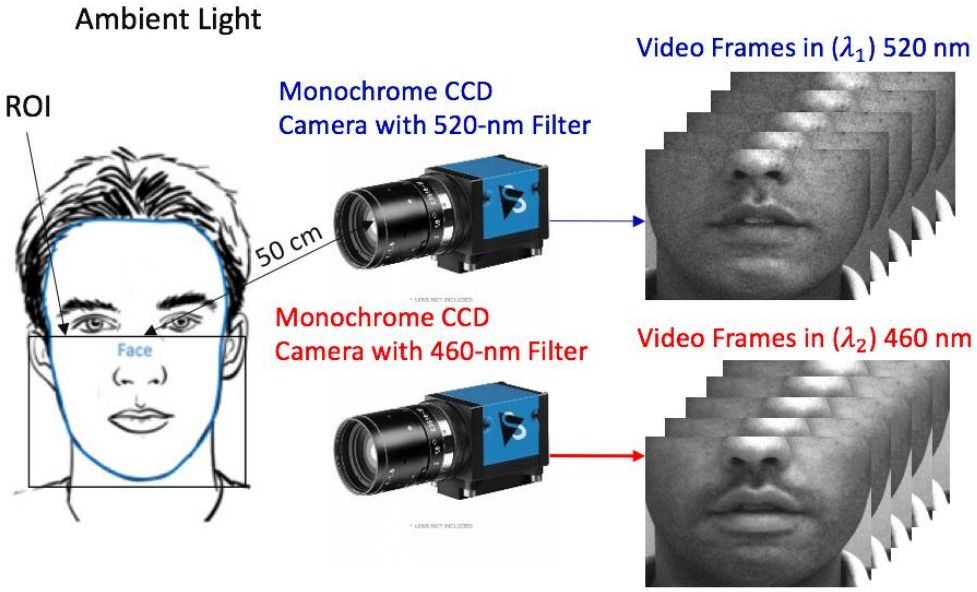

Figure 2.5 The setup to extract iPPG signals for RR, HR, and SpO_2.

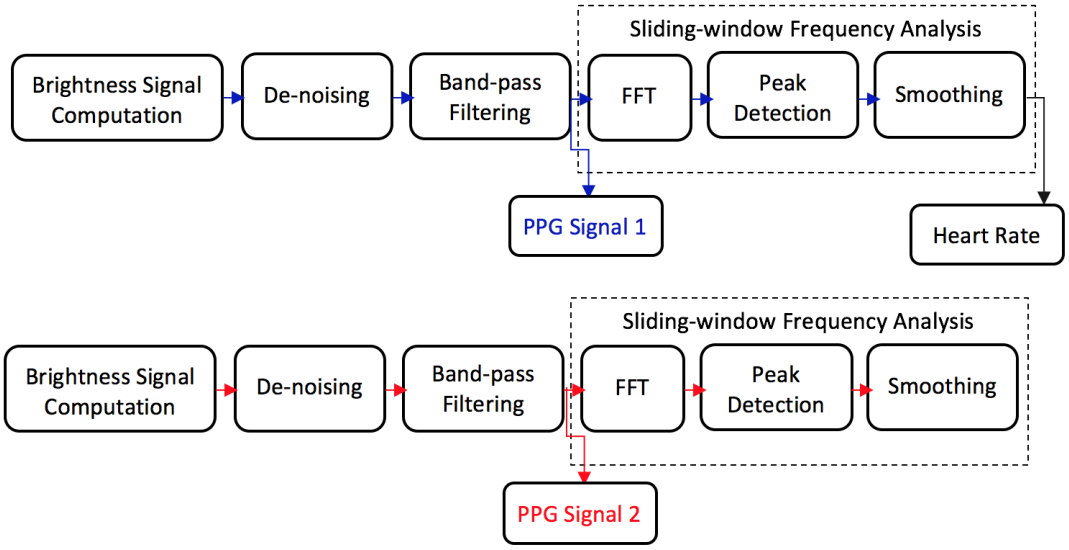

Figure 2.6 Processing pipeline to extract the respiratory rate, heart rate, and oxygen level over time from video sequences of the skin.

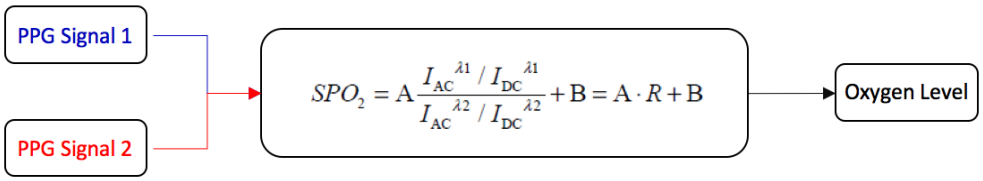

Figure 2.7 Processing to extract the oxygen level over time from the video sequences of the skin.

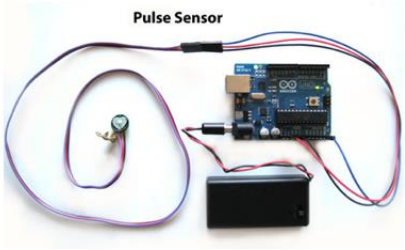

Figure 2.8 Pulse sensor (reference or ground truth).

2.3 Human Blood Pressure Detection using Optical Technique

2.3.1 Blood Pressure Extraction

Recent publications have shown it is possible to estimate the blood pressure (BP) of a patient using optical techniques [2.12], [2.13]. It has been shown that pulse transit time (PTT), or the amount of time it takes a pulse from the heart to travel between two arterial sites, is highly correlated with BP. By monitoring the change in pixel values over time in two areas of the body and applying appropriate averaging and filtering, PTT can be extracted. In this work, PTT was extracted between the face and the palm of the right hand. After proper calibration, PTT can be used along with the calculated calibration coefficient (b) from the following equation to estimate BP, where $\gamma = 0.0174$ (from Dr. Kong, Beijing Institute of Technology):

$$BP = \frac{-2}{\gamma} ln(PTT) + b \tag{2.4}$$

This relationship applies for both diastolic blood pressure (DBP) and systolic blood pressure (SBP). The calibration coefficients for each can be calculated using a fitting method, but due to the limited testing availability in this work, the calibration coefficient was found based on one measurement as an initial test.

An important factor related to the accuracy of these measurements is the frames per second (fps) capability of the camera in use. Because the average PTT between the face and hand is typically very small (as small as tens of milliseconds), a camera with over 100 fps is preferred. In this work, the back camera of the iPhone X is used in order to record video in 1080 p 240 fps. After comparing results between a 100-fps monochrome camera, the iPhone X back camera at 120 fps, and the iPhone X back camera at 240 fps, the 240-fps

camera provided the most consistent results in terms of signal quality under any lighting scenario. The monochrome camera suffered from poor focusing and heavy dependence on lighting. The iPhone X was able to take high quality videos using natural lighting, without the need for an external lighting source.

2.3.2 Experimental Setup and Results

To test the feasibility of the proposed technique, the average PTT's of two subjects are found; one for calibration, and the other one to test the calibration coefficients. This sort of experiments has been conducted by my colleague, Chandler Bouder. In order to extract a subject's PTT, a video is first recorded with the subject's face and hand in-frame for 40 seconds. The subject's blood pressure is taken using a contact sensor directly after the video is taken as a reference. The video is then analyzed by custom MATLAB code to specify the regions of interest. The green channel of each of the regions is then extracted in order to help reduce noise. To help eliminate noise caused by slight movements, rather than taking an overall average pixel value across the whole region, the region is divided into smaller 20 x 20-pixel regions, averaged, filtered, and added back together. The initial results and errors of the estimations are shown in Table 2.1. However, there are improvements that can be done to increase the accuracy of this technique. First, a much larger sample of experiments needs to be run in order to extract unique b and γ coefficient values for both SBP and DBP. By holding γ constant, the difference between the SBP and DBP will always be the same.

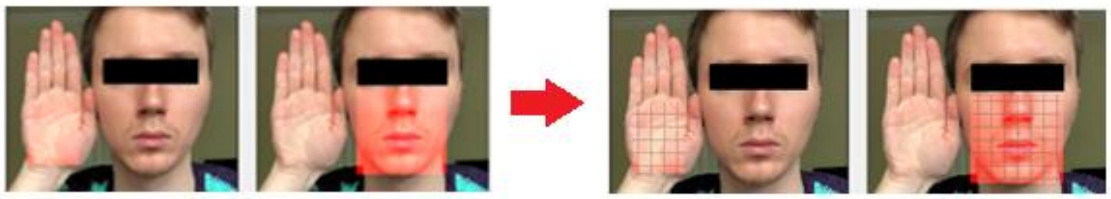

Figure 2.9 Pixel average of two regions of interest, palm and the area in face bellow eyes as ROIs.

Table 2.1 The Calibration Coefficients for Both DBP and SBP

Reference BP	**Estimated BP**	**Avg. PTT**	**% Error SBP**	**% Error DBP**
127/80	121/86	40ms	4.73%	7.5%

Though SBP and DBP have a somewhat linear relationship, this is not always perfect. Blood pressure (SBP – DBP) is also known to vary widely from a person to another.

Another important improvement is including more variables in the model to predict BP. PTT does not have a perfect correlation with BP, and other works have reported including other parameters such as heart rate, age, height, and more [2.14], [2.15]. It has also been reported that using variations in the hue of the video results in more accurate estimations than extracting the green channel [2.16].

There have also been studies using transdermal optical imaging (TOI) technology that allow the separation of re-emitted light from hemoglobin from that of melanin [2.17]. This would greatly reduce the risk of affecting the accuracy of results based on skin tone.

2.4 Human Vital Sign Detection Using Radar Technique

Although we showed that we can retrieve human vital signs using optical techniques, there are several limitations using this technique. The major one is that in order to use cameras, we need to have access to the subject's face. It means in the situation that the subject is behind the wall or not facing the camera, we are not able to extract his/her vital signs. Moreover, if the light on the surface of the subject's skin is not adequate or the subject is in dark, the performance of the camera and the optical technique degrades. In these situations, the accuracy of retrieved vital signs is too low and results are not reliable. Hence, optical systems are adequate only in short ranges and in a well-lit region. In [2.11], we employed cameras and optical technique for vital sign detection in many different situations including different distances between the subject and camera, different orientation of the subject to the camera, and different lighting conditions. The results show

that this technique is not effective for remote triage or through-wall detection, and it significantly degrades or even fails under poor lighting conditions.

Another attractive solution for non-contact human vital sign detection is radar technique. Radar techniques can detect human vital signs in the dark or behind walls.

There are different types of radars, but stepped-frequency continuous-wave (SFCW) radars and frequency-modulated continuous-wave (FMCW) radars have been proved particularly useful to remotely monitor multi-human subjects' vital signs. Compared with a single-tone continuous wave (CW) radar, they can detect the positions of the targets due to their wide Doppler frequency spectrum and therefore, are capable of being used for multi-subject applications. Moreover, when compared with ultra-wideband (UWB) impulse radars, they are less sophisticated and yields higher signal-to-noise-ratio (SNR) in general. In addition, for faster response and to drastically reduce the amount of data, multi-channel SFCW and FMCW radars can employ compressive sensing techniques. For these reasons, a see-through-wall SFCW radar is investigated here. The focus of this work is on extracting and tracking respiratory and heart rates in a near real-time manner using the aforementioned radar systems and by employing advanced signal processing techniques.

2.4.1 SFCW Radar System

The SFCW radar shown in Figure 2.10, also called frequency-domain radar, generates a set of N consistent CW pulses whose frequencies rise from one pulse to the next by a fixed frequency step size Δf. Therefore, the frequency of the n^{th} pulse is,

$$f_{n-1} = f_0 + (n-1)\Delta f \tag{2.1}$$

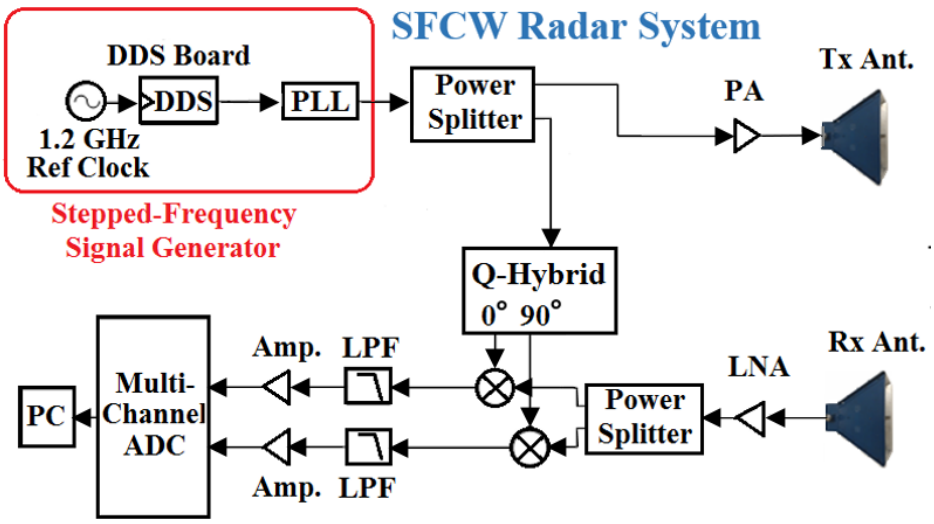

Figure 2.10 SFCW radar system detecting human vital signs.

Table 2.2 SFCW Radar System Parameters

Parameter	Value
RF Frequency Range	2-4 GHz
Number of Channels	2
Frequency Step Size ($\Delta \boldsymbol{f}$)	20 MHz
Number of Frequency Steps in One Frame ($\boldsymbol{N}$)	50
Frame/Pulse Repetition Frequency (PRF)	20 Hz
Sampling Rate	50 kHz
Range Resolution	5 cm

In (2.1), f_0 indicates the initial carrier frequency. Therefore, every frame of the signal includes N frequency steps. Figure 2.10 shows a block diagram of the designed and implemented SFCW radar system for human vital signs detection. The characteristics of the utilized SFCW radar is summarized in Table 2.2.

2.4.2 Signal Processing

Phase based method is a traditional method for extracting vital signs information by using complex data from I and Q down mixing. Specifically, the methods are the complex signal demodulation (CSD) and arctangent demodulation (AD). Since it was proven that CSD method suffers from harmonics interference of respiratory motion of the chest [2.18], this work will not analyze the performance of these hardware systems with CSD method. AD extracts the phases of the I and Q signal over the range profile and phase unwrapping to remove discontinuities when the phase exceeds π. This can be shown as [2.19]:

$$\varphi(t) = arctan\left(\frac{B_I(t)}{B_Q(t)}\right) + F \tag{2.2}$$

where F is added to deal with phase discontinuities. Then, FFT is implemented on the constructed signal to extract the vital signs information of the subjects. Although AD is known to suffer from less interference from respiratory harmonics, AD can still suffer from DC offsets issue, which creates imbalance in the I and Q signal amplitude and phase. This results in a shift and distortion of the received signal constellation.

2.4.3 Experimental Results

The performance of the hardware system and algorithm has been assessed through measurements with different subjects (different genders, ages and health situations).

Figure 2.11 Experimental Setup.

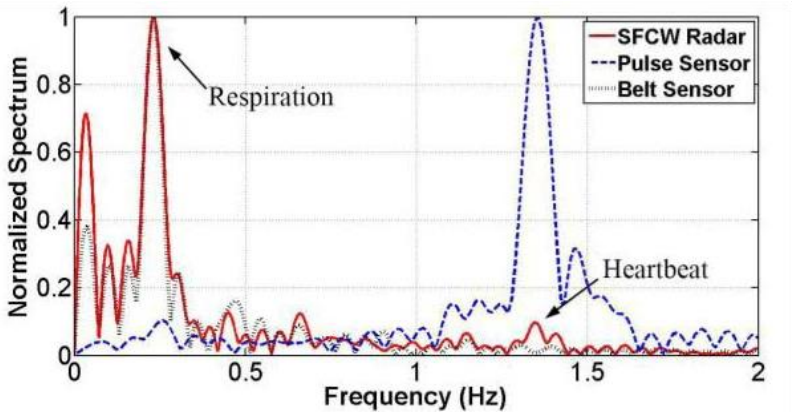

Figure 2.12 Spectrum of vital signs from SFCW radar system and arctangent demodulation method [2.11].

The measurement time was 20 seconds. Experiment with each participant was conducted at different distances. Respiration monitor belt sensor NUL-236 [2.20] and pulse sensor SEN-11574 [2.21] were used as respiratory and heart rate ground truths correspondingly. The radar system mentioned above was used to record data from participants to quantify the performance error on the basis of the ground truth. Figure 2.11 shows the experimental setup in an indoor environment and Figure 2.12 shows the results of RR and HR extracted by AD method applied to the data collected using the SFCW radar system.

As seen from the result, using SFCW radar system and AD method, we can retrieve human vital signs accurately. However, as it is clear from the results, the amplitude of vital signs spectrum for respiration is much higher than the one from heartbeat due to the fact that human chest displacement caused by breathing is much larger than the tiny motions of the body because of heartbeat or pulsation. Considering this fact, in many cases, respiration signal has a strong harmonic near the peak of the heartbeat, which makes it really challenging to differentiate and identify heart rate.

2.5 Comparison Study of Non-Contact Vital Sign Detection using Optical and Radar Techniques

Although radar techniques are suitable for detecting vital signs of human subjects behind the walls or in dark conditions, it is very challenging to detect human SpO_2 using Doppler radars. The reason is that oxygen absorption spectrum has a response in around 60 GHz. However, at this frequency range (mm waves), radar signal cannot penetrate human skin to detect the changes in oxygen in blood. Hence, between different human vital sign parameters, in this work, we use radar technique to detect HR and RR. On the other hand,

we showed that in well-lit situations, the optical technique is also able to retrieve RR and HR accurately. Therefore, it is worth comparing these two different techniques by conducting different sets of experiments and using camera and radar at the same time as detection sensors simultaneously. In this way, considering each technique's pros and cons, we can use the proper technique or combination of both at different specific situations.

In [2.11], we conducted a complete study to be able to compare the performance of camera-based photoplethysmography and radar techniques in different situations and conditions. In fact, we conducted many experiments with different human subjects, at different orientations (angle to the radar boresight), and in many various experimental situations. Here we explain one set of experiments. In this experiment, data of one subject at 1, 1.5, and 2 m away from the experimental system with four orientations specified in Figure 2.13 have been collected simultaneously by the SFCW radar and the iPPG system (camera). The experimental setup is shown in Figure 2.14. Antennas of SFCW radar and cameras of iPPG system were mounted 110 cm above the ground. The transmitting and receiving antennas were 50 cm apart, and the cameras were mounted in the middle between the transmitting and receiving antennas of the SFCW radar. Note that for the iPPG system, when the subject is at the "back" position, the ROI of the captured video is the neck not the face 9in this case the area of the back of the neck is used as the ROI); while when the subject turns right or left, ROI will be the left side of the face and right side of the face of the subject, respectively. The subject (age 31, weight 82 kg, and 1.8 m tall) was sedentary at the same distance from the radar receiver and iPPG system.

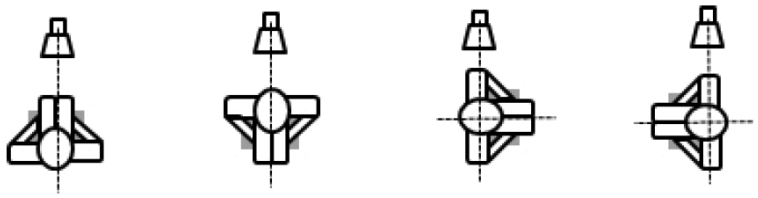

(a) (b) (c) (d)

Figure 2.13 Four orientations of subject (a) front, (b) back, (c) right, (d) left [2.11].

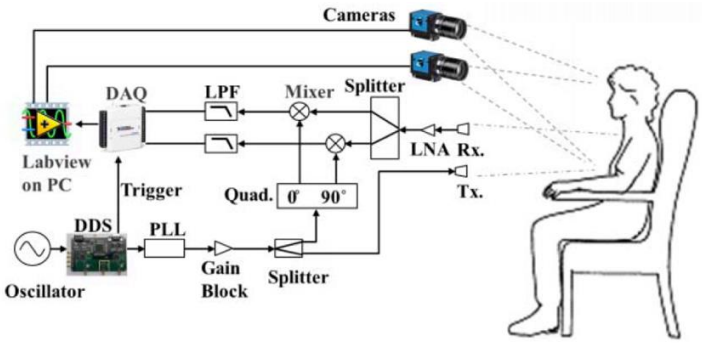

(a)

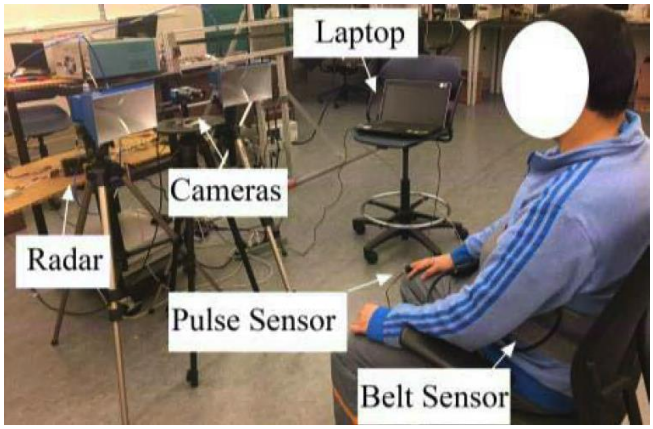

(b)

Figure 2.14 (a) Block diagram of the experimental setup. (b) Experimental setup in laboratory [2.11].

For evaluation, one belt sensor (NUL-236) [2.20] and one BVP sensor (pulse sensor SEN-11574) [2.21] were used as references of respiration and heartbeat, respectively.

The frame rate of SFCW radar is 20 Hz and the sampling rate of camera is 20 frames/s. Both SFCW radar and iPPG system collect data for 30 s in the experiment, while the controlled environment illumination is measured by a lux meter (Extech LT300, FLIR Commercial Systems Inc., Nashua, NH, USA) [2.22].

The accuracy is defined here as "$Ratio$". The ratio of measurement to reference sensor is calculated as

$$Ratio = \frac{V_M}{V_R} \times 100\% \tag{2.3}$$

where V_M indicates measurement result; and V_R indicates reading from the reference sensor.

When a subject is 1 m away from the experimental setup at the position "front" and the illumination level is 500 lx, the demodulated signals spectrums from both radar and optical sensor are compared with the results of the corresponding reference sensor, as shown in Figure 2.12. The respiratory and heart reference rates of a subject were 0.23 and 1.35 Hz, respectively, during the experiment. Both radar and camera demonstrate high accuracies in RR and HR monitoring. For radar, the corresponding ratios to respiratory and heart reference rates are 100.17% and 99.63%, respectively; meanwhile for camera, the ratios to respiratory and heart reference rates are 99.30% and 100%. These differences are less than 1% using either technique in vital signs detection.

The performance of radar and camera in vital signs detection for a subject seen at different orientations and at different distances with 500 lx illumination have been compared.

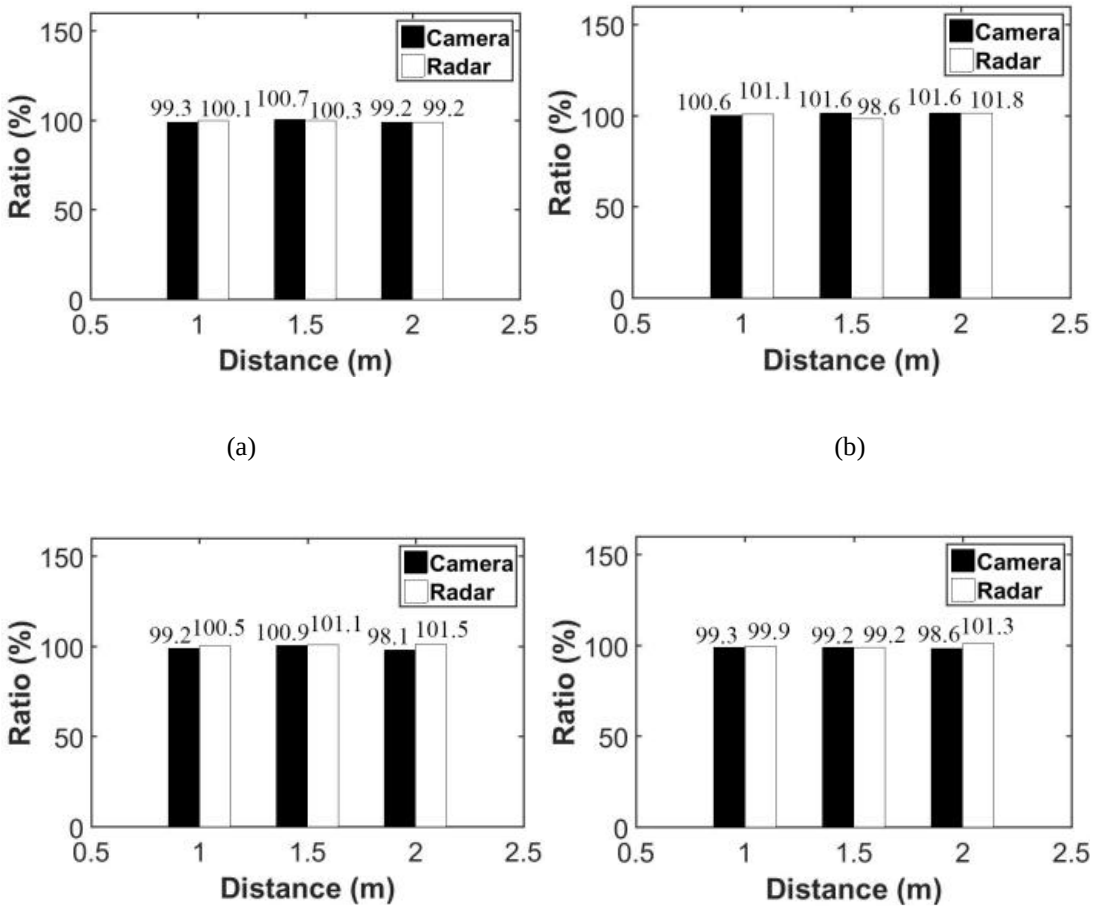

Figure 2.15 When illumination is 500 lx, comparison of ratio to reference using SFCW radar and camera in RR detection when subject is at orientation of (a) front, (b) left, (c) right, and (d) back [2.11].

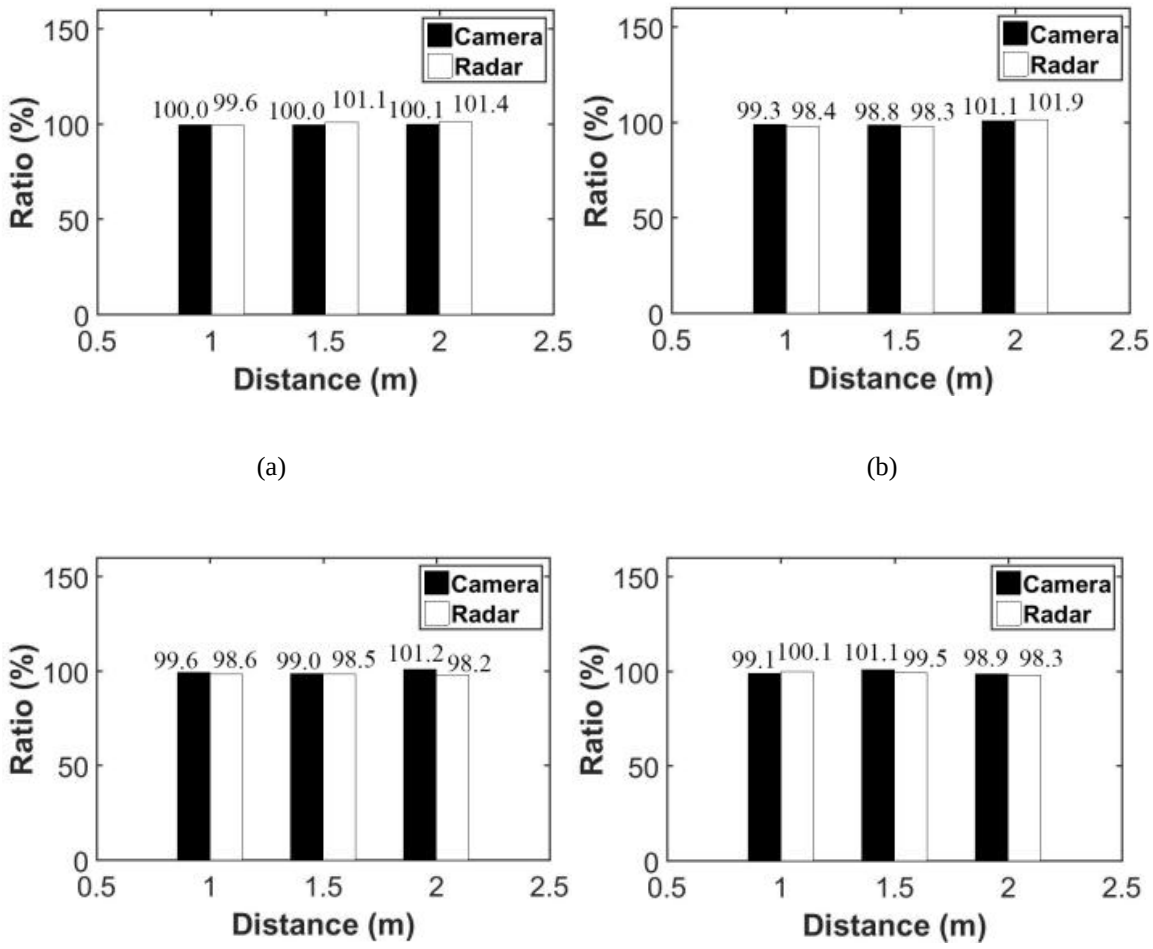

Figure 2.16 When illumination is 500 lx, comparison of ratio to reference using SFCW radar and camera in HR detection when subject is at orientation of (a) front, (b) left, (c) right, and (d) back [2.11].

The results are shown in Figures 2.15 and 2.16. As shown, both radar and camera have ratios for both RR and HR detection within 100% ± 2% for all orientations up to 2 m. Vital signs of a subject at these different orientations can be clearly extracted using radar, especially when subject is in close range. It is also observed that camera is capable of accurate vital signs monitoring as long as videos of exposed human skins are captured. This is consistent with our prediction that both radar and camera sensors possess an SNR in the range of 27 dB when the subject is 2 m away under 500 lx illumination, which ensures the accuracy of vital signs detection for both systems.

To investigate the influence of illumination level on performance of camera in vital signs detection, another experiment is conducted where the subject is 2 m away for the four indicated orientations (front, right, left, and back) but under different illumination conditions. The results are summarized in Figures 2.17 and 2.18. When the illumination level drops from 500 lx to 200 lx, the accuracy of camera in RR monitoring degrades by 10% as indicated by the ratio parameter when the subject is at left or right positions, while the accuracy of HR detection is not greatly affected. When the illumination level is 100 lx, ratios of RRs extracted by camera degrades to 70%, i.e., −30% difference to reference readings, while the ratio of HR is overestimated by 40% when the subject is at the “right” position. Vital signs detected by camera in low illumination level are not reliable. It is worthwhile mentioning that radar is not influenced by illumination conditions as demonstrated in Figures 2.17 and 2.18.

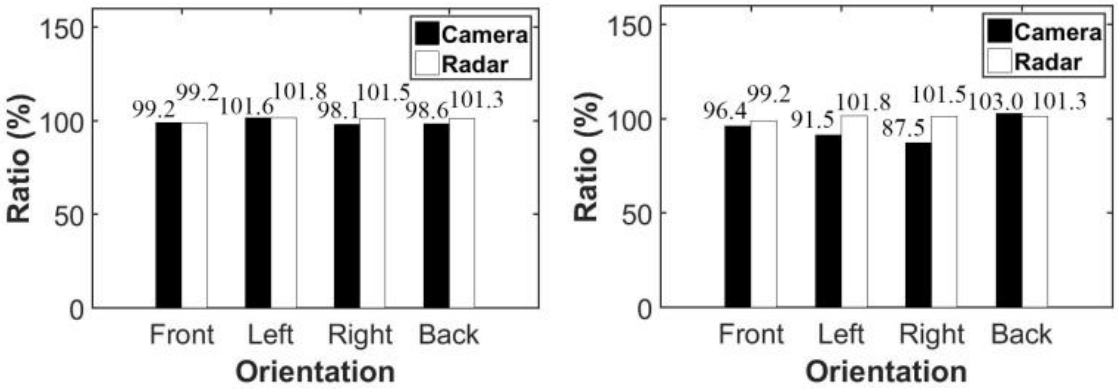

(a)

(b)

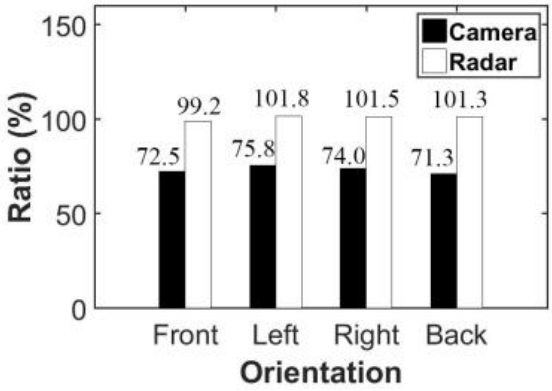

(c)

Figure 2.17 When subject is 2 m away, comparison of ratio to reference using SFCW radar and camera in RR detection when illumination level is (a) 500, (b) 200, and (c) 100 lx [2.11].

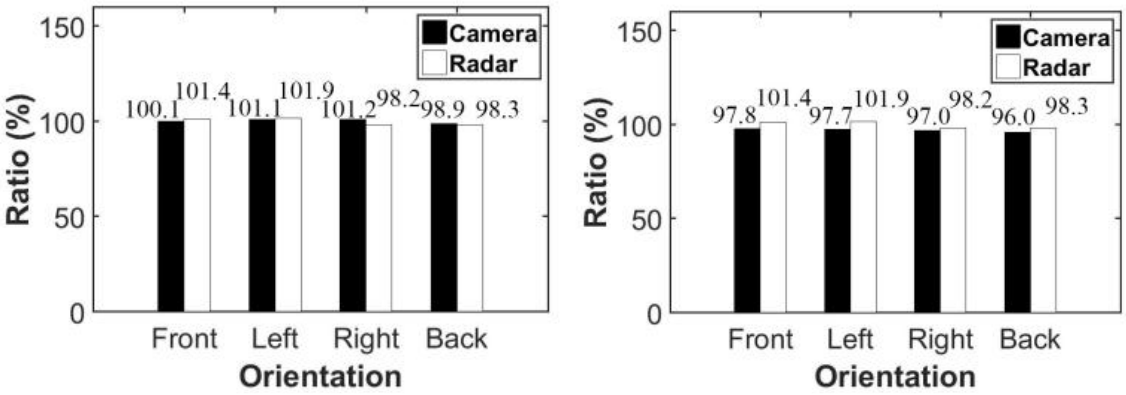

(a)

(b)

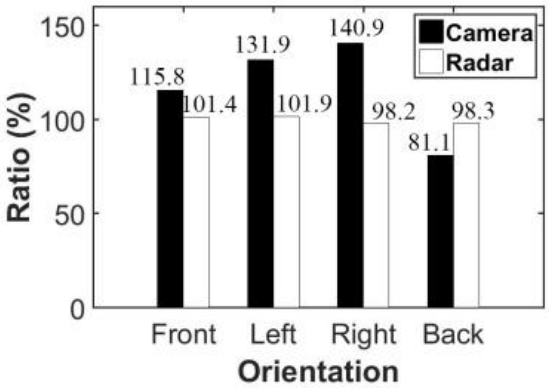

(c)

Figure 2.18 When subject is 2 m away, comparison of ratio to reference using SFCW radar and camera in HR detection when illumination level is (a) 500, (b) 200, and (c) 100 lx [2.11].

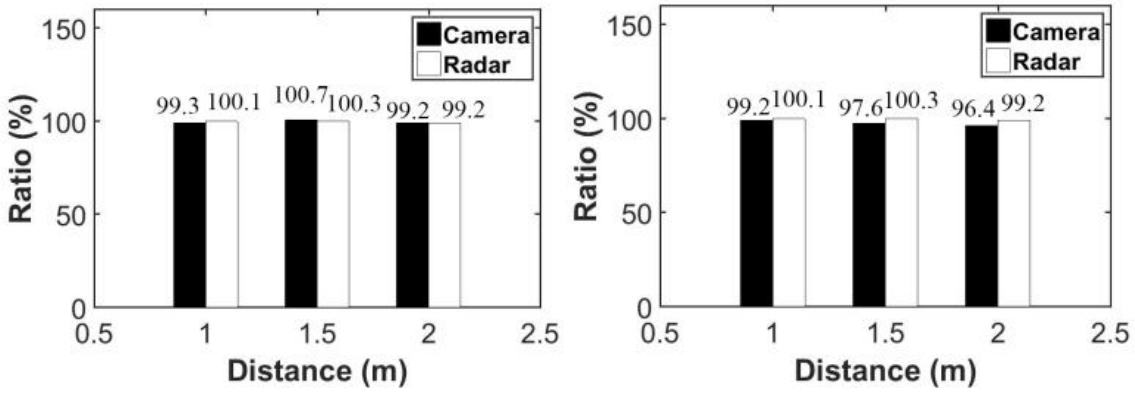

(a) (b)

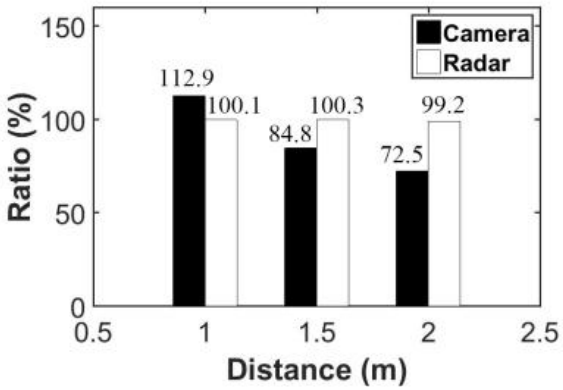

(c)

Figure 2.19 When subject is at orientation of front, comparison of ratio to reference using SFCW radar and camera in RR detection when illumination level is (a) 500, (b) 200, and (d) 100 lx [2.11].

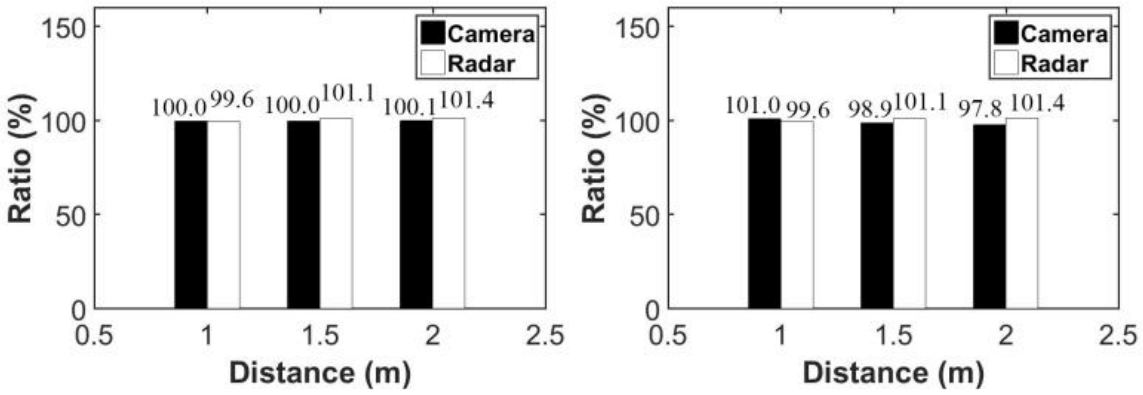

(a) (b)

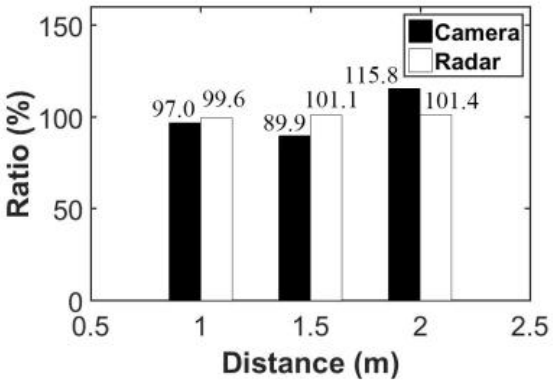

(c)

Figure 2.20 When subject is at orientation of front, comparison of ratio to reference using SFCW radar and camera in HR detection when illumination level is (a) 500, (b) 200, and (d) 100 lx [2.11].

The above experiment was then repeated to study the effect of subject distance from the setup, with the subject in "front" position. As shown in Figures 2.19 and 2.20., when the subject is at front position, RR and HR are readily monitored by camera when lighting level is above 200 lx; when lighting level drops to 100 lx, accuracies for RRs significantly degrade with the increase of subject distance. As shown in Figure 2.20 (c), the ratio of RR measurement to reference degrades from 97% at 1 m, to 89.93% at 1.5 m and 115.81% at 2 m.

2.6 Mono-Static SFCW Radar System

Bi-static radar utilizes two different antennas for transmission and reception. However, use of separate antennas provides adequate isolation between the transmitter and receiver necessary for full duplex operation. For compact radars, however, mono-static architectures are preferred. But isolation between the transmitter and receiver is a concern, since a relatively low leakage from the transmitter to the receiver can cause significant interference and dominates the very weak (low-power) signal reflected back from the target.

For UWB impulse radars, mono-static radars have been successfully developed using high isolation switches. Typically, the receiver is turned off while the transmitter is on, and vice versa the receiver is on while the transmitter is off. The receiver must also be off during any anticipated pulse fall-down time of the impulse radar. Use of fast switches with high isolation (> 30 dB) are adequate for pulsed operation [2.23].

Meanwhile, for CW, FMCW, or SFCW radars, using RF switches results in losing a part of signal since the radar signal is a continuous sinusoidal signal. In case of continuous-

wave radar systems, circulators or couplers are used. There have been several passive leakage cancellation networks for mono-static CW radars [2.24-2.27]. These leakage cancelers however have been designed for narrowband systems. Alternatively, [2.28] and [2.29] presented mono-static transceivers using relatively high isolation couplers. In [2.28], for example, a variable gain block amplifier and a variable phase shifter have been used but needed calibration. In [2.29], a wideband coupler has been designed and led to high insertion loss (> 6 dB). Other methods require use of active elements and complicated calibration methods, but it is generally doable.

However, it is a major challenge to achieve high isolation from the transmitter to the receiver over a wide frequency range. For example, a typical wideband circulator will provide a fraction of a dB insertion loss for signals in clockwise direction, and 18 dB to 20 dB in opposite direction. Normally, 20 dB is not enough to protect the transmitter. Therefore, more than one circulator are used in cascade to provide more than 40 dB isolation from receiver to transmitter as in [2.31]. However, we still see only 20 dB leakage isolation from transmitter to receiver. In other words, the circulator will protect the transmitter from highly reflected signals, but the level of direct leakage from the transmitter to the receiver is still the same as illustrated in Figure 2.22, and increasing the number of circulators will not affect this leakage level. Similarly, low isolation performance over a wide frequency range is expected from wideband couplers. Hence, novel methods are required to eliminate this leakage or significantly reduce it to 30-40 dB down.

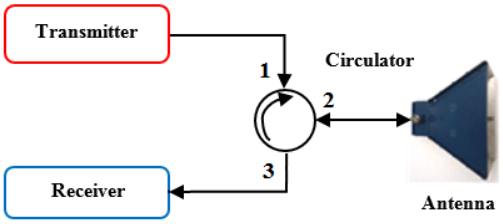

Figure 2.21 Block diagram of mono-static radar using circulator [2.30].

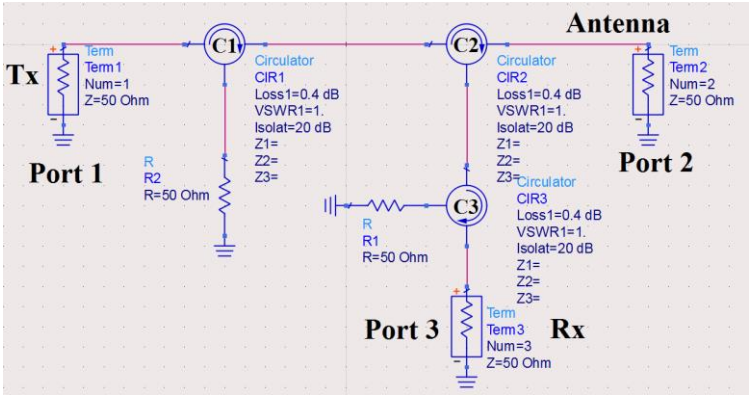

(a)

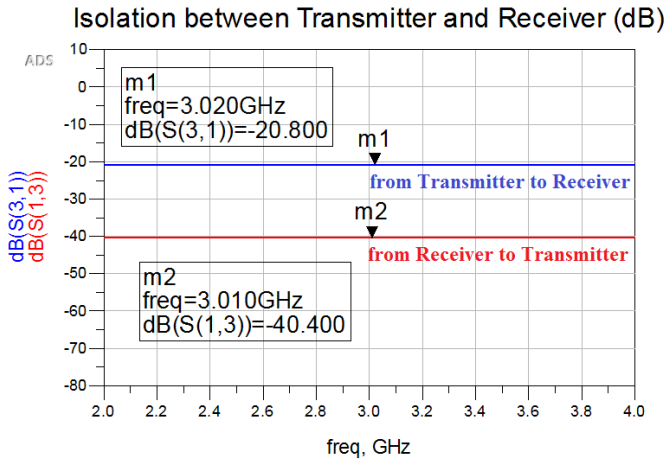

(b)

Figure 2.22 (a) Block diagram of the mono-static radar using 3 circulators; (b) Results of isolation between the transmitter and the receiver.

In this work, we demonstrate a novel passive leakage cancellation network for a wideband mono-static SFCW radar which is easy to implement. The operating bandwidth of the radar system is 2 GHz (2-4 GHz) and provides adequate isolation between the transmitter and receiver that is greater than 33 dB over the radar bandwidth.

2.6.1 Structure of The Leakage Cancellation Network

The proposed assembled leakage cancellation network is comprised of two low-cost similar circulators (RFLC-301-4S) with a relatively poor isolation (18 dB) over a 2 GHz bandwidth, a wideband equal power splitter, a wideband 180° phase shifter, and a wideband in-phase equal power combiner as shown in Figure 2.23 The transmitted signal from transmitter (Tx) is divided equally using a wideband power splitter (W1). Half of the signal goes through a wideband circulator (C1), and then the forward signal goes to the antenna (Ant.), while the leaked signal is fed to one input of a wideband in-phase combiner (W2). The other half goes through the second circulator (C2), and the leaked part goes through a phase block convertor 180° phase shifter (PS) and is fed to the second input of W2. Both leakages travel through identical routes. It is anticipated that we have high cancellation over a wide frequency range, and the desired received signal from the antenna will go through C1 in a clockwise direction followed by W2 to the receiver (Rx).

Practically, it is very challenging to design a wideband phase block convertor over a 2 GHz bandwidth, and maintain the amplitude of the two leakage signals equal due to the fact that one of them goes through the phase convertor and suffers from extra loss. Hence, amplitude adjustment would be needed which could make the system very complicated.

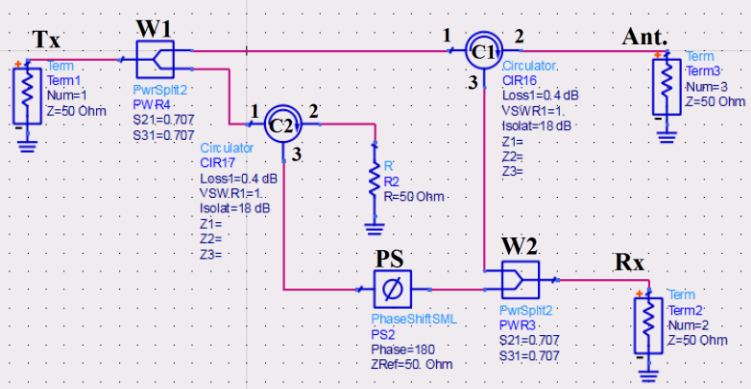

Figure 2.23 Leakage cancellation network working through 2-4 GHz [2.30].

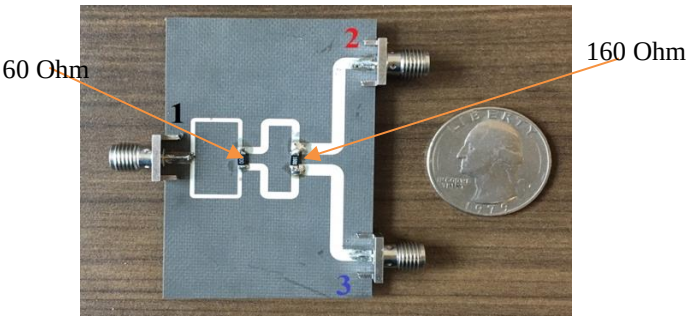

(a)

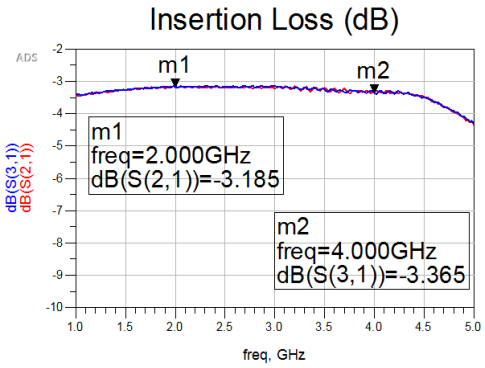

(b)

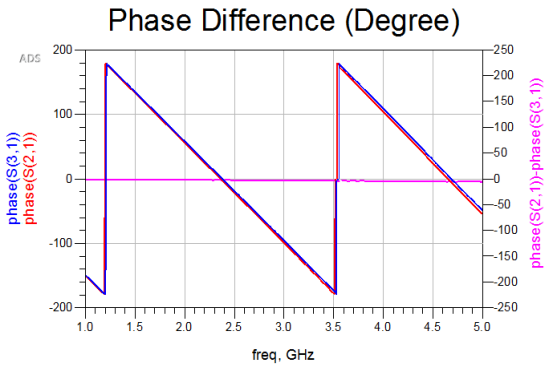

(c)

Figure 2.24 (a) Implementation of the wideband equal power splitter using microstrip lines; Measured results ((b) output ports insertion losses, and (c) phase response) [2.30].

To overcome these two problems, we integrated 180° phase convertor and equal power divider by designing a wideband equal power combiner with 180° phase difference between its two input ports using parallel-strip transmission lines.

However, the penalty of this approach is the extra loss in the received signal due to feeding only one input port of the power combiner, in addition to the 3-dB loss in the transmitted signal that was used to generate an exact duplicate of the leaked signal. Overall, by removing the unwanted leakage signal, we can amplify the received signal which is mainly reflected back from the subject.

2.6.2 Wideband Equal Power Splitter (Divider)

We simulated the Wilkinson power splitter and combiner using CST Studio Suite 2017 and used 31 mil Rogers RT5880 as the substrate. To achieve a wideband in-phase equal power splitter function, we designed a two-stage Wilkinson using microstrip lines to make it wideband and optimized it to achieve equal insertion losses over the bandwidth as shown in Figure 2.24.

2.6.3 Wideband 180° Equal Power Combiner

Figure 2.25 shows the wideband equal power combiner with 180° phase difference between ports 2 and 3. The concept of designing this component is to use parallel-strip transmission lines instead of microstrip lines [2.32]. In Parallel-strip lines, a substrate is sandwiched between two strip conductor lines and therefore, the signals flowing on the upper and lower lines always have equal magnitudes but are 180° out-of-phase. With this approach, we can obtain a frequency-independent 180° differential phase between ports 2 and 3.

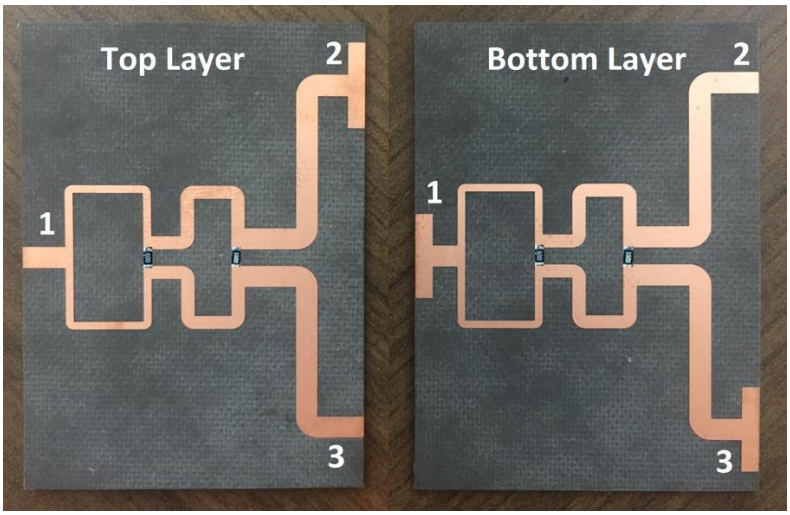

(a)

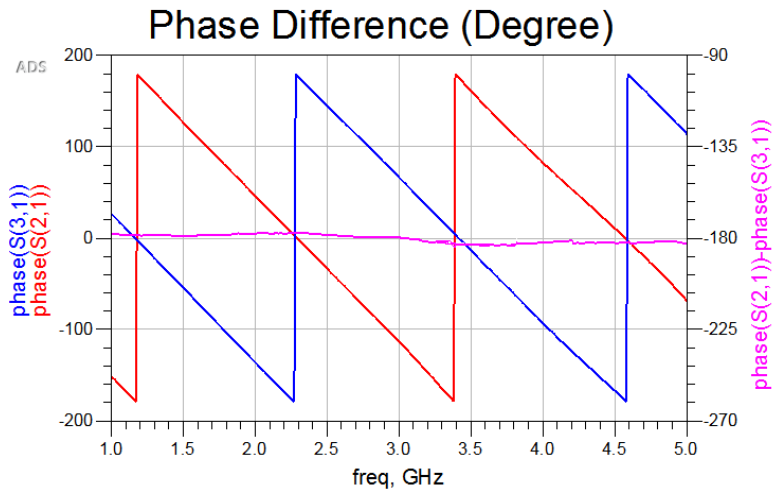

(b)

Figure 2.25 (a) The wideband 180-degree equal power combiner using parallel-strip lines (top layer (left); (b) bottom layer (right)), and phase response measurements [2.30].

This is achieved by step transitioning the parallel-strip lines to microstrip lines while connecting the inner conductor of SMA connectors to the lower line in port 2 and to the upper line in port 3 as shown in Figure 2.25. Measured results show 180° ± 2° phase difference between output ports. To make the combiner wideband we used a two-stage Wilkinson with a center frequency of 3 GHz. The insertion losses and resistors are the same as the in-phase power splitter.

2.6.4 Measurement Results

All components in the designed leakage cancellation network were assembled, and the measured isolation from the transmitter to the receiver is shown in Figure 2.26, while the insertion loss from the antenna to the receiver is less than 4.05 dB over the entire bandwidth. The results demonstrate that this cancellation network reduces the leakage signal by more than 33 dB through the whole 2 GHz operating bandwidth, while it passes the received backscattered signal from the target to the receiver. Thus, this network provides a full duplex operation over a wide frequency range.

Therefore, a wideband low-cost passive leakage cancellation network comprised of a wideband equal power divider, two circulators, and a wideband 180° parallel-strip line power combiner has been proposed to cancel the unwanted signal due to the leakage from the transmitter to the receiver. The implemented canceler provides more than 33 dB isolation between the transmitter and receiver over a 2 GHz which is adequate for mono-static radar application. The performance is comparable to active leakage canceler schemes and has even wider bandwidth. This work has been compared to similar works in Table 2.3. As be seen, this canceler has a wider bandwidth and lower insertion loss.

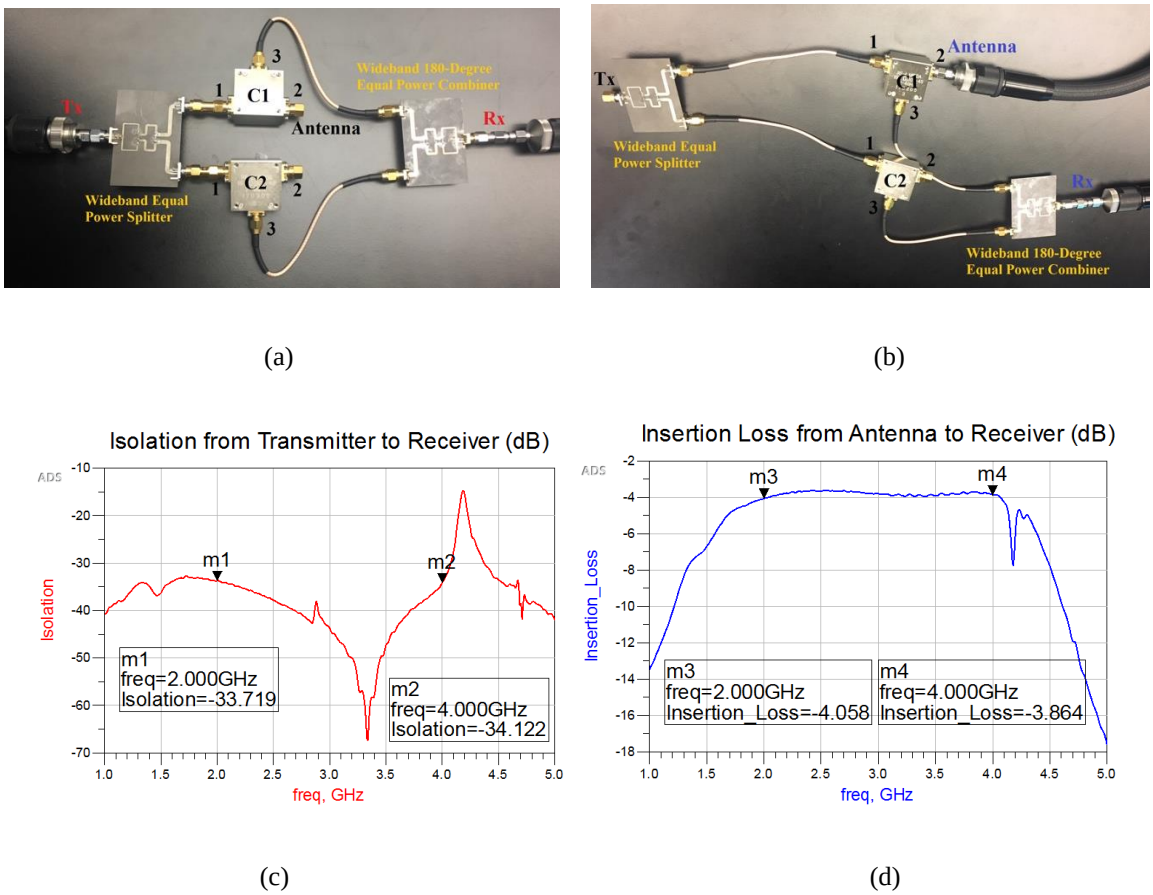

(a) (b)

(c) (d)

Figure 2.26 The leakage cancellation network; measuring the isolation from the transmitter to the receiver (left) (a) and (c) and measuring the insertion loss from the antenna to the receiver (right) (b) and (d) [2.30].

Table 2.3 Summary of Similar Leakage Cancellation Networks

Ref.	BW (%)	Freq. (GHz)	Insertion loss (dB)	Isolation (dB)	Type	Network Structure
[2.24]	8.33	24	> 6	30	passive	Five Q-hybrids
[2.25]	6.25	24	N/A	35	passive	A Wilkinson and a coupler
[2.26]	2.5	24	N/A	45	passive	Ring hybrids, Q-hybrids and Wilkinson power dividers
[2.27]	1.26	25.46	N/A	40.5	passive	Two large couplers and a Wilkinson power divider
[2.28]	18.75	6.4	N/A	36	active	Tunable canceller using variable phase shifter and gain block amp.
[2.29]	10	60	> 5	30	active	A tunable coupler
This work	67	3	4	33	passive	Two circulators, a Wilkinson, and a 180° power combiner

2.6.5 Reflection from Antenna Port

The results for leakage cancellation network are very good and the network provides a relatively high isolation between the radar transmitter and receiver, and acceptable insertion loss from the antenna to the receiver for a wide bandwidth. Therefore, this leakage canceller can be used in SFCW radar system in order to reconfigure it as a mono-static radar system. Hence, in this mono-static configuration, we only use one antenna to send the radar signal to the target and receives the backscattered signal from the target and guide it to the receiver side, simultaneously.

However, there is another challenge connecting the antenna to the circulator, due to the return loss or reflection from the antenna port. In reality, in Figure 2.23, port 2 of C1 9circulator 1) is connected to the antenna. If the antenna is very good, it has the return loss of bellow -15 dB for the entire bandwidth. Therefore, a considerable part of transmitting signal reflects back from the antenna and goes to the receiver path, which is very strong compared to the weak received backscattered signal from the target and is even stronger than leakage signal due to the poor isolation of circulator. Therefore, cancelling this reflected signal from antenna is as important as the leakage signal.

To solve this problem, we need to create the exact reflected signal from antenna in the other path by putting the same antenna at port 2 of C2 which is facing to another direction. However, using a programmable dummy load at port 2 of C2 can do the same duty. Figure 2.27 shows the structure of the mono-static radar system including Tx/Rx antenna and dummy antenna for reflection cancellation purposes.

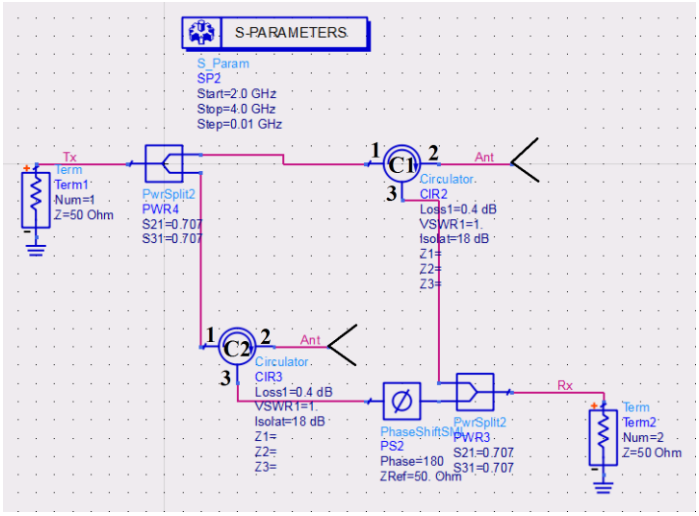

Figure 2.27 The structure of the mono-static radar system including Tx/Rx antenna and dummy antenna for reflection cancellation purposes.

2.6.6 Validation and Vital Sign Detection Results

In order to validate the performance of the leakage cancellation network and therefore mono-static SFCW radar system with two channels and operating at 2-4 GHz, we utilized it to collect data from a human subject sitting in front of the radar. Then, we formed range profile and then processed the collected data using arctangent demodulation method to retrieve respiratory and heart rate. Figure 2.28 shows mono-static SFCW radar system with only one antenna that transmits the radar signal and receives the radar returned signal from the subject simultaneously in the indoor environment of the lab and Figure 2.29 shows the results.

From Figure 2.29, we can see that the range profile is pretty clean and shows the subject's range clearly. Moreover, the results of vital signs match the contact sensors well. Comparing the results of Figure 2.29 from the mono-static SFCW radar with the ones in Figure 2.12 while we used bi-static configuration of the same SFCW radar system shows that eliminating the receiving antenna does not have any adverse effect on the performance of the SFCW radar system and still we have less than 1% error extracting vital signs. In fact, the beauty of this method is that the leakage cancellation network is completely a passive and low-cost network, and therefore, does not need any calibration or complex method to use.

2.7 Near Real-Time SFCW Radar System

Near real-time operation has been developed and being improved over time for SFCW radar system.

Figure 2.28 Mono-static SFCW radar system for human vital sign detection.

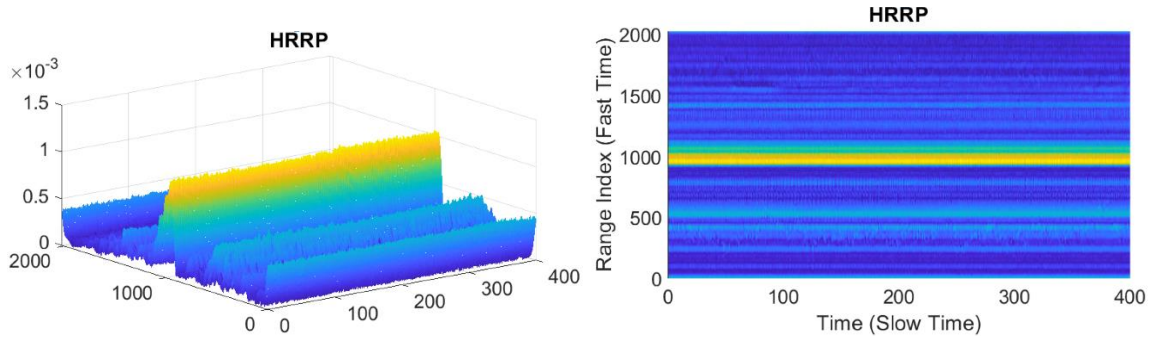

(a)

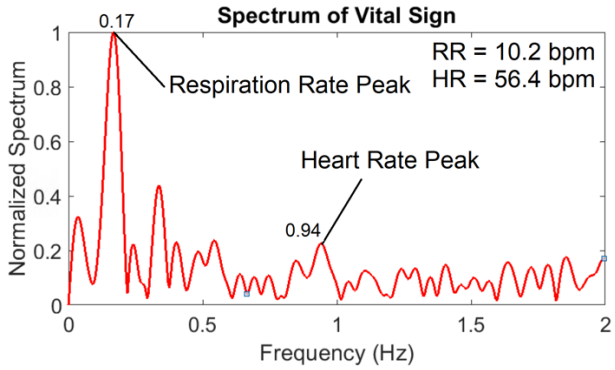

(b)

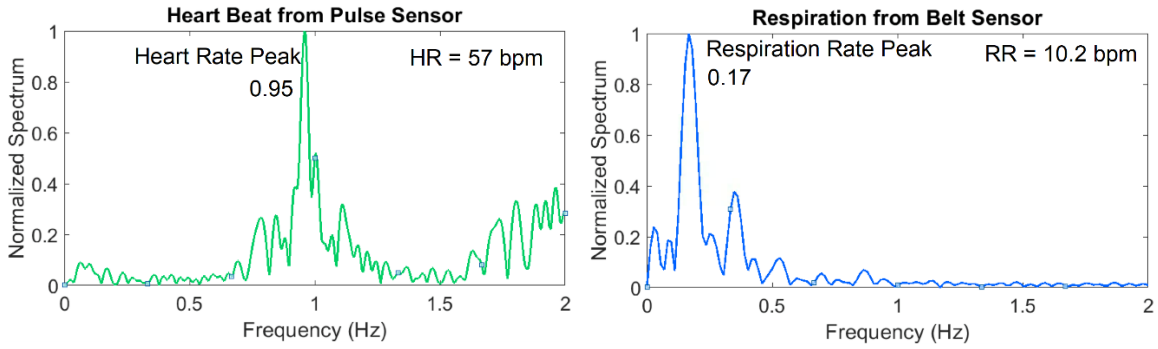

(c) (d)

Figure 2.29 Results from the data collected using mono-static SFCW radar; (a) 3-D and 2-D HRRP; (b) Spectrum of vital signs measured using mono-static SFCW radar; and (c) Pulse sensor; and (d) Belt sensor.

My colleague, Toan Vo Dai, and I developed the Graphics User Interface (GUI), shown in Figure 2.30, that displays vital signs and distance-from-radar of subjects. Figure 2.30 shows a screenshot of the GUI.

Arctangent demodulation (AD) method is used at this time for real-time operation. In AD method, we use I and Q channels information to extract the phase information of the radar return signal. However, in real-time demo we put all the steps in AD method, taken towards extracting vital signs, in a sliding window with a specific window size that is moving and extracts vital signs. Then, we are able to estimate the values of vital sign parameters using the overlapped parts of the window. The following steps show the flow of AD:

1) Collect data using SFCW radar;

2) De-noise the data and filter out the undesired and out-of-band data;

3) Remove the static background reflection by subtracting the mean of the radar return signal;

4) Construct high-range resolution profile (HRRP) by applying iFFT along the range or fast-time axis;

5) Apply FFT along the range axis of the HRRP to focus on the phase information;

6) Calculate the arctangent of the complex signal obtained from step 5;

7) Unwrap the phase to obtain the displacement signal;

8) Apply FFT on the displacement signal to extract the spectrum;

9) filter the results to extract RR and HR.

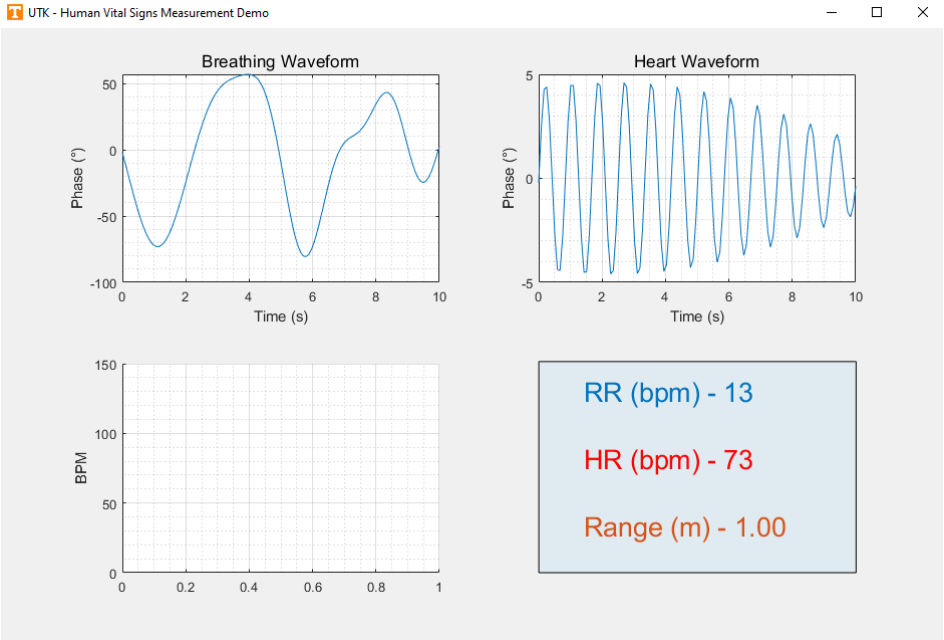

Figure 2.30 Graphic user interface (GUI) for near real-time vital sign demo of SFCW radar system.

However, in real-time demo, we put all the steps inside a sliding window moving along the slow-time (time) axis. To better estimate the heart rate, instead of conventional FFT we employ STFT with sliding Hamming window with a length equals 2/3 the length of original signal and an overlap of 95%. This way we have multiple heart rate estimation corresponding to each sliding window. In this way the results are refreshed and updated every 5 seconds. The final estimate will be done by first getting rid of outliers estimated values using their mean and standard deviation similarly. The remaining estimated values will be averaged to get the final heart rate estimation.

2.8 Conclusion

In recent years, researchers have presented a number of new and interesting methods for non-contact physiological parameters detection using iPPG and radar techniques.

In this chapter, SFCW radar and iPPG technologies were briefly reviewed, discussed, and compared. The two methods were utilized for the extraction of HR and RR at similar conditions to simplify the comparison. Results from the experiments of the SFCW radar system, indicated that the detection of HR was within an error rate of 2% irrespective of the subject's four described orientations up to 2 m. The experimental results also show that SFCW radar has demonstrated slightly better accuracy in the extraction of HR in front and back positions.

Conversely, iPPG technique is uniquely capable of remotely detecting oxygen saturation levels and blood pressure and has similar performance to radar for HR and RR under ambient light conditions. However, it is not effective for remote triage or through-wall detection, and it significantly degrades or even fails under poor lighting conditions.

In this chapter, we showed that different configurations of the 2.4 GHz SFCW radar system, including bi-static and mono-static, can be used in extracting human vital signs, accurately. Promising results from SFCW radar system, encouraged us to extend its application and use it to retrieve more complex parameters of human health, that is human gait. In the next chapters, we will explain the non-contact methods of human gait analysis using radar (SFCW radar) techniques.

CHAPTER THREE
HUMAN GAIT ANALYSIS USING RADAR TECHNIQUES

3.1 Human Gait Investigations

Human gait investigations continue to attract many scientists and practitioners in fields such as sport medicine, geriatric medicine, bio-mechanic and bio-medical engineering. These investigations include segmentation of human body parts for athletic performance evaluation [3.1], health issue diagnosis [1.29], [1.30], automatic monitoring of human activities in security-sensitive zones [3.2], elderly health care monitoring [1.32], man–machine user interface design [3.3], and smart video conferencing [3.4]. The goal here is to further understand any motion abnormalities; hence, we need to thoroughly track and understand the normal motion of human limb joints first. Then, it will be very helpful to accurately monitor human subjects or patients over time to provide early flags of possible complications in order to aid in a proper diagnosis and development of future comprehensive treatment plans.

Commercially, many types of sophisticated equipment have been in the market to monitor, track, record, and analyze patients' motions like spinal cord analysis machines, adaptive motion trainers, and stretch trainers. However, these types of equipment are not widely used because they are either invasive (required to be imbedded in the patient's body) or need contact (require touching the patient), and often are expensive. So, the search is still prevalent for continuous indoor monitoring of patients' motion with aims to extend to outdoor environments. It is expected that these techniques will not obstruct patients' regular activities and will not intrude their privacy.

3.2 Radar Techniques for Human Gait Analysis

Alternatively, radar techniques are more suitable for these non-invasive, non-contact motion activity observations and can provide remote monitoring. Using radars for motion analysis provides non-contact, long-range coverage, which can be fulfilled using simple, low-cost single-tone radars or wideband radar systems to detect and track single or multiple subjects. Various radar types have been used for non-contact remote gait analysis; however, it is typically hard to distinctly track different body limbs. Low cost single-tone continuous wave (CW) radar is a very attractive option and has been used with great success for remote gait analysis [3.5], although it cannot extract any range information and cannot track more than one subject, which is a serious limitation for multiple-subject monitoring.

Complex human motion is generally an amalgamation of movements from different body limb joints. Therefore, the backscattered radar signal from a walking subject, can be analyzed by uniquely assigning the radar returns to the individual micro-Doppler (μ-D) signals from various limb joints.

It is generally very challenging to practically retrieve and separate μ-D features of body part trajectories from a walking subject due to their wide Doppler frequency spectrum, i.e. their various speeds. Additionally, range information is a must to analyze more than one subject and be able to separate various subjects' motions based on their range bins. Therefore, a high-performance wideband radar is required to provide high range-resolution information in conjunction with a robust signal processing technique to retrieve and separate the μ-D frequencies of all moving parts in a multiple-subject scenario.

For a wideband frequency operation, either a SFCW radar, with a linearly stepped frequency to cover a wide bandwidth can be used, or a frequency modulated continuous wave (FMCW) radar which emulates a wideband signal by continuously sweeping frequencies over a wide range. Many chips for FMCW radar system currently exist and they have been successfully addressing the challenging concern that calibration (make up for amplitude and phase distortion for various frequencies) is needed if any non-linearity exists due to the fact that the frequency is being swept in FMCW systems with very fine steps or in a continuous way. Both radar systems, however, can provide localization and multiple-subject detection.

Ultra-wideband (UWB) impulse radar is another alternative technique in which a signal with a large instantaneous bandwidth is employed and can simultaneously extract a subject's velocity and range information. A disadvantage of a UWB-IR radar system is that it requires a high-performance, fast ADC with high sampling rate or other sophisticated devices (e.g. equivalent time sampling systems) in the receiver to capture and digitize the data signal, which results in an expensive system and huge data storage. Recently, UWB impulse radar chips start to be commercialized like the one from [3.6] and would require further evaluation for this application.

On the other hand, SFCW radar is preferred here, as it has an instantaneous narrow bandwidth combined with a wide effective bandwidth (successively over numerous pulses) implying that the hardware necessitates less strict requirements. In other words, upon using SFCW radar system, use of high-speed ADCs and sophisticated processors can be avoided. Additionally, the effective receiver bandwidth is narrower, hence the collected receiver

thermal noise “KTB”, is lower which leads to a much better instantaneous signal to noise ratio (SNR) and this could lead to an increase in radar’s sensitivity. Moreover, SFCW radar provides various advantageous such as high range resolution, wide dynamic range, low noise figure, high mean power, single or multiple frequency processing, and even the possibility of using compressive sensing methods [1.28]. It can also be programmed to work as a CW radar if needed.

SFCW radar system’s calibration is relatively straightforward given that in a SFCW system we have only a discrete, finite, number of frequencies with large step sizes to calibrate. Therefore, we have chosen a SFCW radar (for this investigation) as a convenient and attractive solution for gait analysis. SFCW radar is capable of detecting and tracking human motion accurately and extracting μ-D features of various body joints for multiple subjects. It only requires a low-cost digitizer or data acquisition system with less sophisticated calibration needs compared to UWB-IR and FMCW radar systems, but the recent availability of impulse and FMCW radar chips could open the door to be reconsidered for further investigations.

Previously, we developed a two-channel SFCW radar system with a frame rate (or pulse repetition frequency (PRF)) of 20 Hz [1.28]. It was used for human vital sign detection [2.11], human fall detection [3.7], motion classification, and SAR imaging. But generally, for proper detection of a high-speed moving body limbs, the radar PRF has to be no less than twice the maximum measurable Doppler frequency caused by the motion with respect to the operating frequency. Subsequently, we need to use a SFCW radar with a high PRF to be able to extract the velocity of fast-moving body parts such as toes [3.8]. However,

having such a system is challenging since we need to increase the frequency stepping rate and also to develop a robust algorithm to decimate the data collected using a fast frequency-stepping SFCW radar. Both hardware and data handling problems led us towards establishing a high-performance SFCW radar system for multiple-subject gait analysis purposes; that will be described in more detail in the following sections.

3.3 Signal Processing Algorithms for Human Gait Analysis

Along with using the appropriate radar system, there has been a large number of investigations for implementing advanced signal processing methods to effectively utilize the data collected by such radars. Most of these methods employ a time-frequency analysis of the backscattered radar signals. For instance, the short-time Fourier transform (STFT) method is widely employed for motion investigation or classification [3.9]. However, STFT is not capable of extracting individual features of different limbs. Meanwhile, there are other techniques like Hilbert-Huang transform (HHT) [3.8], [3.10], inverse Radon transform [3.11], multiple signal classification (MUSIC) [3.12], wavelet transform [3.13], artificial neural network [3.14], and short-time state space method (ST-SSM) [3.15] that can be used. In Table 3.1, we have summarized the current signal processing techniques employed for gait analysis which are implemented on wideband radar return signals. Table 3.1 summarizes the current signal processing techniques employed by wideband radars for gait analysis. Among these signal processing techniques, those techniques based on state-space methods have shown great success in analyzing radar data for gait purposes. For example, ST-SSM was successfully used by our group to extract μ-D features of human body for gait investigation utilizing a UWB impulse radar [3.15].

Table 3.1 Major Investigations on Human Gait Analysis using Wideband Radar Systems

Ref. and Year	Radar Type and Operating Frequency	Signal Processing Method	Features	Results
[3.16] 2005	FMCW (f_c 10.526 GHz)	---	FMCW signal with center frequency of 10.526 GHz.	Deriving gait characteristics associated with carrying a bomb attached to the body; Only tracking of thorax.
[3.13] 2007	SFCW (8.9-9.4 GHz)	Wavelet	8.9-9.4 GHz SFCW signal; 10-MHz step size; 20-Hz PRF (very low PRF).	Only spectrogram results; No specific body part or individual organ tracking.
[3.17] 2008	SFCW (8.9-9.4 GHz)	S-Method + Viterbi Algorithm	8.9-9.4 GHz SFCW signal; 10-MHz step size; 20-Hz PRF (very low PRF).	Analysis in high noise environment situation; Low-computational cost method; Results for torso and legs of a walking subject, but no full cycle of hand swing.
[3.18] 2009	FMCW (2-4 GHz)	IFFT	2-4 GHz FMCW signal; 0.4-ms PRT (very high PRF) generated using a fast frequency swept YIG source.	Fluctuation of Pulse intensity along the tracking; Only tracking; No feature extraction.
[3.19] 2011	SFCW (1-2 GHz)	IFFT	1-2 GHz SFCW signal; 2-MHz frequency step size; Four parallel PLLs; 11.1-Hz PRF (very low PRF).	Only motion sensing; No motion tracking.

Table 3.1 Continued

Ref. and Year	Radar Type and Operating Frequency	Signal Processing Method	Features	Results
[3.20] 2012	UWB (8-12 GHz)	Nonlinear Least Squares + Expectation Maximization	UWB Impulse signal; High-resolution radar.	Very high computational cost; High range resolution needed; Tracking torso, hands and legs of multiple subjects while walking.
[1.17] 2012	CW + UWB (f_c 3 GHz)	STFT	3-GHz CW signal with 700-ps pulse with 3-GHz carrier frequency; 75-Hz PRF (low PRF); FPGA-based hardware is needed for equivalent time sampling.	Through-wall sensing; Expensive computational cost; Real-time tracking of target; Multi-subject detection; Only combined spectrogram; No feature extraction.
[1.22] 2014	CW + FMCW (f_c 5.8 GHz)	STFT	FMCW signal with 5.8-GHz carrier frequency and 160-MHz bandwidth; Very expensive signal generator.	Positioning and motion detection; Doppler shifts caused by motions; No individual feature extraction from various limbs and organs.
[3.21] 2017	CW + UWB (f_c 24.125 GHz)	---	DWM1000 chip from Decawave as UWB-IR radar; K-band Doppler radar InnoSenT IPS-154 operating at 24.125 GHz.	Walking trajectory detection; No feature extraction.

Table 3.1 Continued

Ref. and Year	Radar Type and Operating Frequency	Signal Processing Method	Features	Results
[3.22] 2017	FMCW (f_c 5.8 GHz)	STFT	5.8-GHz carrier with 320-MHz chirp bandwidth; 3.5-ms PRT (high PRF); Hard to calibrate.	Detection of hand motion in multi-subject scenarios; No limb joints tracking.
[3.23] 2017	UWB (0.5-3.5 GHz)	Machine Learning	250-Hz PRF (high PRF); Very complex and expensive hardware.	Real time classification using training data set from combined motion-capture and Boulic walking model; Results shown from simulated data only.
[3.8] 2017	SFCW (0.5-3.5 GHz)	MHHT	250-Hz PRF (high PRF); Very expensive hardware;	Noisy Spectrogram; Extraction of only positive velocities.
[3.15] 2018	UWB (1.5-4.5 GHz)	ST-SSM	1.5-4.5 GHz impulse signal; 75-Hz PRF (Low PRF); FPGA-based hardware is needed for equivalent time sampling.	Analysis in low-SNR environment; Extraction of only torso and legs; Feature Extraction; No hand motion extraction.
[3.5] 2019	CW + SFCW* (70 MHz-6 GHz)	1-D Block Processing	Only CW mode (2.45 GHz) of AD9364 SDR SDR (AD-FMCOMMS4-EBZ).	Feature extraction of different body components; No multi-subject detection.

*Not using SFCW mode due to the low PRF and the random changing of phase difference between transmitter and receiver at every step of SFCW mode.

However, ST-SSM was only limited to extract the velocity of torso, left foot, and right foot, as the utilized PRF of this UWB-IR system was relatively low (only 75 Hz). Therefore, we were not able to track other body joints with weaker return signals using ST-SSM/UWB impulse radar even with higher model orders. Hence, there have been a need for faster frame rates or a higher PRF to track other relatively faster body parts motions resulting in sophisticated hardware and huge data sizes.

3.4 Challenges and Problem Statement

As mentioned, among various types of signal processing methods employed by different researchers for gait analysis and extracting of gait features (μ-D signals), state-space method (SSM) based techniques have demonstrated promising results and the capability of separating the μ-D features associated with different limb joints separately. However, STFT is still used widely to explore initial motion extraction by representing time-frequency spectrogram of the motion. Here, the results from the major works on human gait analysis using both STFT and SSM done in our research group and using other methods and techniques implemented by other groups are presented.

3.4.1 Gait Analysis using Ultra-Wide Band (UWB) Impulse Radar

The UWB radar described in chapter one was used to collect data from human subjects in [3.15]. Data was saved into a dataset denoted by $s(k, n)$, where $k = 1, 2, \dots, K$ represents fast time or range index, and $n = 1, 2, \dots, N$ denotes the slow time or cross-range index. We can apply FFT first to each reflected pulse along fast time and acquire its corresponding spectrum.

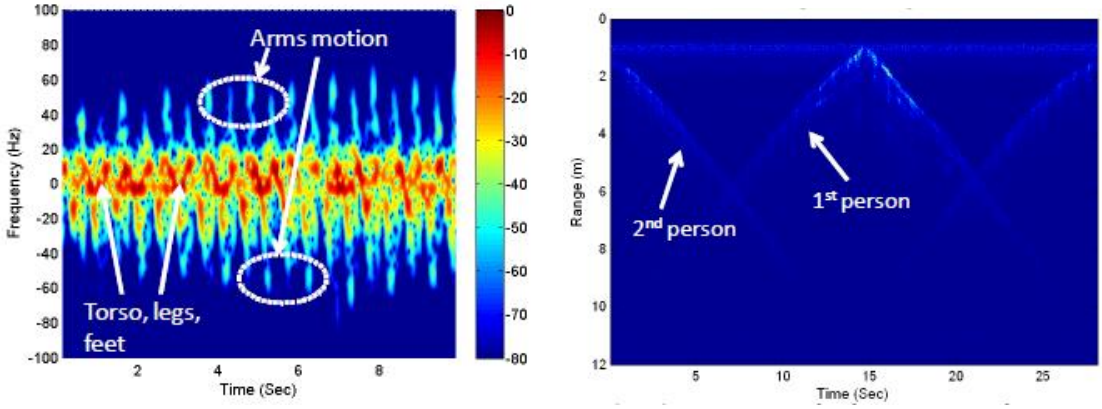

(a) (b)

Figure 3.1 (a) Time frequency spectrogram of a walking person; (b) Range profile image of multiple person walking scenario [1.17].

In this manner, dataset $s(k,n)$ is transformed into $S(m,n)$ in the frequency domain, where $m = 1, 2, \dots, M$ represents fast-time frequency index. A conventional joint time-frequency transform, i.e. STFT, can be applied to the slow-time signal $S(m_0, n) = S_{m_0}(n)$, where m_0 indicates a selected frequency bin in the fast-time spectrum of the reflected pulse. The power spectrum illustrating signal variation in both time n and slow-time frequency f domains for a given fast frequency m_0 is calculated as

$$S_{m_0}{}'(n,f) = \left|\sum_{p=-\infty}^{\infty} S_{m_0}(p)g(n-p)e^{-jpf}\right|^2 \tag{3.1}$$

where $S_{m_0}(p)g(n)$ is a sliding-window function.

As a result, we could extract time-frequency spectrogram of a walking person and range profile images of multiple subjects in a walking scenario [1.17]. Figure 3.1 shows the results. As it is clear from Figure 3.1, no limb tracking has been performed.

On the other hand, state-space method is a parameter estimation algorithm with robustness against noise and efficiency in computation [3.24]. In SSM, forming the Hankel matrix from the data string (one-dimensional (1-D) data) is a key step of this algorithm. This data string or vector is formed from a range profile data by focusing on one range bin, in the fast-time axis in UWB radar data, or summing up the data of a range profile along the fast time or range axis. However, since only one range bin cannot represent the whole motion of the walking subject, we form the data vector by summing up all the data of the range profile along the range axis. The Hankel matrix derived from 1-D data is expressed as

$$H = \begin{bmatrix} y(1) & y(2) & \dots & y(L) \\ y(2) & y(3) & \dots & y(L+1) \\ \vdots & \vdots & \vdots & \vdots \\ y(N-L+1) & y(N-L+2) & \dots & y(N) \end{bmatrix} \tag{3.2}$$

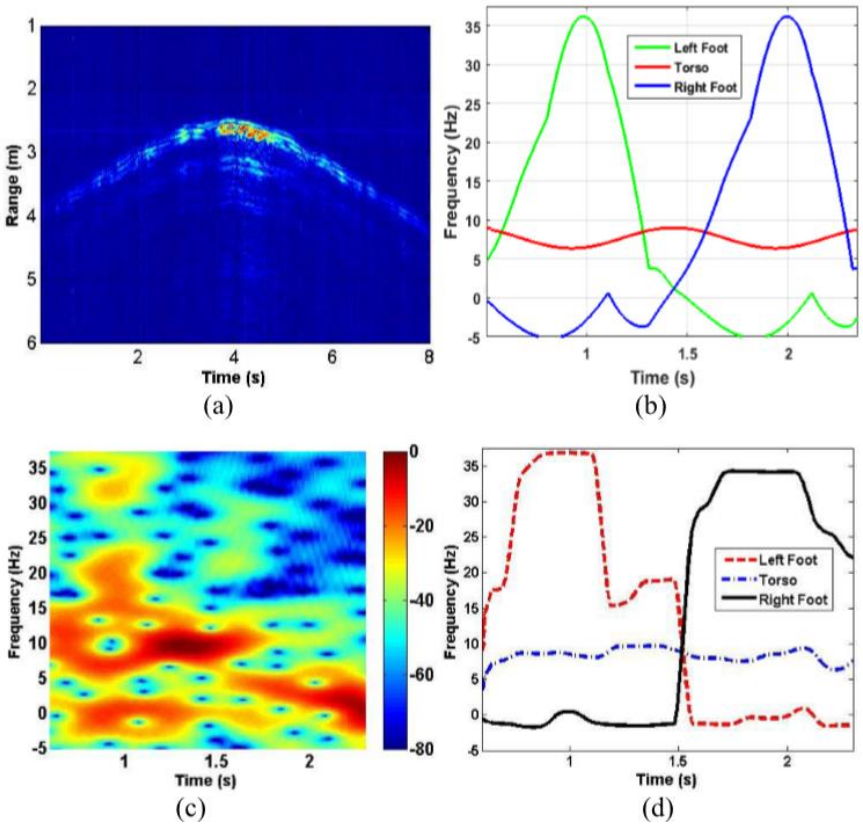

Figure 3.2 Subject 1 (with height of 1.71 m) walking in front of the radar with the speed of 0.40 ms^{-1}; (a) HRRP; (b) Boulic model. (c) Spectrogram using STFT when a sliding window with the length of 50 pulses is applied; (d) Spectrogram using ST-SSM when a sliding window with the length of 50 pulses is applied [3.15].

In Hankel matrix, L is $[N/2]$ and brackets denote the smallest integer equal to or greater than $N/2$.

In 2017, UWB impulse radar system and state-space method for human gait analysis [3.15] was used. In this way, short-time SSM (ST-SSM), was considered for μ-D feature extraction in low SNR situations. Similar to the ST-FT method, we focus on one data bin m_0 and consider the data set $S(m_0, n)$ after FFT of each pulse, where $m = 1,2,\dots,M$ represents fast-time frequency index, $n = 1,2,\dots,N$ denotes slow time index. However, we use a shorter sliding window function to obtain the data sequence, noted by $y(n)$; The obtained data sequence $y(n)$ that is affected by noise $w(n)$ can be further modeled as

$$y(n) = \sum_{i=1}^{P} a_i p_i^n + w(n)\,,\ n = 1,\dots,N \tag{3. 3}$$

The flowchart of UWB impulse radar signal processing for μ-D features and association of the μ-D frequencies obtained with ST-SSM to specific body joints and the processing steps as indicated by [3.15] can be summarized as follows:

1) Collecting the data (pulses) using the UWB impulse radar system;

2) Applying a matched filter to maximize the SNR of the received signal (collected pulses);

3) Removing the static background by subtracting the mean of the data from the original collected data; therefore, the trajectories from walking subject can be highlighted in HRRP;

4) Applying fast Fourier transform (FFT) to each pulse along the fast-time (range) axis and acquiring a complex value for each pulse;

5) Applying arctangent demodulation process [2.19] to achieve phase information associated with motions (the phase of each complex value);

6) Differentiating the phase values along slow time for μ-D features overview;

7) Applying ST-SSM to the complex values of step 5 and finding μ-D frequencies (velocities) from human body joints;

8) Sorting the μ-D frequencies based on the descending order of Boulic model and detect strides from μ-D features along slow time;

9) Correlating μ-D frequencies with specific body joints.

However, this method was only limited to extract the velocity of torso, left foot, and right foot, as the utilized pulse repetition frequency (PRF) of this UWB impulse system was relatively low (only 75 Hz) [3.15]. Therefore, we were not able to track other body joints that are faster or typically have weaker return signals. Hence, there have been a need for higher PRF to track other relatively faster body parts movements resulting in a sophisticated hardware and huge data sizes that would result in a very expensive computational cost and consequently much longer processing time. Figure 3.2 shows time-frequency spectrogram for a walking person detected by the UWB impulse radar and tracking only torso, left foot and right foot. Moreover, due to the low PRF of UWB impulse radar and according to the Nyquist Theory, in the experiments the subject has to walk with the velocity of less than 0.40 ms^{-1} [3.15].

3.4.2 Gait Analysis using Continuous-Wave (CW) Radar

To extend gait analyses to other limb joints using state-space method (SSM), a CW radar operating at 3.5 GHz was initially developed in our lab in 2018 using software-defined radar (SDR) by Farhan Quaiyum [3.5]. CW radar is simple and does not have the limitation of PRF. He has used an enhanced SSM, i.e. 1-D block SSM on one-dimensional data string

collected using CW radar, to extract the velocity of each body component. In a CW radar, since the data is collected at one single frequency, the collected data can be modeled as (3.4) which means the data sequence is a one-dimensional data vector. Below the instructional steps to track limb joints using the 1-D block processing algorithm from data collected by a CW radar are summarized [3.5]:

1) Select a model order or number of poles that represents the number of signals or joints to track. The employed technique to estimate the model order is to look for a knee in the plot of the singular values computed from the singular value decomposition (SVD) of the Hankel matrix. Typically, this number is smaller than the number of desired joints to track. Examples of this technique being implemented are shown in the results section.

2) Due to the non-linearity of the data, choose the block size or the sliding time window to lie over a fraction of one normal motion period of a human gait to achieve adequate timing and frequency resolution. For example, if a particular motion lasts for 0.6 s in one direction, start with a time window size of half that period and decrease the window size gradually if required.

3) Form the Hankel matrix from the 1-D data string and computing the state transition matrix.

4) Calculate the eigenvalue decomposition of state transition matrix to obtain the damping factors a_i and frequencies f_i.

5) Model the data vector or fit from the λ_i computed from the radar data for all the eigenvalues.

6) For complex motions where tracking of many signals may be needed, the model order can be chosen to capture the stronger signals first.

Next a data residual is extracted by subtracting the fit (derived from the poles or eigenvalues and amplitudes of the stronger signals) from the original data then repeat steps 3-5 with appropriate model order.

7) Repeat step 6 until all the desired limb joints are identified.

8) Since there will be more extracted features than the desired number of joints to track, identify the appropriate features by comparing the extracted results with the reference Boulic motion model and separate the correct ones by a nearest neighbor approach.

Figure 3.3 shows the results for a simple motion when a subject walking without hand motion. It can be seen from Figure 3.3 that in the results the maximum velocity for each body joint is in good agreement with results from Boulic model and also simulated results. Farhan extended the experiments to more complex motions like walking with both hands swinging. Figure 3.4 shows the results.

However, from the results we can see that the trajectories of simple motions were easily tracked, but when complicated motion evolved, it was obvious that CW became less insightful. For example, for motions including more scatterers such as walking, there are significant discrepancies between simulated and measured results for each trajectory.

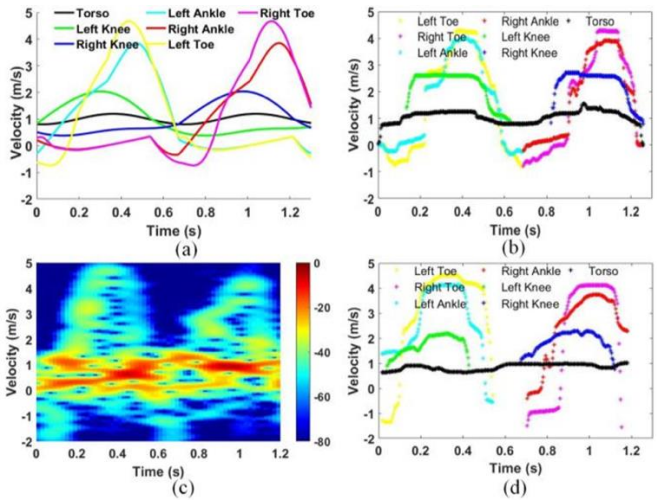

Figure 3.3 Tracking torso, toes, ankles and knees of a subject walking without hand motion (a) Boulic model; (b) Extracted features using 1-D block with EM simulation data; (c) Spectrogram using STFT from measured radar data; and (d) Extracted features using 1-D block. with measured radar data [3.5].

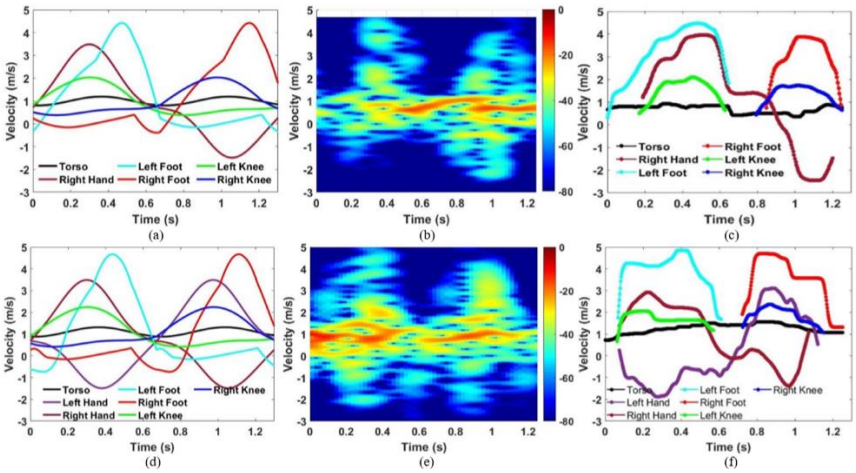

Figure 3.4 Tracking torso, legs and right hand for a subject walking with only right hand swinging (a) Boulic model; (b) Spectrogram using STFT; (c) Extracted limb joint velocities from measured data using 1-D block method; (d) Boulic model; (e) Spectrogram using STFT; and (f) tracked limb joints from measured data using 1-D block for a subject walking at about 1.1 ms-1 with both hands swinging [3.5].

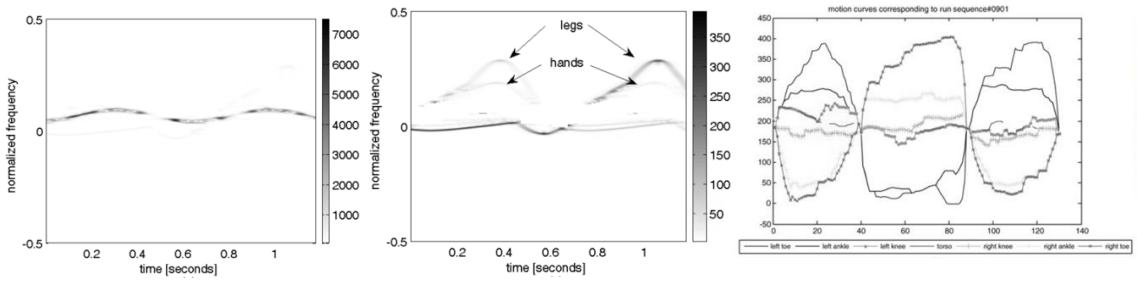

(a) (a) (b)

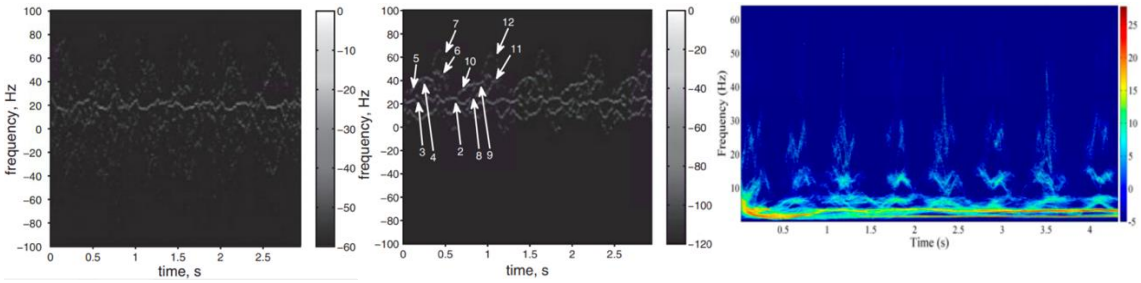

(c) (c) (d)

Figure 3.5 (a) Gait analysis results for a walking subject reported in [3.17] using an 8.9–9.4 GHz SFCW radar; (b) Analysis performed in [3.25] using simulated UWB radar data for identifying only the torso and lower body parts of a walking subject; (c) Motion analysis results reported in [3.26] where identification done for the legs, hands and torso trajectories from simulated data of a walking subject; (d) MHHT-based spectrum of the activity of piaffing [3.8].

Table 3.2 Comparison of Other Reported Works on Limb Joint Tracking for A Walking Human Subject.

Ref.	**Problem and Challenges**
[3.17]	The extraction of the complete hand swing is not possible.
[3.25]	Only the torso and lower body parts are extractable.
[3.26]	Results from measured data are difficult to interpret.
[3.9]	Only parts of motions with positive velocities can be extracted. Negative velocities are not detectable; and the results spectrum is noisy.

3.4.3. Other Investigations on Human Gait Analysis using Radar Techniques

On the other hand, there are other techniques employed by other researchers in order to extract human gait features. The results from the major existing works on limb joint tracking for a walking subject using radar techniques are shown in Figure 3.5.

Table 3.2 summarizes the results from these major reported works on human gait analysis and the main challenge of each approach.

3.5 Conclusion

As it can be seen from the results of STFT, ST-SSM, 1-D block processing on 1-D data vector, and other major techniques for human gait extraction, it is obvious that in order to extract μ-D features of different body components of a walking human subject separately and precisely, both data type collected by a radar system and signal processing scheme play key roles in achieving these objectives. In Chapter Four, radar hardware design and implementation to collect reliable data proper for associated signal processing algorithm will be explained. The developed signal processing technique will be described in Chapter Five, and the results will be represented in Chapter Six.

CHAPTER FOUR
HARDWARE DEVELOPMENT

As mentioned in Chapter Three, in order to extract accurate human gait features in a complex motion such as walking, we need to collect reliable data using a proper type of radar system.

As represented in the previous chapter, the 1-D block processing was employed on the collected 1-D data vector using the CW radar, but with modest success [3.5]. In that case, trajectories of simple motions were easily tracked, but once complicated motion was considered, CW radars became less insightful. Therefore, in this work the 1-D block processing technique has been enhanced to utilize 2-D input data, and is developed to analyze a 2-D data matrix to tackle the restrictions faced by the CW radar [3.5] with 1-D vector data. Moreover, using 2-D data matrix enables us to form range profile to separate different subjects in the scene in case of multi-subject scenarios. Therefore, a wideband radar type is needed to meet these requirements.

Generally, there are different wideband radar types that provide range information; and they can offer multi-subject tracking capability as well. One example, is the ultra-wideband (UWB) impulse radar in which a signal with a large instantaneous bandwidth can be employed [3.15]. A second option is the SFCW radar [2.11] with a linearly stepped frequency to cover a wide bandwidth. A third is a frequency modulated continuous wave (FMCW) radar, which emulates a wideband signal by continuously sweeping frequencies over a wide frequency range. It is worth mentioning that SFCW radar is a special case of FMCW radars.

However, a UWB impulse radar system requires a high-performance fast analog-to-digital convertor (ADC) with high sampling rate or a sophisticated equivalent time sampling in the receiver to capture the data signal. However, just recently some impulse radar chips have been developed; but still need to be explored further [3.7]. Alternatively, SFCW or FMCW radars can be utilized. Here we adapted SFCW radars as they have an instantaneous narrow bandwidth combined with a wide effective bandwidth, implying that the hardware has less strict requirements. The radar provides a high range resolution, wide dynamic range, low noise figure, high mean power, a single- or multi-frequency processing, and provides a possibility of using compressive sensing methods [1.28].

As described in Chapter Two, we developed a SFCW radar system with a pulse repetition frequency (PRF) of 20 Hz [2.11]. The SFCW radar was successfully used for human vital sign detection [2.11], human fall detection [3.7], motion classification, and synthetic aperture radar (SAR) imaging. But, it failed in detecting relatively fast moving body limb joints, as the radar's PRF must be no less than the maximum measurable Doppler frequency shift caused by the motion with respect to the operating frequency. Subsequently, we needed to develop a radar system with adequate PRF to retrieve the velocity of the fast-moving body parts [3.8]. A SFCW radar system is designed to achieve up to 200 Hz PRF and has been used for single- and multi-subject gait analysis purposes.

Hence, in this work we will use SFCW radar that has adequate PRF to collect 2-D data that will be utilized as the input of an enhanced 1-D block processing technique; details will be descried in Chapter Five for retrieving human gait features in a multi-subject analysis.

4.1 Towards SFCW with Fast Frequency-Switching Rate

The SFCW radar shown in Figure 4.1, also called frequency-domain radar, generates a set of N consistent CW pulses whose frequencies rise from one pulse to the next by a fixed frequency step size Δf. Therefore, the frequency of the n^{th} pulse is,

$$f_{n-1} = f_0 + (n-1)\Delta f \tag{4.1}$$

where f_0 indicates the initial carrier frequency. Therefore, every frame of the signal includes N frequency steps.

In this work, we have developed a SFCW radar system operating from 3 GHz to 4 GHz with a fast PRF exceeding twice the highest Doppler frequency of potential human activities investigated. Converting the velocity component of movement into Doppler frequencies identified by SFCW radar with a center frequency of f_c GHz, we have

$$f_D = 2vf_c/c \tag{4.2}$$

where f_D denotes the Doppler frequency, v is the velocity of the moving component, and c indicates the speed of light. To step the frequency and generate the chain of frequencies forming frames, we have used a direct digital synthesizer (DDS) based scheme [2.11]. The number of frequency steps, the start and stop frequencies, and the step interval are all adjusted through programming of an FPGA board that controls the DDS.

In order to meet the hardware requirements, we programmed the DDS board to generate the frequency steps with a relatively high rate. Moreover, we used a fast switching phase-locked loop (PLL) with very short settling times, and an analog to digital converter (ADC) with fast sampling rate to capture the data.

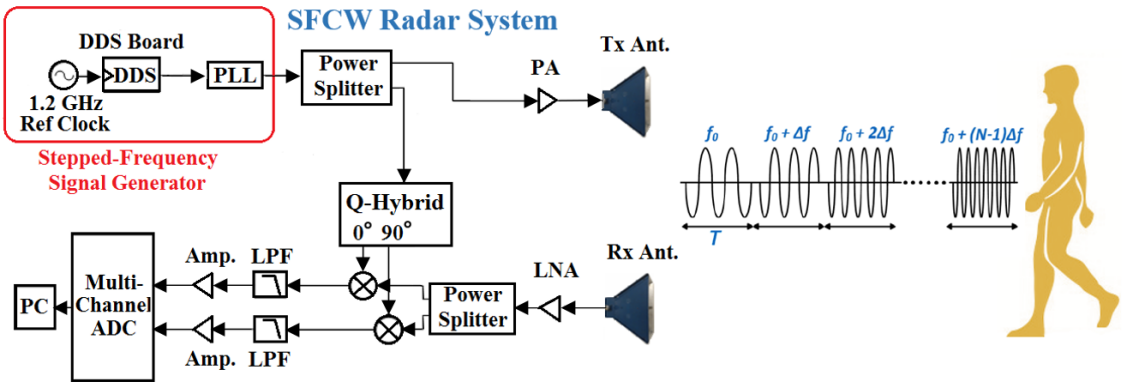

Figure 4.1 Block Diagram of a SFCW Radar System Detecting Human Motion.

Table 4.1 SFCW Radar System Parameters

Parameter	**Value**
RF Frequency Range	3-4 GHz
Operation/Center Frequency (f_c)	3.5 GHz
Total Bandwidth (BW)	1 GHz
Frequency Step Size (Δf)	20 MHz
Number of Frequency Steps in One Frame (N)	50
Frame/Pulse Repetition Frequency (PRF)	200 Hz
Sampling Rate	50 kHz

4.1.1 Pulse Repetition Frequency (PRF) Requirement for Human Gait Analysis

The minimum PRF requirement for radar is determined by Nyquist theorem. To be able to detect the motion and retrieve the velocity of a moving target, according to the Nyquist theorem, the PRF of the system needs to be at least twice the maximum Doppler shift (Doppler frequency (f_D)) caused by that motion. And according to (4.2), this Doppler frequency depends on the center frequency of the radar system.

This frequency (f_D) is also known as Nyquist frequency, which is half of the PRF of the system. Therefore, for a system with lower center frequency (f_c), the Doppler shift caused by the moving velocity of v (m/s), is lower than the Doppler shift caused by the same moving velocity for a system with higher center frequency. And consequently, based on Nyquist theorem, the minimum required PRF for the system with lower center frequency to grasp motions with that velocity will be smaller.

To show the validity of (4.2), in radar systems with the center frequency of f_c, the transmitted signal is reflected by a target and then demodulated in the receiver. It is used to determine the target's speed. If $D = do + d(t)$ is the distance from the radar to the target, the total number of wavelengths λ contained in the two-way path is $2D/\lambda$. Since one wavelength corresponds to an angular excursion of 2π radians, the total angular excursion φ traveled by the electromagnetic wave is $4\pi D/\lambda$ radians. If the target is moving, D and the phase φ are changing continuously. A change of φ with respect to time is equal to a frequency, such as the Doppler angular frequency ω_D is:

$$\omega_D = 2\pi f_D = \frac{d\varphi(t)}{dt} = \frac{\varphi(t)}{\lambda}\frac{d\,(d(t))}{dt} = \frac{4\pi v(t)}{\lambda} \tag{4.3}$$

where $v(t)$ is the radial target speed. The Doppler frequency shift is therefore

$$f_D = \frac{2v(t)}{\lambda} = \frac{2v(t)f_c}{c} \tag{4.4}$$

Thus, a velocity of 1 ms^{-1} detected by a radar with operating frequency of 2.45 GHz would correspond to a Doppler frequency shift of about 16.33 Hz. We can also see that as we increase the operating frequency, larger Doppler frequency shifts are generated which increases the sensitivity [1.25], [4.1].

Meanwhile, analysis of the human gait or body joint velocities from a human walking (Boulic) model explained in [2.11], [4.2] reveals that in a normal walking activity, the velocity of the torso is the average speed of walking. While, the highest velocity component is generated from the toes' motion. For instance, for a subject with a height of 1.6 m, the maximum velocity components caused by the toes' trajectories are about 4.3 ms^{-1}, assuming an average speed of 1 ms^{-1} for walking. When the average walking speed varies, then the velocity of the toes is scaled accordingly. Translating these velocity components to Doppler frequencies detected by the SFCW radar system with a carrier center frequency of 3.5 GHz using (4.2), we can realize that the maximum Doppler frequency, caused by toe movement, is about 100 Hz. Therefore, for correct detection of the Doppler frequency of the toes, the PRF of the system needs to be 200 Hz. In this case, the radar PRF depends mainly on the settling/dwell time (T) of each frequency step. Therefore, we need to increase the stepping rate of the reference signal generated by the DDS board to generate frequency steps with a faster pace and consequently increase the frame rate; where the DDS board generates this reference stepped frequency signal. The reference signal is then multiplied by a programmable factor in a PLL to produce the RF signal and extend the bandwidth of

the signal generated by DDS. Every time the frequency of the reference signal is changed (stepped), the PLL needs to get locked onto that new frequency according to the multiplier that has been set. As a result, we need a fast switching PLL to be able to lock onto each frequency step very quickly. In fact, the minimum step interval is mainly restricted by the lock time of the PLL.

In fact, in SFCW radar, the selected dwell time (internal pulse interval) should be enough to capture the returned signal after a round trip to at least the maximum unambiguous range typically. This should be adequate to allow capturing stable samples. Meanwhile, the coherent processing interval (CPI) is N (N=50) times the dwell time assuming it is uniform for all frequency steps, and the pulse repetition frequency is 1/CPI. While CPI is related to the Doppler frequency shift range, which is double the maximum Doppler frequency shift here as parts go closer and further away from the radar with the same maximum speed;

The description of the utilized components is given below and the characteristics of the utilized SFCW radar is summarized in Table 4.1.

It is worth mentioning here that the maximum theoretical unambiguous range in the implemented SFCW radar system is 7.5 m according to the following formula:

$$R_{max} = \frac{c}{2\times\Delta f} = \frac{3\times10^{8} m/s}{2\times20\times10^{6} Hz} = 7.5\ m \tag{4.5}$$

where c indicates the speed of light and Δf is frequency step size in the implemented SFCW radar system (here 20 MHz).

On the other hand, the returned echo corresponding to a frequency step must be overlapped in time with the replica of such frequency step so that the mixing process is correct.

Considering this limitation, the real maximum detectable range of targets in the implemented SFCW radar system is about 6 m for a discernable data.

4.1.2 Fast-Switching Phase-Locked Loop (PLL)

We utilize the ADF4152HV PLL from Analog Devices [4.3], right after the DDS board output to generate the RF (3-4 GHz) stepped-frequency signal. The ADF4152HV does not have an internal frequency stepping feature; hence, we use it right after the DDS board that is programmed to generate the fast sweeping stepped-frequency reference signal. This PLL can produce the frequency step rate that we need and is a fast-locking fractional/integer multiplier PLL synthesizer with a lock time less than 50 µs. Moreover, ADF4152HV evaluation board includes a USB interface to connect to a computer for locking and board configuring commands using software; therefore, no external UWB interface is needed.

4.1.3 Reference Signal Routing

As previously mentioned, we employed a DDS board to drive the PLL and provide the stepped-frequency reference signal. This reference signal is then multiplied by the PLL multiplier factor (N) to produce the RF output with wider bandwidth. Although the ADF4152HV evaluation board has an internal fixed reference signal provided by an on-board 25 MHz crystal oscillator (Y1 in Figure 4.2), it also has a REFIN port to be connected alternatively to an external reference signal. In this case, the REFIN is connected to the DDS board output. Therefore, we needed to modify the evaluation board of the PLL to disconnect the routine path from the crystal oscillator and guide the reference signal from the REFIN port. This is done by removing R100 and R101 to disconnect the crystal oscillator from the voltage supply and necessary routing path.

4.1.4 External Voltage-Controlled Oscillator (VCO) Replacement

The ADF4152HV has the footprint for an external VCO already. Since the VCO that comes with the PLL evaluation board is a 1-2 GHz VCO, and we needed to make a RF signal with 3-4 GHz frequency, we replaced the VCO and implemented modifications in the board to be able to use this new VCO. We selected a VCO from Synergy, the DCYS200400-5 [4.4], which can cover a frequency range of 2-4 GHz and is compatible with the PCB footprint. Because the new VCO needs a supply voltage of 5 V, we needed to provide 5 V from the chip voltage supply with a tuning range of 0.5-16 V which is determined by the on-chip charge pump. Therefore, we needed to adjust the voltage regulators to provide the correct supply voltages for both the VCO and the charge pump.

4.1.5 PLL Loop Filter Configuration

Since one frame of the generated signal by the DDS board consists of 50 frequency steps, in order to have a PRF of 200 Hz we needed to attain a settling time of 100 µs for each frequency step and a PLL lock time of about 50 µs. The ADF4152HV is a fast PLL which is capable of achieving such short settling and lock times; however, it cannot reach the short lock time required for our desired PRF with the default configurations. As a matter of fact, both lock time and stability of the PLL rely on the loop filter configuration which we will need to modify as well for our application. Figure 4.3 shows the basic PLL structure including the main components inside the feedback loop.

As seen from Figure 4.3, the feedback loop consists of a phase detector (PD), a charge pump (CP), a loop filter, a VCO, and a frequency divider. The feedback structure has been designed to make the error signal approach zero to keep the phase and the frequency

constant (locked to the intended frequency). The phase detector tracks the error signal and drives the charge pump. The charge pump generates the tuning voltage for the VCO, accordingly. The higher frequency contents of the error signal are filtered out by the loop filter, which is mainly a low-pass filter. Here, there is a trade-off between stability and lock time. Stability depends on the loop bandwidth of the feedback route which is set by the loop filter cut-off frequency. A larger loop bandwidth makes the settlement to the lock condition faster, but it can also make the system less stable, while a small loop bandwidth increases the lock time. For an optimum lock time performance, we maximized the loop filter bandwidth while keeping the phase margin of the system greater than 45° to maintain stability [4.5], [4.6]. We used the ADIsimPLL software from Analog Devices [4.7]; to design the optimal loop filter. It allows us to modify the loop filter configuration and several design parameters such as VCO sensitivity, phase margin, loop bandwidth, and the value of the lumped components. Therefore, the user can tune and optimize the design to meet precise design requirements. The software enables us to construct a PLL by identifying the frequency requirements of the PLL, then choosing the PLL and VCO chips from the library, as well as, a loop filter selected from a variety of topologies. When we run the analysis of the configuration on the software for the evaluation board's default loop filter settings, the exhibited loop bandwidth is 15.9 kHz, the phase margin is 45.8° and the lock time is about 4 ms as shown in Figure 4.4. However, by changing the configuration of the loop filter, we can get the loop bandwidth up to 172 kHz with a phase margin of 46.6° which helps in achieving a lock time of about 30 μs as depicted in Figure 4.5. Therefore, we implemented a new loop filter on the PLL evaluation board to complete the PLL system with a fast frequency-switching capability. As it can be seen from Figure 4.5,

by removing capacitances C3 and C4, the lock time has decreased dramatically, but the frequency response is not as sharp as before due to the removal of the next stages of the loop filter. As a result, during the lock time period, i.e. transition region, the PLL may lock to undesired frequencies, generating unreliable signal samples. However, VCO/PLL phase noise is a major concern in the performance of the radars. By widening the bandwidth, phase noise increases from -124.8 dBc/Hz to -116.4 dBc/Hz at 10 kHz offset, due to the larger operation range.

4.1.6 Analog-to-Digital Convertor (ADC)

The last important part of the hardware structure of the high-performance SFCW radar system is an ADC to sample and digitize the received baseband signal. We utilized the USB-205 eight-channel and 12-bit ADC from Measurement Computing (MC) [4.8] that can collect 5 samples of each frequency step as voltage values, done at 50 kHz (sampling rate) (or 20 μs intervals). Each sample is then stored instantly to the computer using USB, before the next sample is made, which saves an additional data transfer time, as was required by previously reported equivalent time sampling systems in [1.17], [3.15]. Once the data capturing is finished, we still need to use a suitable method to select the best and most reliable sample of each frequency step made by the PLL and implement the consequent signal processing technique to extract the velocities of different body components. In summary, by using this method of signal generation, we could achieve the targeted PRF (200 Hz) that will be adequate to detect a maximum Doppler frequency of ± 100 Hz generated by any fast-moving body components.

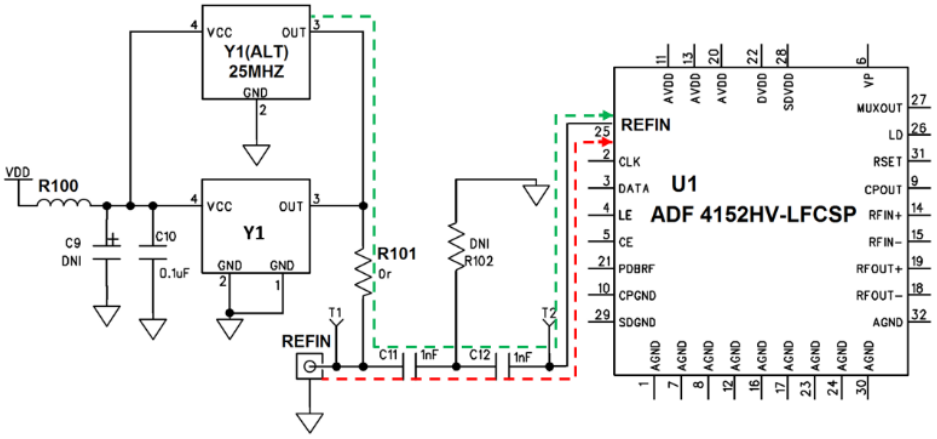

Figure 4.2 PLL evaluation board (Reference signal routing). Green path denotes the default path and red one shows the intended path to the external reference signal source.

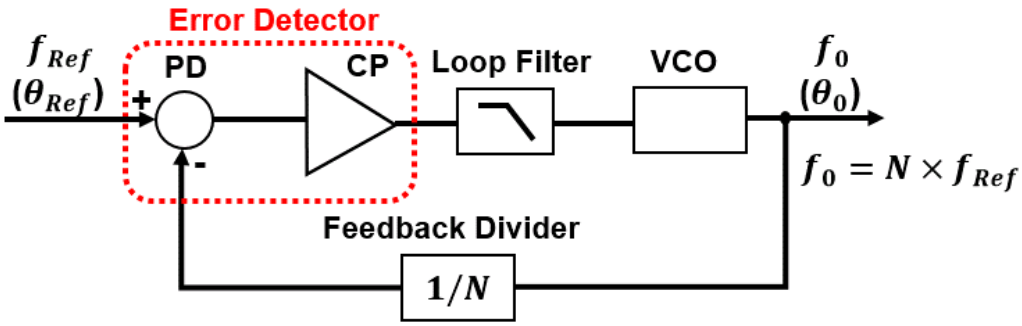

Figure 4.3 General block diagram of a PLL; (PD and CP stand for phase detector and charge pump, respectively).

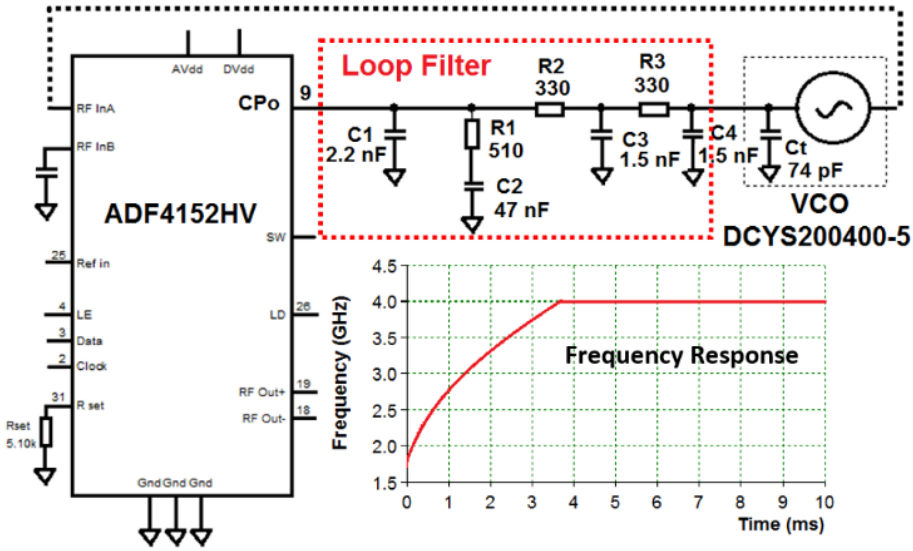

Figure 4.4 Schematic of the PLL with the original loop filter configuration demonstrating frequency response.

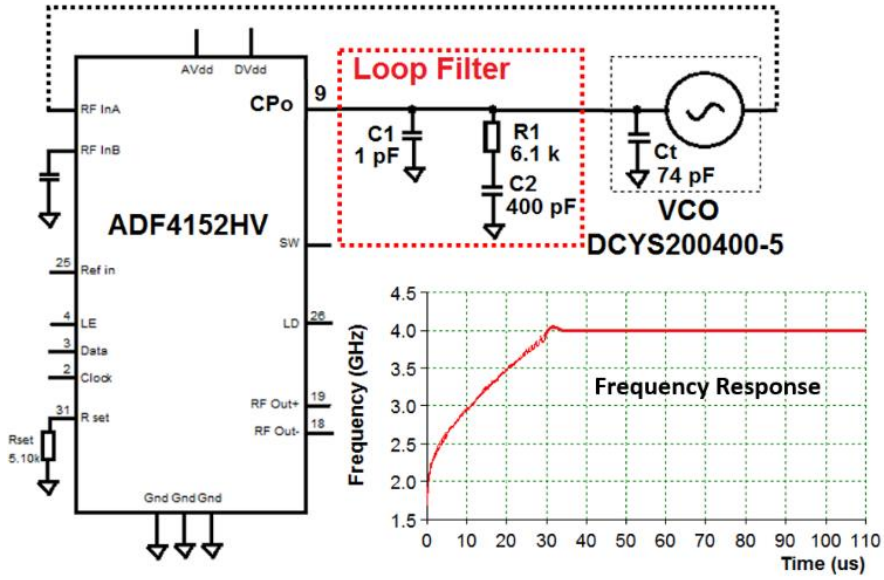

Figure 4.5 Schematic of the PLL with the newly designed loop filter configuration demonstrating frequency response.

4.2 Adaptive Data Decimation Algorithm

In our SFCW radar system, the PLL takes five samples of each frequency step, so, before using the data to be processed by the gait analysis algorithm, we have chosen to decimate the data first and then reshape it using the best sample from each frequency step. In Figure 4.6, the left panel shows time-frequency representation of the SFCW signal including the best sample chosen out of five samples for each step, while the right picture indicates decimated sampled stream reshaped into the frames comprising 50 frequency steps (20 MHz/step).

In order to decimate the data and obtain the most reliable frequency sample, we use the fact that once the PLL settles, the I/Q samples should remain relatively constant until the PLL moves to the next frequency.

We have created an offline decimation algorithm (a collaboration with MaXentric LLC; the algorithm has been developed by Bardia Ghajari), that is designed to choose the most reliable frequency sample for a SFCW radar given no synchronization strategy between transmit and receive blocks. However, there are two problems associated with the SFCW radar with no synchronization; the first problem is that the ADC will capture sample points even when the DDS board is not fully settled resulting in invalid data samples. The second problem is that time alignment cannot be maintained when a DDS and ADC do not share a common reference clock. Due to this fact, samples associated with a given frequency could be non-deterministic, making a simple decimation process difficult to implement.

Figure 4.7 illustrates these two problems in a time domain capture of a SFCW radar signal where there are 5 samples per frequency step. Where we see, outlined in yellow braces,

approximately three valid samples associated with each frequency step. However, we also see there are transition samples between them. This is because the ADC path is still capturing even when the PLL has not settled yet. Further, due to the clock frequency difference, transition samples drift in time; thus, choosing every 5^{th} sample will eventually lead to errors even if capturing begins on a valid sample.

The solution is to create an adaptive down sampling algorithm that chooses the settled sample in the flat region for each frequency step. A sample can be determined to be settled if there is a minimal slope, i.e. “flat”, before and after that sample. This can be shown in a time domain capture in Figure 4.7, where the ideal sampling region is indicated with a yellow outline. The red x is the center sample in the “flat” region where the slope between adjacent points is minimized. This algorithm is inspired by a modified early-late gate algorithm from symbol recovery theory [4.9].

The algorithm starts by identifying the first sample index. This is accomplished by determining the sampling phase, which is the average of the most settled in the first 400 samples. First, we obtain the indices associated with 1 to n sampling phases of the first 400 samples. From here, the algorithm calculates the slope between adjacent points of each sampling phase index to determine which sampling phase produces samples that are in the flat region. This is accomplished by computing early and late errors for each of the sampling phase indices. Early error is defined as the absolute value of the difference between the current sample and the previous one. Late error is defined as the absolute value of the difference between the current sample and the next one. The minimum of the early and late errors of each sampling phase set is obtained and then averaged across each

sampling phase. The phase that has the least computed error is determined to be the best sampling phase. Thus, the first sample's index will be at the first best sampling phase index.

Once the initial reliable sampling point is determined, it is required to determine and maintain the reliable sample for the subsequent frequency steps. This is determined by first computing the sum of the early and late errors for each point of the waveform capture. Using this error values, a loop is constructed such that the flattest point for each frequency step is extracted. This can be accomplished by advancing the first reliable sample index by the number of samples per frequency step, n. This value is called our pointer. If the clocks were locked to the same reference, this would be the next reliable sample and the center sample of the next frequency step; however, due to mismatch, we need to check all the samples of the next frequency step to ensure we are choosing a point in the flat region. To do this, the loop obtains the minimum of the sum of the early and late errors for each sample in that given frequency step. As an example, the samples associated with the given frequency step for $n = 5$ is the index of the previous two samples before the pointer, the pointer value, and the next two samples after the pointer. The index of the minimum error value is recorded as a shift from the current pointer value. The reliable sample for this frequency step and the new pointer is calculated as the sum of the current pointer and the shift pointer. The pointer is advanced again by n and this process repeats until the end of the capture. The outputs of this loop are the indices associated with one reliable sample per frequency step of the capture, in order. Using these indexes, an array of the reliable samples from the capture is obtained. However, sharing a clock between the signal generation (DDS) and ADC could help alleviate the issue.

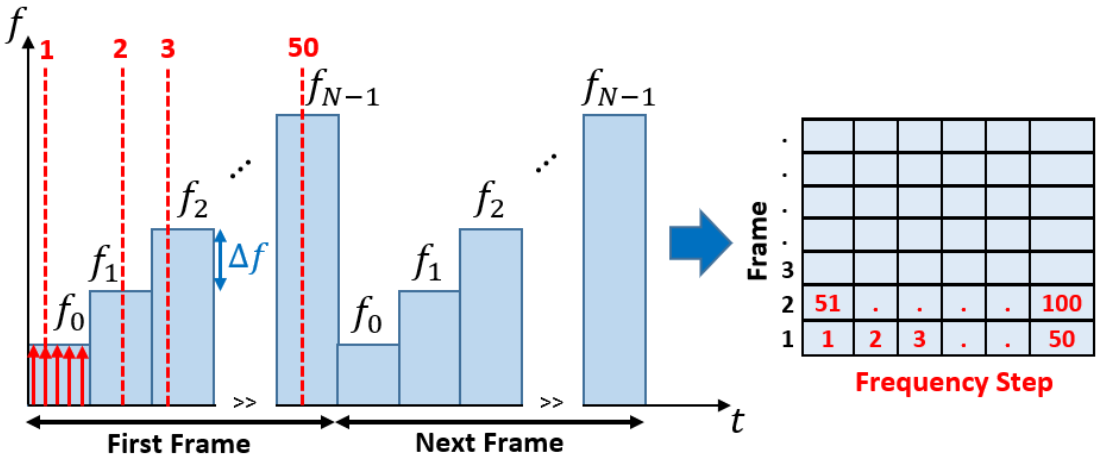

Figure 4.6 Time-frequency representation of SFCW and frame fitting.

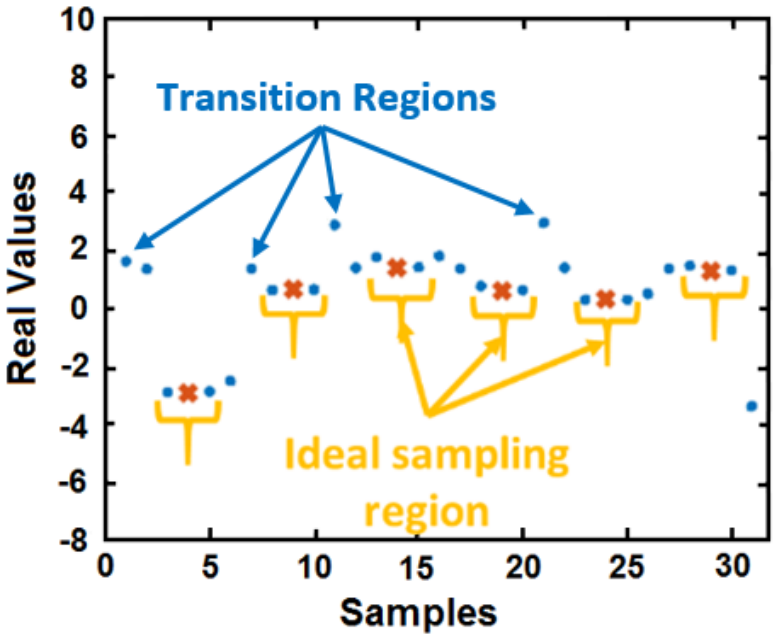

Figure 4.7 Example of adaptive down conversion.

Although in some systems sharing a clock could be challenging, e.g. when transmitting and receiving hardware are physically separated. However, in our SFCW radar system, we shared DDS board clock with the ADC. But our main problem is really the first one; where the ADC will capture sample points even when the generator (DDS + PLL) is not fully settled resulting in invalid data samples. It means the ADC path is still capturing even when the PLL has not settled. The reason is that the discrete nature of the frequency updates in SFCW signal is smoothed by the loop filter, such that the synthesized waveform is subject to the normal phase locked loop dynamics. If the loop filter bandwidth is lower or comparable with the rate of the CW pulses, then the loop filter will not fully settle before a new frequency is received [4.10]. Meanwhile, in order to have enough PRF we decreased the bandwidth of the loop filter.

In SFCW radar, some of the samples in one frequency step are not reliable because they are located within the settling/transition region. Therefore, we always need a smart way to choose the most reliable sample and make sure this sample is not in the transition region.

To summarize, using the adaptive decimation algorithm to decimate the data and choosing the best sample of PLL is necessary from signal generating aspect. Although this decimation is implemented on the received signal and data by receiver, the main reason that we need it is the transmitting path. As a matter of fact, we generate the SFCW signal in transmitting path using DDS board and PLL and PLL makes five samples of each frequency step. But since this signal is injected to the receiving path as well using a mixer for down-conversion of the RF received signal, we need to implement the adaptive data decimation algorithm on the received signal that has been demodulated using the PLL

output signal. Therefore, either the sample is the first order reflection or the higher order one due to the multi-path effect, we have five of that sample due to the multiplication to the transmitted (PLL output) signal. And consequently, we need to choose one out of five (using adaptive data decimation algorithm). In other words, we have the samples in the transition region of the PLL in the main signal, and all the reflection signals due to the multi-path effect. Since PLL is not fully settled at these regions, the samples will not be reliable. We use the early-late error calculations we described. After finding the first sample (the index and samples associated with the first frequency step), we calculate the early-late error between that sample and the samples of the next frequency step and find the minimum error [4.9]. By choosing the sample that minimizes the early-late error function, it guarantees that it is the best sample. The early-late error in a sense is the difference or slope calculation, but looks at relative differences between adjacent points to determine the "Flattest" point. Obviously, there is a large discontinuity when it switches to the next frequency and where it is not settled. This will be translated to a larger error as compared to the error/slope calculation of the sample that is settled.

4.3 Radar Performance Evaluation

Now that we have a SFCW radar system with high PRF, and the data decimation algorithm to decimate the data properly in order to provide reliable 2-D data matrix as the input of the enhanced signal processing algorithm to extract μ-D features of a single- or multiple-moving subject, we need to evaluate the performance of both the hardware system and the adaptive data decimation algorithm.

4.3.1 Data Decimation Algorithm Validation

To validate the effectiveness of the adaptive data decimation algorithm, we have setup an experiment using a programmable actuator placed in front of the developed SFCW radar. Meanwhile, all the experiments were conducted in the indoor environment of the lab. The actuator is programmed to create a triangle (saw tooth) motion waveform with a motion frequency of 0.5 Hz and an amplitude of 2 mm. We then collect radar backscattered signals from the actuator using the developed high-performance SFCW radar.

Afterwards, the data was analyzed to retrieve the high range-resolution profile (HRRP), the displacement waveform, and the spectrum of the motion in two different scenarios: in the first scenario we do not decimate the data using the adaptive algorithm and process the raw data collected from the radar by choosing a fixed sample for each frequency step (e. g. the third sample); while in the second scenario, we decimate the data using the adaptive data decimation algorithm to choose the best sample for each frequency step and then process the decimated data. The results from both situations are shown in Figure 4.8.

As seen from the results shown in Figure 4.8, when we choose a fixed sample for all frequency steps, the HRRP is not clean, the displacement signal does not show the correct motion pattern (triangle waveform), and consequently we cannot retrieve the correct motion frequency (0.5 Hz) of the actuator. It is because we have chosen a fixed sample for all frequency steps and some of these samples are inside the transition regions, where the PLL has not settled completely yet on the correct frequency and therefore, the data will not be reliable. While using the data set acquired from the adaptive decimation algorithm, the results confirm that the reliable samples inside the ideal sampling region have been chosen.

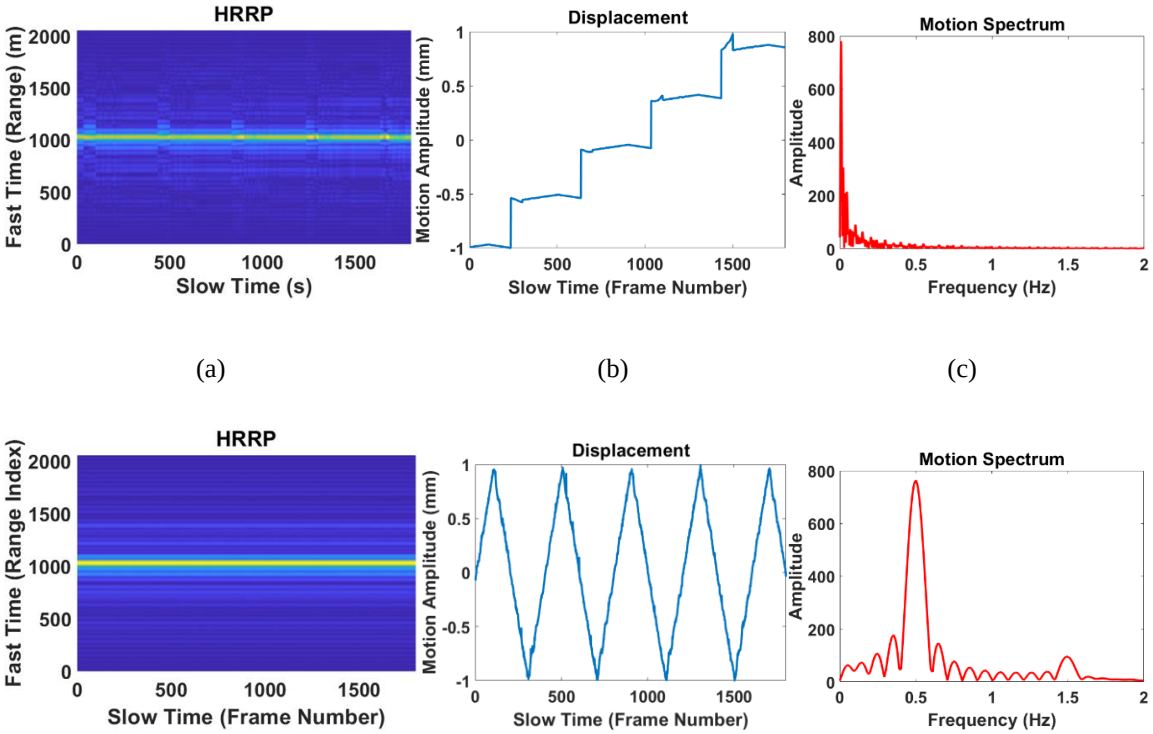

Figure 4.8 First scenario: (a) HRRP, recognizing the actuator range; (b) Motion Pattern (actuator displacement); and (c) Spectrum of the actuator motion. Second scenario: (d) HRRP, recognizing the actuator range; (e) Motion Pattern (actuator displacement); and (f) Spectrum of the actuator motion. Hence, we have a clean range profile leading to a correct motion pattern and frequency measurement.

4.3.2 SFCW Radar Performance Evaluation

In order to evaluate the performance of the SFCW radar system with a fast frequency stepping rate equipped with a data decimation algorithm, we were able to extract gait velocities. We utilized an experimental setup, where a human subject stands facing the radar antennas and makes a motion or activity with a gradually increasing velocity. To achieve this, the subject swings only one hand back and forth slowly, and then gradually increases the velocity of the swing. The SFCW radar system collects the data at a PRF of 200 Hz. Next, we decimate the data using the adaptive data decimation algorithm. Afterwards, we apply a simple motion analysis technique, the short-time Fourier transform (STFT) method on the 2-D decimated data matrix to generate the time-frequency spectrogram. Figure 4.9 shows the experimental environment and setup and Figure 4.10 presents the STFT spectrogram for the experimental setup, just described.

From the demonstrated results in Figure 4.10 we can see that the spectrogram is clean and we can extract the Doppler frequency of hand movement successfully for low velocities. As shown, by gradually increasing the speed of a swing, the maximum frequency related to the speed also increases-- while the time intervals between them decreases, which validates proper system performance. It can immediately be observed that the plot frequency range is limited to ± 100 (half of the radar PRF). In the beginning, when the hand motion is slow, we are able to clearly see a complete swing. By increasing the velocity of a hand swing, the related Doppler frequencies start to exceed the limited range (± 100 Hz) and the spectrogram collapses.

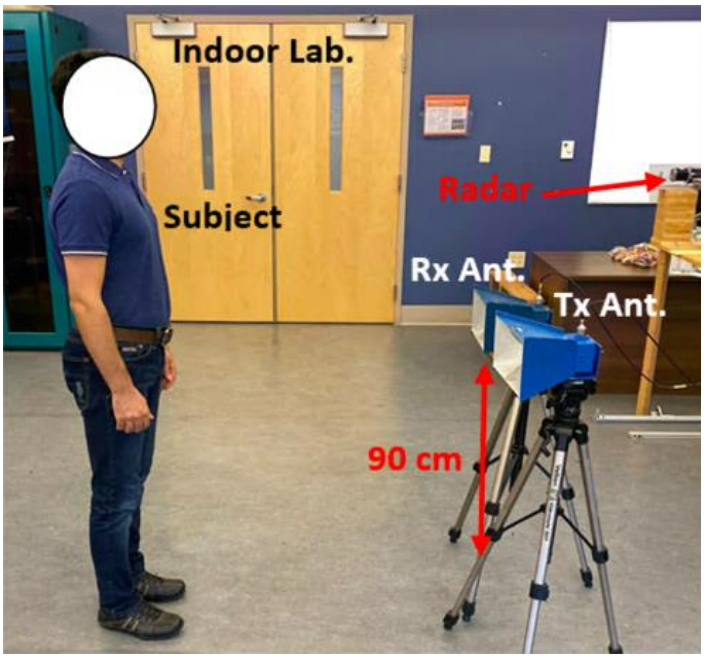

Figure 4.9 Experimental setup for gait analysis using SFCW radar in an indoor lab environment.

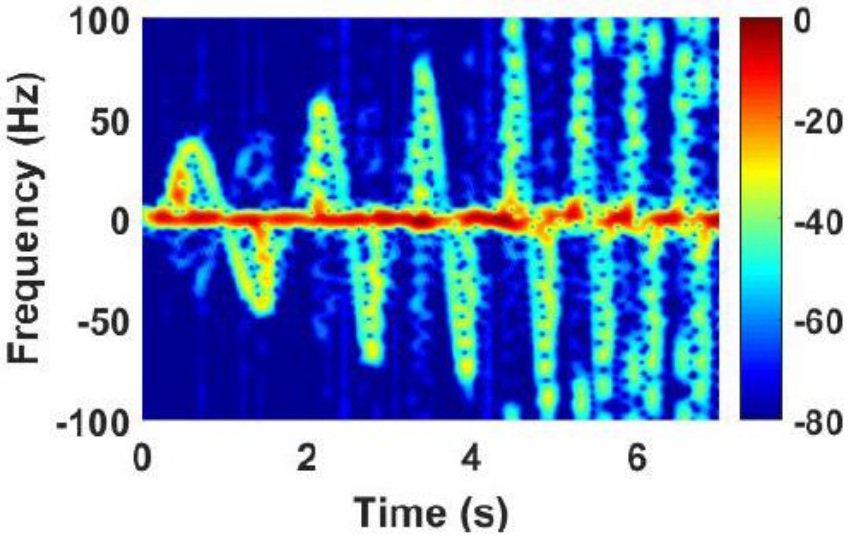

Figure 4.10 STFT spectrum of the 2-D data collected using SFCW radar when the subject stands and swings only one hand while increasing the speed of swing gradually.

As mentioned previously in the walking experiments, the maximum velocities created by the fast-moving components of the human body are within the limits of the detectable Doppler frequency generated from the associated motions. Therefore, a PRF of 200 Hz is adequate for our gait analysis purposes, i.e. walking here.

4.4 Conclusion

Various types of wideband and UWB radar systems have been developed which can be used for human gait analysis. Major wideband radar systems utilized for gait analysis are listed in Table 3.1 in Chapter Three. In this table the type of radar, the operating center frequency of the radar, the radar bandwidth, and the PRF are listed as well. Table 3.1 indicates that our developed SFCW radar system has a high PRF (suitable for human gait analysis), high range resolution and wide bandwidth (suitable for multiple-subject detection). Additionally, it provides clean and reliable data with acceptable data sizes for processing and there is no need for expensive components such as high-speed ADCs or FPGAs, nor does it need any complicated calibration.

The newly developed SFCW radar system achieves a relatively high PRF of 200 Hz which is suitable and adequate for detecting Doppler frequency shifts up to ± 100 Hz. Since the produced Doppler shift depends on the operating center frequency of the radar, the maximum detectable velocity by this developed radar with 3.5 GHz center-frequency and PRF of 200 Hz is 4.3 ms^{-1}. This setup is suitable for demonstrating walking experiments, where we consider a walking speed of around 1 ms^{-1} or less (human normal walking speeds) so that the maximum velocities caused by the fastest body-moving components are within the PRF limit.

However, there are two problems encountered with this SFCW radar system if no strategy to synchronize the transmitter and receiver is employed. The first problem is that the ADC captures the sample points before the DDS settles; thus, rendering invalid data samples. The second issue is if there is no common reference clock to be incorporated in the system, then no time alignment can be maintained between the DDS and the ADC circuitries. Thus, a strong decimation technique of the SFCW data is required for data alignment, which was introduced in this work.

Upon addressing the above challenges, the high-performance SFCW radar is ready to provide the decimated 2-D data matrix to be processed using robust techniques for gait analysis. Moreover, with a 1-GHz bandwidth, the range resolution capacities of this SFCW radar should be capable of tracking multiple-subject motions. Detailed results of such a multi-subject tracking investigation will be presented in the next two chapters of this study, where we develop a robust signal processing technique and use the reliable data obtained by the high-performance SFCW radar to extract motion velocities from different body components in single- and multiple-subject motion scenarios.

Details of our signal processing methods will be explained in Chapter Five and experimental validation results will be discussed for both single- and multiple-subject motion scenarios in Chapter Six.

CHAPTER FIVE
SIGNAL PROCESSING SCHEMES

As mentioned in Chapter Three, in order to detect multiple subjects and analyze human gait in multi-subject motion applications, we needed to use a wideband radar system, operating in a wide frequency range. In Chapter Four, we explained the development of a high-performance, wideband SFCW radar operating within 3 to 4 GHz, with a high PRF of 200 Hz, which is adequate for human gait extraction. It will be shown here, using this 1-GHz bandwidth radar, that the range resolution capabilities of the SFCW radar would be suitable to track multiple subjects' motion as well. Moreover, an advanced data decimation algorithm developed by Bardia Ghajari from MaXentric Technologies LLC, explained in Chapter Four, has been established and implemented to decimate and de-noise the 2-D data matrix collected from moving human subject(s) using high-PRF SFCW radar that prepares it for the signal processing stage for gait extraction.

However, along with using the proper data and radar type, there is a need to use a powerful signal processing method to effectively utilize the data collected by such radars in order to extract human gait features accurately and separate and identify the μ-D frequencies from each moving body component. Most of the signal processing methods and algorithms employ a time-frequency exploration of the backscattered radar signals. However, as mentioned in Chapter Three, due to the capabilities of the state-space method (SSM)-based techniques in extracting and separating the μ-D features of the gait, this following work focuses on a SSM-based technique, noted by the 1-D block processing technique.

Previously, the short-time state-space method (ST-SSM) was successfully used by our group to extract μ-D features of the human body for gait analysis utilizing a UWB impulse radar [3.15]. However, it was limited to extracting the velocity of torso, left foot, and right foot only, as the utilized radar's PRF was relatively low (only 75 Hz) and their signal-to-noise ratio (SNR) were low as well. Therefore, we were not able to track other body joints with fast movement rates; add to that it was hard to extract weak return signals. Hence, there has been a need for UWB radars with higher PRFs to track the other relatively faster body parts' movements and a methodology of isolating strong signals from shadowing weak signals, which would require the use of sophisticated and expensive hardware and handling of huge data sizes.

Initially, to extend gait analysis to other faster limb joints, a CW radar was used in [3.5]. The well-known ST-SSM method was excluded right away for motion retrieval as it requires range profile, while CW radars are known that they do not provide range information. Moreover, due to the heavy non-linearity of CW data, the sinusoidal model used by ST-SSM for estimation is lacking. Alternatively, the 1-D block processing introduced in [3.24] was employed on the collected 1-D data vector using the CW radar, but we had modest success [3.5]. In this case, trajectories of simple motions were easily tracked, but once complicated motion was considered, CW radars became less insightful. Therefore, in this work the 1-D block processing technique is enhanced to utilize 2-D input data instead, provided by the SFCW radar with adequate PRF. enhanced 1-D block is also developed to analyze the 2-D data matrix to tackle the restrictions faced by both the CW radar [3.5] with 1-D vector data, and the UWB impulse radar with low PRF [3.15].

Meanwhile, the human Boulic model [3.15], [5.1] is selected as our reference to validate our experimental results. Results with our new system will be compared with the results published by other researchers as depicted in Table 3.1 in Chapter Three. Additionally, we extended the investigation to multi-subject motion analysis and it will be discussed in this chapter as well.

5.1 Signal Modeling and Data Type

SFCW radar system with a fast stepping rate acquires a set of 2-D data decimated with the adaptive data decimation algorithm [5.2]. Here, the collected data from the SFCW radar from a moving target is a 2-D matrix and when degraded with an input noise $w(m,n)$, it can be represented by

$$y(m,n) = \sum_{i=1}^{P} a_i s_i^m p_i^n + w(m,n), \tag{5.1}$$

$$m = 1, \dots, M \; and \; n = 1, \dots, N$$

where P is the order of the signal, i.e., the number of signals forming the data, M is the number of frequencies, and N is number of data sample points in the corresponding data acquisition time. The spectral pattern of the i^{th} body motion from a human subject is correlated with a pole pair (s_i, p_i) and the complex amplitude a_i which is defined by

$$a_i = |a_i| e^{j\varphi_i} \tag{5.2}$$

where φ_i denotes the phase. The poles s_i and p_i yield the frequencies describing body limb joints movements in the range (r_i) and Doppler frequency (f_i), respectively. These frequencies can be estimated according to

$$r_i = \frac{\theta_i}{2\pi} \; and \; f_i = \frac{\beta_i}{2\pi} \tag{5.3}$$

where θ_i and β_{i} refer to the phase angles associated with s_i and p_i respectively as detailed in [5.3], and [5.4].

Therefore, using SFCW radar system generates a 2-D data signal expressed by an $M \times N$ matrix. Therefore, according to (5.1) we can represent the 2-D data collected by the SFCW radar system as a $M \times N$ matrix defined by

$$Y = \begin{bmatrix} y(1,1) & \cdots & y(1,N) \\ y(2,1) & \cdots & y(2,N) \\ \vdots & \cdots & \vdots \\ y(M-1,1) & \cdots & y(M-1,N) \\ y(M,1) & \cdots & y(M,N) \end{bmatrix}. \tag{5.4}$$

The spectral pattern of the ith human body motion is correlated with the complex amplitude a_i and the pole pair (s_i, p_i). These poles, $\mathrm{s_i}$ and $\mathrm{p_i}$, produce the frequencies describing body limb joint movements in range (r_i) and Doppler (f_i), respectively. In the case of using CW data as described in [3.24], due to the lack of range information, the poles associated with the range (s_i) and subsequently the related frequencies (r_i) will be absent.

5.2 Data Processing

Here, we apply two effective techniques using SSM, the first is ST-SSM [3.15] and the second is 1-D block processing [5.2], to process the 2-D data formulated in (5.4) that was collected from a walking subject using the high-performance SFCW radar system. ST-SSM can be applied here as we have range information as well. The methods relying on the state-space procedure, forming the Hankel (forward-prediction) matrix is the key point here. Indeed, the Hankel matrix offers a way for computing the matrices defining the state-space

processing technique. For ST-SSM and 1-D block processing we form the Hankel matrices using the 2-D data in (5.4) in different ways. Therefore, we have developed ST-SSM and 1-D block processing methods to achieve the best results from the 2-D output data matrix collected by the SFCW radar.

5.2.1 Short-Time State Space Method (ST-SSM) for SFCW Signal

In ST-SSM we need to use a short-time sliding window function operating on a 1-D data string, $y(n)$. This data string or vector is formed from the range profile by focusing on one range bin, m_0, in the fast-time axis like the one in [3.15]. This range bin is obtained by selecting the effective range bins that correspond to the human subject and are accumulated along the fast-time (range axis). Thus, ST-SSM is applied to the data from a high range-resolution profile (HRRP). Here, using the 2-D data from the SFCW radar system and removing the static background of the backscattered signal, we first select the effective range bins, then accumulate them to make a 1-D data sequence vector, $y(n)$, by summing the information of the range profile along the fast time/range axis, and then we form the Hankel matrix using $y(n)$. The Hankel matrix derived from $y(n)$ [3.5], [3.15] is expressed as

$$H = \begin{bmatrix} y(1) & y(2) & \dots & y(L) \\ y(2) & y(3) & \dots & y(L+1) \\ \vdots & \vdots & \vdots & \vdots \\ y(N-L+1) & y(N-L+2) & \dots & y(N) \end{bmatrix} \tag{5.5}$$

where L is $[N/2]$ and brackets denote the smallest integer equal to or greater than $N/2$.

In fact, to use ST-SSM we need to form the range profile first, then ST-SSM is applied on the dimensionally reduced data from the range profile. Moreover, in ST-SSM the signals

with weak Doppler frequencies are treated as stationary signals (or signals with constant Doppler frequencies) in the short-time window. In this way, we change the 2-D data matrix of the range profile to a 1-D data matrix by summing up all the range bins along the range (fast-time) axis. This method is suitable for a system with huge data size and simple motions such as swinging hand or leg.

The results from ST-SSM on SFCW signal will be shown in the next chapter. However, since we collapsed the 2-D data matrix collected using SFCW radar system to a 1-D data vector by summing up the data of range profile along the range axis, we eliminated frequency information. Therefore, to have more accurate estimation, we needed to use the information in both time/frequency dimensions. In this way, 1-D block processing technique can be applied on both dimensions of the 2-D data matrix collected using SFCW radar system.

5.2.2 Enhanced 1-D Block Processing Technique on 2-D Data Matrix of SFCW Radar

After removing the static background, we implemented the SSM-based technique noted by the 1-D block, on a 2-D data set which is collected from the SFCW radar, where each row is like a CW data set. Hence, we should have M rows ($M = 50$ frequency steps here). The data matrix is therefore represented as (5.4).

Therefore, simple Hankel matrices are formed from each row of the 2-D data set given by (5.4). Here, we use vectors from the 2-D data set along the row direction, and each is using a set of time series.

In fact, the 1-D block processing is an alternative technique to the ST-SSM that is summarized above. It accounts for weak signals by exploiting coherency between

consecutive pulses, as well as accounting for noise to improve the SNR. It is carried out by computing an enhanced Hankel matrix and employing a superposition approach, from which strong and weak scattered signals are tracked separately in a recursive way.

However, the major difference between the 1-D block processing and ST-SSM is in forming the Hankel matrix. As a matter of fact, 1-D block processing forms an enhanced Hankel matrix with block matrix entries carried out on row/column of the data matrix. Therefore, in the 1-D block processing technique, the block matrix entries are Hankel matrices computed from each row or each column of the 2-D data matrix expressed in (5.4). Thus, the Hankel matrices of mth row and nth column are

$$H_m^{row} = \begin{bmatrix} y(m,1) & L & y(m,L) \\ y(m,2) & L & y(m,L+1) \\ M & L & M \\ y(m,N-L+1) & L & y(m,N) \end{bmatrix} \tag{5.6}$$

$$H_n^{col} = \begin{bmatrix} y(1,n) & L & y(J,n) \\ y(2,n) & L & y(J+1,n) \\ M & L & M \\ y(M-J+1,n) & L & y(M,n) \end{bmatrix} \tag{5.7}$$

where $L = [N/2]$, and $J = [M/2]$, where brackets denote the smallest integer equal to or greater than the value inside.

In fact, the 2-D data matrix can be modelled by forming a row-/column-enhanced Hankel matrix from one set of the complex matrices defined by (5.6) or (5.7). Here, we use vectors from the 2-D data set along the row direction, and each is using a set of time series. First, the row Hankel matrices are concatenated to form, for example (5.6) from which the row-

enhanced Hankel matrix is computed as defined in (5.8). The 1-D block processing state-space system associates the inputs to the output H_e^{row} to compute the state matrices.

$$H_m^{row} = \begin{bmatrix} y(m,1) & L & y(m,L) \\ y(m,2) & L & y(m,L+1) \\ M & L & M \\ y(m,N-L+1) & L & y(m,N) \end{bmatrix} \tag{5.8}$$

After forming simple Hankel matrices (H_m^{row}) (similar to the 1-D data set in [3.5]) from each row vector as described by (5.8), these row Hankel matrices are then concatenated to form (5.9). Finally, the matrix entries of (5.9) are casted into a meta-matrix that falls into the structure of a Hankel matrix that is denoted by enhanced Hankel matrix (H_e^{row}) (5.10) and is used to compute the state transition matrix from which human subject's motions are estimated. The 1-D block processing state-space system associates the inputs to the output H_e^{row} to compute the state matrices.

$$H^{row} = [(H_1^{row})^T \ (H_2^{row})^T \ \ldots \ (H_M^{row})^T]^T \tag{5.9}$$

$$H_e^{row} = \begin{bmatrix} H_1^{row} & H_2^{row} & \ldots & H_J^{row} \\ H_2^{row} & H_3^{row} & \ldots & H_{J+1}^{row} \\ \vdots & \vdots & \ldots & \vdots \\ H_{M-J+1}^{row} & H_{M-J+2}^{row} & \ldots & H_M^{row} \end{bmatrix}. \tag{5.10}$$

Given that the data sets are uncompressed, they can be exploited in both directions (frequency/range and time). In fact, use of the enhanced Hankel matrix with its full/complete structure of the 1-D block processing is novel and is more accurate approach. Let us emphasize here again that the 1-D block processing with a 2-D data accounts for weak signals by exploiting coherency between consecutive pulses, and mitigating the corrupting noise as well.

5.2.3 Signal Processing Technique for Motion Tracking

Once the enhanced Hankel matrix is computed, we estimate the block size (time window) and model order (number of scatterers) [3.5], and apply singular value decomposition (SVD) to define the enhanced Hankel matrix as a product of observability (Ω) and controllability (Γ) matrices that give rise to the state transition matrix A_r, the control matrix B_r, and the observation matrix C_r. Then an eigenvalue-eigenvector decomposition is applied to A_r to calculate Λ_r which is a diagonal matrix that gives the eigenvalues $\lambda_i(A_r)$ or state-space poles as its main diagonal entries; thus, the eigenvalues λ_i are used to calculate the μ-D frequencies corresponding to the body movements, f_i, and the corresponding damping factors, α_i. From mathematical point of view, we can formulate the whole process as follows:

Using SVD we decompose Hankel matrix as

$$H_e^{row} = \Omega\Gamma \tag{5.11}$$

On the other side, using the input-output relationship for the general autoregressive moving average (ARMA) model, the 1-D block processing state-space system relates the input to the output H_e^{row} so that

$$H_k^{row} = C_r A_r^{k-1} B_r, \quad k = 1, 2, \dots, M \tag{5.12}$$

where (A_r, B_r, C_r) are the state matrices and are related to the Ω and Γ matrices as

$$\Omega = [C_r \quad C_r A_r \quad \cdots \quad C_r A_r^{M-J}]^T \tag{5.13}$$

$$\Gamma = \begin{bmatrix} B_r & A_r B_r & \dots & A_r^{J-1} B_r \end{bmatrix} \tag{5.14}$$

Performing the SVD of the enhanced Hankel matrix and implementing a P rank reduction, the state-space matrices (A_r, B_r, C_r) are derived from Ω; therefore A_r is calculated as

$$A_r = \left(\Omega^*_{-rf}\Omega_{-rl}\right)^{-1}\Omega^*_{-rl}\Omega_{-rf} \tag{5.15}$$

where

$$\Omega_{-rf} = \Omega(N-L+2:(M-J+1)(N-L+1),:) \tag{5.16}$$

$$\Omega_{-rl} = \Omega(1:(M-J)(N-L+1),:) \tag{5.17}$$

Utilizing eigenvalue-eigenvector decomposition on A_r calculated in (5.15) results in the following derivation

$$A_r = M_r \Lambda_r M_r^{-1} \tag{5.18}$$

where Λ_r is a diagonal matrix with the eigenvalues $\lambda_i\{A_r\} = [\lambda_1, L, \lambda_P]$ (or the state-space poles) as the diagonal entries, M_r is the matrix of eigenvectors with column vectors $[\upsilon_1, L, \upsilon_P]$ associated with their corresponding eigenvalues. Thus, the eigenvalues λ_i produce the damping factors α_i and the frequencies f_i as

$$\alpha_i = \frac{log|\lambda_i|}{\Delta t}, \quad f_i = \frac{angle(\lambda_i)}{2\pi\Delta t}, \quad i = 1, \ldots, K, \ldots, P \tag{5.19}$$

In the case of complex motions such as walking, where more than one or two scatterers are involved, in addition to the above steps, we utilize a superposition approach, as captured in the flow diagram depicted in Figure 5.1, to extract both strong and weak joints' motion signals. In this way, we carry out several runs (iterations). Initially, the 1-D block extracts μ-D frequencies related to the body parts with stronger reflections (motions). Typically, it is not hard to model the data matrix or compute the fit for the kth block of pulses with the

ith set of eigenvalues $\lambda_i,\ i = 1, \dots, P$. Subsequently, a new data fit, $y'(m,n)$, is formed from the related poles (eigenvalues). Then, this new data set is subtracted from the original data set, $y(m,n)$, and a second iteration of the 1-D block algorithm is applied to the residual data with a new (typically larger) model order. The residuals allow estimation and tracking of weaker joints' motions. This process is repeated until the features of all desired body joints are extracted. Finally, we superpose all acceptable body parts' features into one plot. Capability of extracting low SNR signals covered by strong SNR signals is clearly one of the advantages of this method. The Flowchart of Figure 5.1 summarizes the 1-D block with 2-D data matrix.

5.2.4 Model Order Selection

This approach is very systematic until the choice of the two main parameters: model order and block size. We have developed a method for model order selection so it is deterministic, while the selection of the block size is heuristic but the size would be traded off with smoothness for optimum operation.

Model order estimation is always a challenge in signal processing, especially when the data are not particularly clean; however, there are approaches that might provide a good estimate of the model order. For example, the Akaike Information Criterion (AIC) [5.5] and the Minimum Descriptor Length (MDL) [5.6]. These approaches only sometimes work, depending on the SNR and data sampling rate.

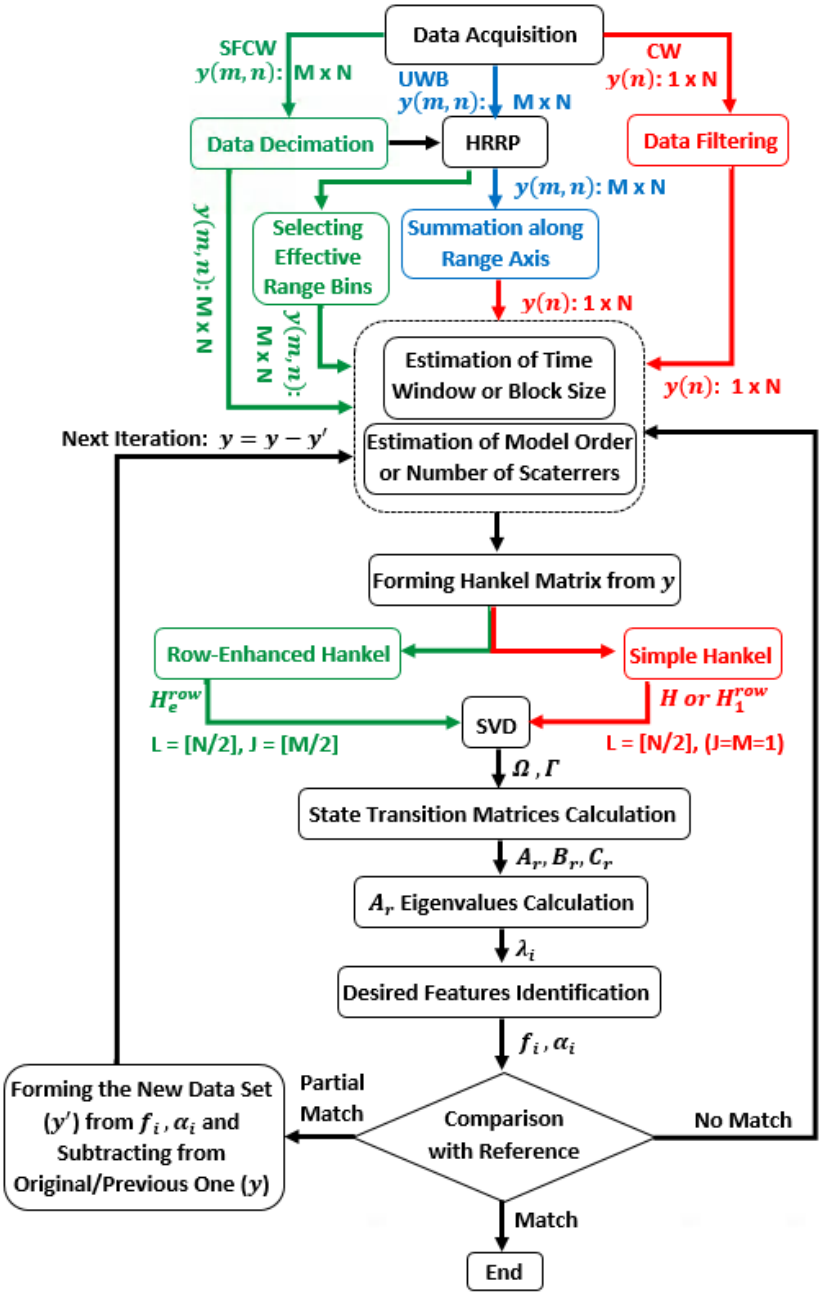

Figure 5.1 Gait analysis flowchart for different radars data, showing the difference between 1-D block processing technique using 2-D data matrix and using 1-D data vector. Green boxes and arrows represent 1-D block with 2-D data set, red ones show 1-D block with 1-D data set, and black ones indicate common steps; the initial steps taken by ST-SSM for UWB radar data are in blue.

In this work, we use Singular Value Decomposition (SVD) approach and relatively work quite often. However, this approach is very efficient in case of using 2-D data matrix and forming the enhanced Hankel matrix. Here is how we proceed:

1) In the 1-D block algorithm, we compute the enhanced Hankel matrix.

2) Then, we use SVD to compute the singular values from the enhanced Hankel matrix formed in the previous step and plot their amplitude to visualize these singular values.

3) Subsequently, we look for a breakpoint or a "knee" in the plot and identify its associated value on the x-axis to estimate the model order (Figure 5.2 shows an example of a singular value plot computed from enhanced Hankel matrices for all time windows and identify a general knee of the composite plots).

We use the superposition approach and successive subtraction, where we repeat these steps from the residual 2-D data until we retrieve velocities of all the parts, since large singular values are associated with strong radar returns, and the smaller ones are attributed to the weak signal components covered by noise. So, we use small model orders for strong signals, and large model orders for weak signals especially for noisy or for a scene with multipath effects based on multiple subtraction.

As mentioned above, the first step of model order selection with this approach is forming the Hankel matrix. However, in case of using SFCW radar to collect data, we have a 2-D data matrix which is used to form the enhanced Hankel matrix. Therefore, the break or “knee” in the singular value curves is more accurate and gives a better estimation of model order.

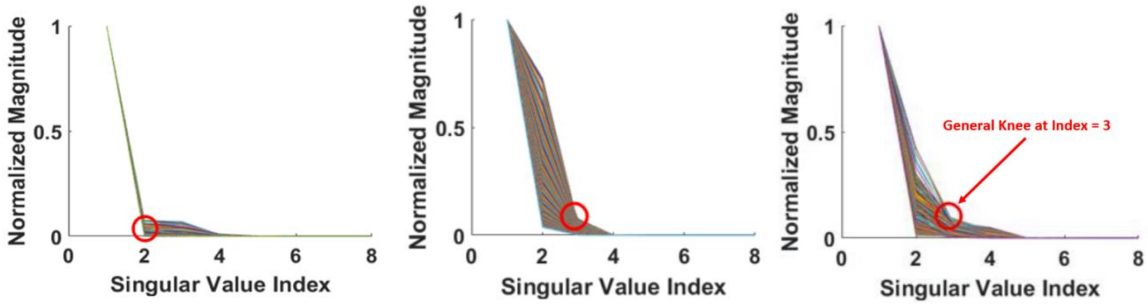

Figure 5.2 Singular value plots for estimating the order number. Use of the enhanced Hankel Matrix leads to more accurate order number estimation.

However, for block size estimation we choose it heuristically. Here we start from a block size of 10 as a rule of thumb that satisfies the constraints to generate an unambiguous linear image in accordance with the radar PRF, and increase the block size to find the optimum one that prevents excessive integration steps. The large block size provides enough samples to form an enhanced Hankel matrix that provides coherent gain to carry out the motion estimates and smoothness in the motion estimates as time evolves. However, larger block sizes result in higher computational cost and longer processing time as we have larger enhanced Hankel matrices to compute SVD from.

5.3 Conclusion

Our previously developed non-contact UWB radar detection techniques supported by ST-SSM signal processing were successful [3.15]; however, they were only suitable to track slowly moving body parts. The detection was hindered by the low PRF for the impulse radar and limitations of the ST-SSM. Here, SFCW radar with a high PRF is used to investigate the feasibility of tracking fast moving body parts, like toes, when their velocities are extracted by the enhanced 1-D block processing technique.

The 1-D block processing was applied to CW 1-D data string. In case of CW data, the implementation of ST-SSM is not very successful due to the lack of range information and heavy non-linearity. Moreover, because of the formulation of the 1-D block processing, the state transition matrix carried out from the observability matrix is computed not only from the row indices of the block Hankel matrix, but also from the data matrix and the free parameter L that is heuristically chosen $L = [N/2]$. Thus, the dynamic of the scatterers will be better captured, i.e., the non-linearity will be accounted for. Thus, this approach, in the

case of a single tone, will give rise to a slightly different state transition matrix for the 1-D block processing. It is expected that the eigenvalues of the state transition matrix will provide better estimates than those from the ST-SSM. However, the lack of information from range indexes of CW radar still results in less accuracy. The reason is that the row-enhanced Hankel matrix formed from a sequence of rows in the 2-D data matrix collected by SFCW radar provides a state identification matrix from which accurate poles can be extracted that are coherent as time evolves, whereas the Hankel matrix formed from a 1-D data vector collected by CW radar provides a state transition matrix that is computed from a single Hankel matrix exhibiting poles that provide coarse velocity estimates. Therefore, the poles from CW radar data fall short in coherency as time progresses.

As a result, we have expanded the 1-D block processing technique to be applied on a 2-D data matrix collected using SFCW radar system and expect more accurate results due to the forming of an enhanced Hankel matrix on the 2-D data. In the next chapter, Chapter Six, the results will be shown and compared to the results from applying 1-D block processing on CW radar data.

CHAPTER SIX
EXPANDED MOTION ANALYSIS UPON IMPLEMENTING ENHANCED 1-D BLOCK TO PROCESS 2-D DATA SETS

In this chapter, the experimental results obtained from the previously described implementation of the enhanced 1-D block processing technique on 2-D data set collected using the high-performance SFCW radar system with fast-switching frequency (i.e. fast-stepping rate) will be demonstrated and compared to our modeling results (as our reference or ground truth). To complete the picture, the results from applying ST-SSM on SFCW data and 1-D block processing technique on 1-D data vector collected using CW radar will be shown here as well to be able to compare various methods' accuracies and show the advantageous of applying SSM-based techniques on 2-D data set.

Additionally, human Boulic model has been used as a reference and all results will be compared with the results from the human Boulic model for the same experimental setup and conditions.

6.1 Human Walking (Boulic) Model

In this study, our focus is particularly on human walking. The combination of all motions and events happening during human normal walk is called gait cycle. In fact, human gait is time interval between the two consecutive repetitive events in human normal walking [5.1]. For example, consider the situation when in an event the right foot is on the ground and its velocity is negative (stance phase), while the left foot is not in contact with the ground and its velocity is positive (swing phase). Therefore, in a second event the right foot is not in contact with the ground and its velocity is positive, while the left foot is

touching the ground and its velocity is negative. Therefore, in a gait cycle, there is symmetry in the characteristics of the motions of the peer components such as feet and hands and the display of these characteristics is periodic due to the cyclic motions.

In order to model the human motion kinematics while walking and to have a complete human gait analysis, we utilize an analytical model extracted from empirical data, called the human Boulic model [5.1]. According to this model, human walking motion is modeled by cycles with constant translational velocity. There are two inputs to this model: the average velocity and the height of the human subject. From these two inputs, the human body phantom can be created using 16 joints between its 17 body parts, which are identified as the head and the lines between the joints, as depicted in Figure 6.1 (a) (The MATLAB codes implementing the human Boulic model were developed by Dr. Kilic's team in Catholic University of America (CUA)). Furthermore, the fundamental spatial and temporal motion characteristics (i.e. the length of the walking cycle, L_c, and the duration of the walking cycle, T_c) are also determined from these inputs. The time-dependent translation and rotation of each joint on a human body are then calculated using these two parameters, i.e. L_c and T_c. For example, Figure 6.1 (b) shows the radial speeds of the different human body parts for one walking cycle, T_c = 2.3 s, created by the Boulic model for a human subject with the height of 1.72 m and walking at 0.33 m/s speed. We can see that the lower parts of the legs such as the feet and ankles achieve a maximum μ-D frequency at around 30 Hz, while the torso and hands oscillate slightly around the velocity of the translational movement of the human. The motions of the left and right parts of the human body are observed to be cyclic [5.1].

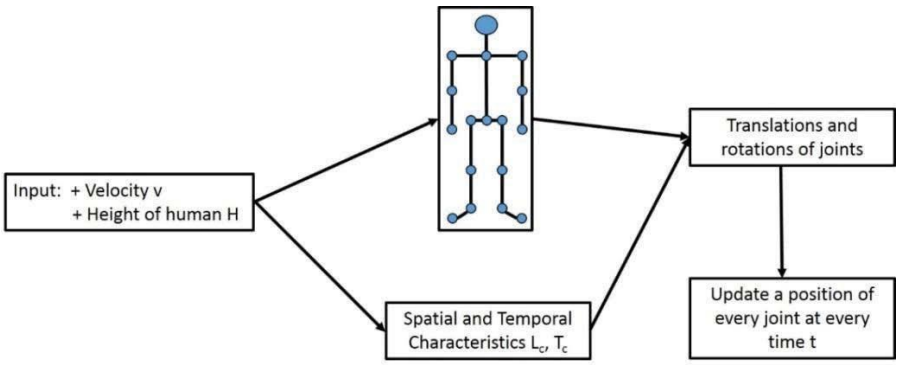

(a)

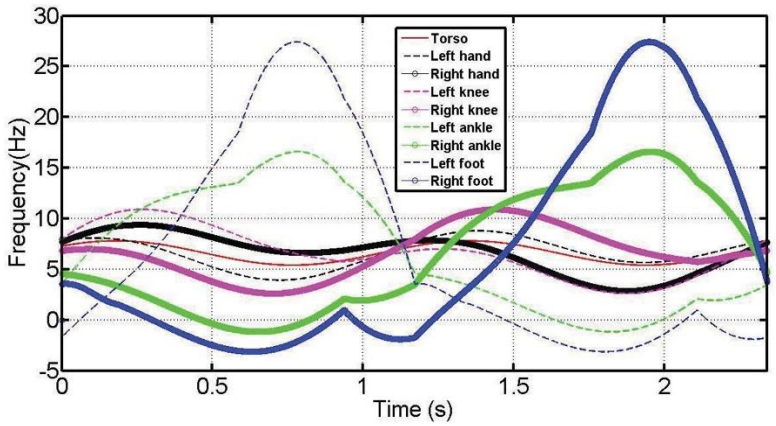

(b)

Figure 6.1 (a) Human motion model with 17 body parts. (b) μ-D frequencies of different body joints in one cycle [3.15].

However, in experimental scenarios, we know the height of human subject as a priori. But in order to have the other input of the model, i.e., velocity of human subject, we use a camera to record the walking or motion and then we calculate the average walking speed or velocity using the software "Tracker" [6.1]. Using this software, we can calculate the speed of any moving component of the human body separately, as well.

In this effort we did not use simulation and results using Electromagnetic (EM) tools for comparison, but used only the Boulic model as our ground truth. Previously, in [3.15] and [3.5], this model was utilized to simulate radar data by implementing EM analysis as well, where the method of moments (MoM) enhanced with a multi-level fast multi-pole algorithm (MLFMA), and using EM simulator tool FEKO. Results were compared to the Boulic model results. The results from the simulated data and Boulic model were in good agreement. Given that Boulic model data were very good and EM simulation takes lots of time in case of using SFCW signal with many frequency steps; then we used with high confidence here only the Boulic model as our ground truth.

Moreover, this walking model enables us to recognize the different body components with the same or similar frequency information. Different body parts (for example the right and left feet) may produce similar or exactly the same micro-Doppler (μ-D) frequencies. However, these μ-D frequencies happen at different time intervals. Therefore, we use time-frequency (time-velocity) representation to separate the left foot motion from the corresponding right foot. In fact, in a normal walking scenario, when the right foot is moving forward (with positive velocity or Doppler frequency), the left foot is lagging so they reach their peak values at different times as shown in the Boulic model of Figure 6.1

(b). The proposed processing scheme is different from STFT method that produces a mixed, while SSM methods can separate the spectrum of the different body components. In fact, state-space method or SSM-based techniques such as the 1-D block or ST-SSM predict the states of the system as time evolves and provide motions of walking human subjects and their dynamics as well. Therefore, using SSM-based methods, including 1-D block, we can track different moving body components (scatterers) separately as long as they happen at different times.

6.2 Experimental Results

6.2.1 ST-SSM vs. 1-D Block Processing

To compare the two state space methods in a simple motion scenario, we collected experimental data from a subject with only one hand swinging for one cycle (T_c) and conducted analyses using both ST-SSM [3.15] and 1-D block processing techniques using 2-D data sets [5.2] with the same model order and block size. Figure 6.2 shows the results for the wrist and elbow when a model order of 6 and a block size of 80 ms were used. To validate the results, the Boulic model for swinging only one hand with the same velocity has been utilized as well and the results are shown in Figure 6.2. It is clear that the ST-SSM correctly predicts the maximum velocity of the different motions of the wrist and elbow but the fine details of the motion are missing. Using the 1-D block method provides better classification of the motion besides accurate prediction of the maximum velocity.

In this case, the performance of both methods have been compared by calculating the error defined as the absolute value of the difference between the velocity and reference.

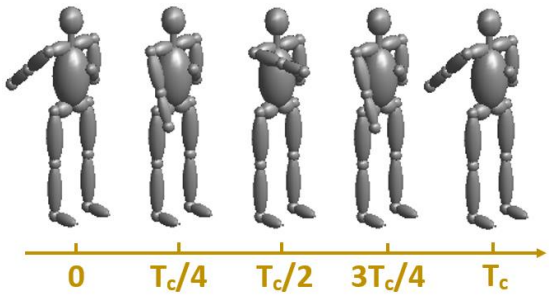

(a)

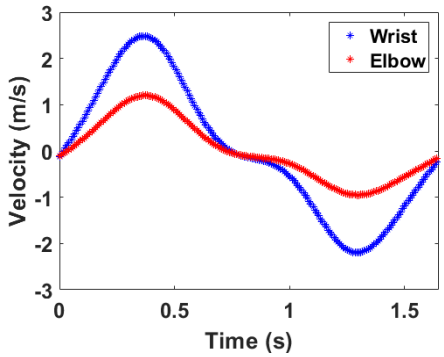

(b)

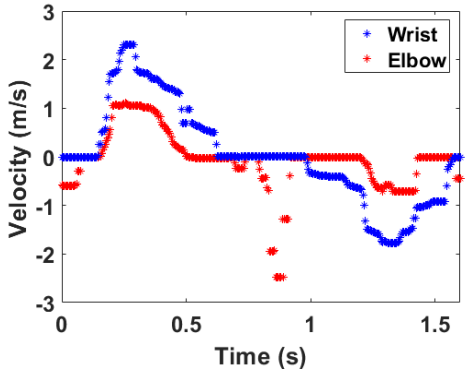

(c)

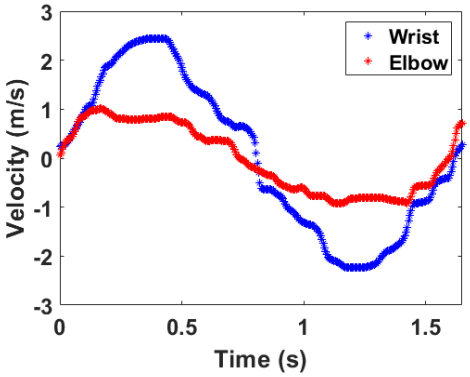

(d)

Figure 6.2 (a) Human motion model while the subject is swinging one hand only for one cycle (T_c); extracted velocities of the components of the swinging hand from (b) Boulic model, (c) ST-SSM, and (d) 1-D block processing.

Table 6.1 A Comparison of The Velocities of The Moving Components from Boulic Model and The ST-SSM and 1-D Block Methods, Applied to The Measured Data from The SFCW Radar for One Cycle of Hand Swing

Tracked Part	Time (s)	Velocity Boulic (m/s)	Velocity ST-SSM (m/s)	Velocity 1-D Block (m/s)
Wrist	0.25	1.97	2.30	2.09
	0.5	1.83	0.69	1.85
	0.75	-0.02	0.00	0.55
	1	-0.55	-0.34	-1.32
	1.25	-2.13	-1.54	-2.20
	1.5	-1.19	-0.93	-0.88
Sum of Errors			2.55	1.86
Elbow	0.25	0.92	1.09	0.81
	0.5	0.87	0.00	0.73
	0.75	-0.05	0.02	-0.03
	1	-0.28	0.00	-0.61
	1.25	-0.92	-0.51	-0.82
	1.5	-0.56	0.00	-0.56
Sum of Errors			2.36	0.69

As a matter of fact, the error defined as the absolute value of the difference between the value achieved from each method, and the velocity value obtained from the Boulic model as a reference (correct velocity) at a 0.25-s interval for a total period of 1.5 seconds. These error values are summarized in Table 6.1.

As can be seen from Figures 6.2 (b), (c), and (d) and Table 6.1, the results from the 1-D block processing outperforms the results obtained by ST-SSM as the sum-value of errors from the 1-D block processing technique is smaller than that from ST-SSM for both body parts. In general, for 1-D block processing the state transition matrix computed from the row/column enhanced Hankel matrix exhibits higher smoothing impact due to its large number of rows and columns entries; thus providing more accurate frequency estimates than those computed from the state transition matrix of ST-SSM that is carried out using a simple Hankel matrix. In fact, for ST-SSM, by summing up the data along the range axis, we collapse the phase information that may originate from different body parts with different behavior for a given pulse into one sample. However, in this motion scenario, the motion is swinging only one hand and is a very simple motion; meaning that in the same time intervals for one swinging hand, both wrist and elbow have the same behavior and cause the same impact on the phase information of the returned signal to the radar. For example, from starting point (time 0 s), both are still with the velocity of 0 m/s. Then in the forward moving cycle, the velocity of both wrist and elbow components increase gradually and reach their maximum velocities at the same time (around 0.4 s ($T_c/4$) and then start to decrease until reach the velocity of 0 m/s (at around 0.8 s ($T_c/2$). Then in the backward cycle (from $T_c/2$ to T_c), again both wrist and elbow have the same behavior at

the same times (and both with negative velocities). Therefore, by summing up all the range bins along the range axis, still we are able to retrieve the velocity of wrist and elbow using ST-SSM since they have the same effect on the phase of the radar signal.

By the way, although ST-SSM is able to retrieve the velocity of elbow in this simple motion, the results from 1-D block shows that 1-D block outperforms ST-SSM, due to the fact that 1-D block is using more information (all the range bins or fast-time information) to from the enhanced Hankel matrix. Consequently, the results from 1-D block include more details.

However, for more complex motions, such as swinging both hands in the opposite directions or stepping or walking, ST-SSM is not able to retrieve the velocity of body components with weaker scattered signals. In these cases, the behavior of the weaker scatterers such as elbow is overwhelmed by the stronger ones, since they have different impacts on the phase information with smaller amplitudes.

Therefore, in case of complex motions such as walking and consisting of several scatterer body joints with different behaviors at the same time intervals, ST-SSM is not suitable for extracting μ-D features of such different body parts with weaker return signals.

Now you talk about weak signals previously it was all signals but you got the elbow and wrist very confusing. Alternatively, the 1-D block processing technique considers all the data related to effective range bins (the range bins associated to the subject and his/her motions) of the moving subject and consequently includes the phase information of all moving body parts which can be separated using their frequencies. As a matter of fact, the

1-D block processing is applied to the original data set without any dimensionality reduction (without collapsing range-bin information).

Comparing the experimental results from the two methods with the Boulic model shows that both methods have the capability of extracting motion features since still we are using the time axis information and the summation of range bins (and of course signal intensity). However, the 1-D block processing results exhibit more accurate motion velocities for moving components of the body due to exploitations of the coherence (what do you mean by coherence here?) (between the elements of enhanced Hankel matrix, reflecting the correlation between the parameters or motion features) and consequently smoothness elaborate here of the row-enhanced data matrix that gives rise to a smoother transition. Because of the inherent structure of 1-D block processing, the state transition matrix carried out from the observability matrix can better capture dynamics and nonlinearities of the weak scatterers compared to the state transition matrix computed from ST-SSM [3.15]. This inherent structure allows the 1-D block processing method to successfully extract the motion features using not only SFCW radar data, but also CW data as well.

However, the best performance has been achieved when applying the 1-D block processing on UWB 2-D data matrix. This data as explained before is created here using SFCW radar.

In fact, ST-SSM and 1-D block processing are independent methods and their difference is in forming the Hankel matrices. In ST-SSM the Hankel matrix is a simple one. It is formed from a collapsed range profile by summing up the all the range bins along the range axis. While 1-D block is performed on the original data set collected by the radar. In case

of SFCW radar, 1-D block forms the “enhanced” Hankel matrix that is carried from set of rows/columns of the 2-D data set.

Given that the two techniques, ST-SSM and 1-D block processing, were implemented on the same 2-D dataset collected using the high-performance SFCW radar system from a moving human subject, we were able to compare and evaluate the performance of these two SSM-based methods in a fair way. Hence, we have concluded that the 1-D block processing outperforms the ST-SSM method. Therefore, from now on we will apply the 1-D block processing on the data collected from a single-subject and also from multi-subject scenarios considering more complex motions in the following sections.

6.2.2 Single-Subject Gait Analysis

In the following, we present gait analysis of two motion scenarios for a single subject using the 1-D block processing technique with 2-D data collected by the SFCW radar. In these investigated two cases, after removing the static background, we form the enhanced Hankel matrix. Typically, in case of a single person, we apply the 1-D block on the original 2-D data set collected by the SFCW radar. But, if the SNR is low, we first form a range profile on the original data set by applying inverse Fourier transform (iFFT) along the frequency axis, choosing only the effective range bins related to the subject motions from the range profile. This helps to de-noise the data set due to the subtraction of unrelated range bins and static background. This step is followed by applying the 1-D block on each row (range bins) of this new 2-D data set and form the enhanced Hankel matrix using these effective range bins.

In the first case, data was collected from a single moving subject with a height of 1.60 m, where the 1-D block was implemented and compared to the Boulic model results. The subject walks for one cycle (T_c) at a speed of approximately 0.5 ms^{-1}, while the subject's hands are folded and immobile as indicated in Figure 6.3. The signal processing was run for three iterations, where the second and third iterations were run on the residual signals. In the first iteration, a model order of 4 was estimated based on the computed knee [3.5] and the velocity of the torso was extracted first (being strong signal), while during the second and third iterations, a model order of 12 and 17 were computed, respectively, for the residual signals, to obtain the velocities of the remaining moving components with weaker reflections. These large model orders are due to multipath effect and weaker signals corrupted by noise. Meanwhile, the block size selection of the above three iterations is heuristic; but was optimally chosen to be 90 ms. Results in this scenario are in very good agreement with the Boulic model as will be shown in Figures 6.3 (b) and (c).

In the second scenario, a similar analysis was applied to a moving subject with a height of 1.60 m, while walking at a speed of about 1 ms^{-1} with both hands swinging (normal walk) to investigate the extraction of relatively faster motion scenarios. Figure 6.4 shows the human motion model and results from both the Boulic model and the 1-D block processing using the enhanced Hankel representation. In this scenario, we selected 3 iterations with estimated model orders of 3, 8, and 12, respectively, with an optimum block size of 75 ms for all iterations. Again, very good agreement was demonstrated for these relatively fast-moving joints.

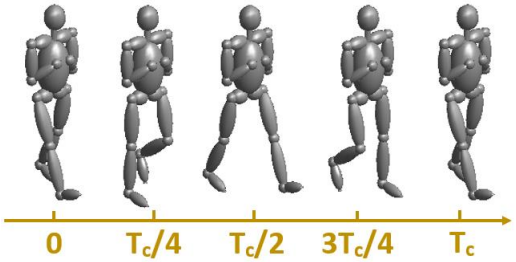

(a)

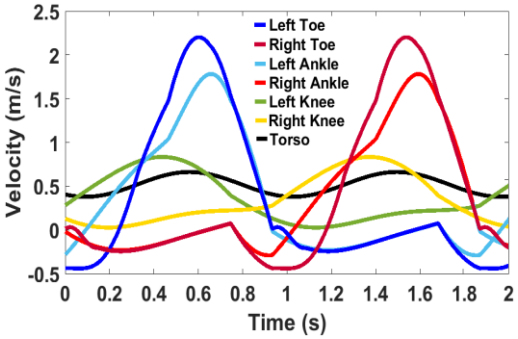

(b)

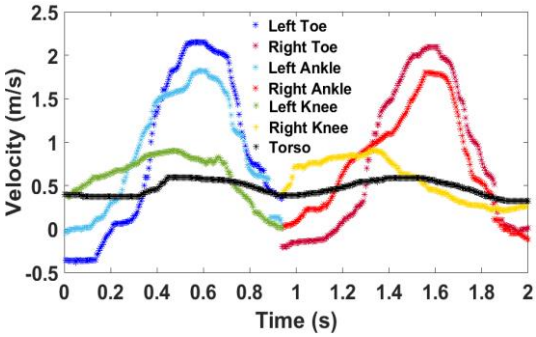

(c)

Figure 6.3 (a) Human motion model, while walking for one cycle (T_c) without any hand motion; extracted velocities of the moving components from (b) Boulic model, and (c) 1-D Block on 2-D SFCW data. (The average velocity of moving: 0.5 ms^{-1}.) It is imperative to recognize here that right and left joints could have the same poles obtained from the enhanced Hankel matrix, but their motions could be discernable in the time-frequency representation as they occur at different time ranges as shown above.

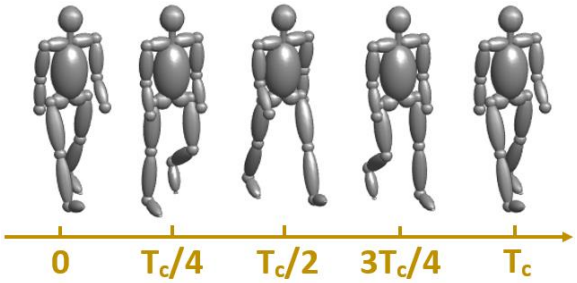

(a)

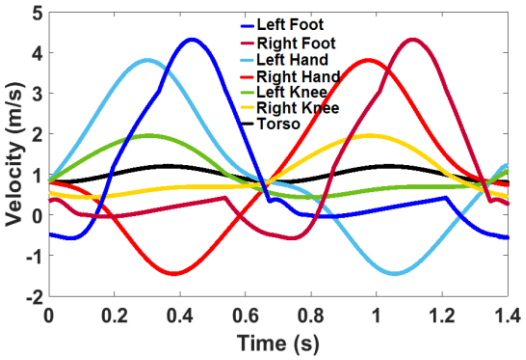

(b)

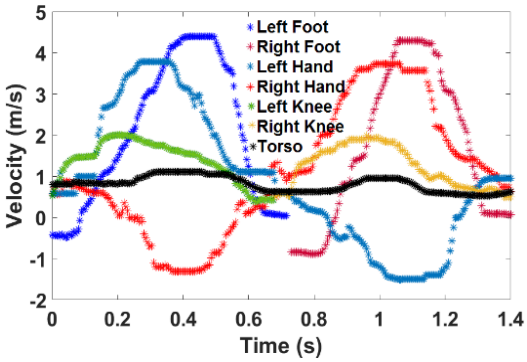

(c)

Figure 6.4 (a) Human motion model, while walking for one cycle (T_c) with both hands swinging (normal walk); extracted velocities of the moving components from (b) Boulic model, and (c) 1-D Block on 2-D SFCW data. (The average velocity of moving: 1 ms^{-1}.)

6.2.3 Multi-Subject Gait Analysis

Here, we utilize the available bandwidth and range resolution capabilities of the SFCW system to investigate four scenarios for multi-subject experimental setups, where the data for a specific time is collected and the static background is removed. It is imperative to mention here that in a physical therapy application for example, we can use a real deep depth camera to measure the range and remotely identify the number of subjects in a scene. But, if we say we are in the dark, then we can benefit from utilizing other capabilities of our developed radar system to identify human subjects in this situation. We can use this radar system for non-contact human vital sign detection including their respiratory rate and heart rate. Even when a human subject is static, we can still detect him/her as a human subject by detecting the respiratory rate and chest displacement very clearly, using phase-based method and with that comes his/her range information. It is worth emphasizing that the human subjects, even though they are stand still, they will not be subtracted as static background in the scene as they are still breathing. So, we first subtract the static background and then apply iFFT along the frequency axis to form the range profile. Then, we separate the subjects by choosing the effective range bins. Then, we implement the 1-D block processing by forming the enhanced Hankel matrix from this new 2-D data set for each subject separately.

Since the subjects move in front of the radar, we only use down-range info to separate the motion of the different subjects. The down-range resolution of the developed SFCW radar is 15 cm (5.9 inches) according to the following formula:

$$R_{res} = \frac{c}{2 \times B} \tag{6.1}$$

where c indicates the speed of light and B is the effective bandwidth (here 1 GHz).

In order to use cross range information to better discern the motions of the different subjects present in the scene, we need to use an array of antennas to have reasonable azimuth angle resolution. However, in this work, it was found out that a lateral (azimuth) separation distance of about 25 cm between the subjects was adequate to clearly see two subjects placed symmetrically with respect to the antenna's broadside direction.

In any case, to accurately estimate the limb joint motions, we needed high PRF, and as explained before a PRF of 200 Hz is adequate here to capture the fastest motion of the body parts of a walking subject. You need bring the discussion about PRF and center frequency from the reviewers' comments

In the first scenario setup, shown in Figure 6.5 (a), the two subjects stand in front of the radar, one at a distance of 1.7 m to the radar and the second at 2.1 m. The subjects are equally off-center from the radar boresight direction view, and are at a distance of 0.6 m from each other as shown in Figure 6.5 (a). Both subjects stand and swing only their right hands with a maximum speed of around 3 ms^{-1}. We segragate the two subjects'motions using their effective range bins from the range profile as seen in Figure 6.5 (b), where we identify the effective range bins associated with each subject's motion. Then, the 1-D block is implemented on the relevant range bins for each subject (new 2-D data sets). This approach helps in reducing the background noise. Figure 6.5 (c) presents the extracted velocity of the hand for each subject.

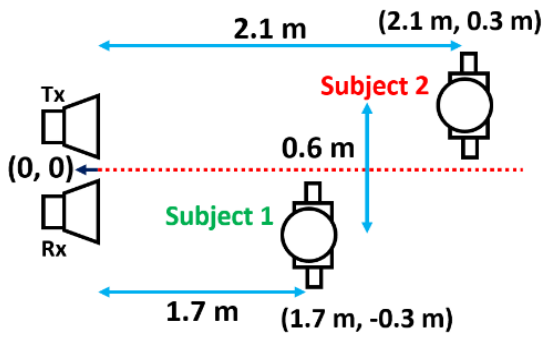

(a)

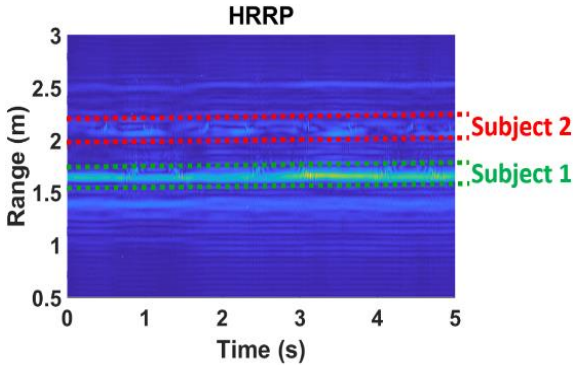

(b)

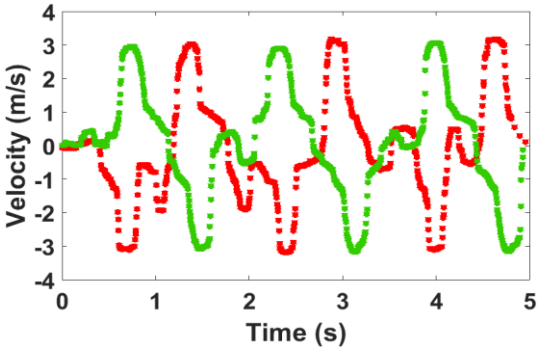

(c)

Figure 6.5 (a) Experimental setup for multi-subject motion analysis using SFCW radar system for swinging only one hand (top view); (b) Extracted high range-resolution profile identifying the two subjects and their motion ranges; and (c) Extracted hand motions from 1-D block processing. It is essential to recognize here that if we combine the motions of the two subjects using enhanced Hankel matrix, then we will have quite similar frequencies on top of each other, in addition, that strong signals (typically related to the close-by subjects) will bury the signals from the further away subjects with lower SNRs. This method efficiently separates these subjects by their relevant range bins.

In the second scenario, we investigate the case of two subjects walking in front of the radar. Similarly, we form a range profile from the data first. Then, we select the effective range bins related to each subject from the range profile. Now we have two sets of 2-D data, each associated with one of the subjects that is ready to be processed using the 1-D block processing technique, in which enhanced Hankel matrices are formed from each 2-D data set. Figure 6.6 (a) shows the setup scenario, where the first subject with a height of 1.75 m walks from a distance of 3.1 m to 2 m towards the radar at a speed of 0.55 ms^{-1}, while the second subject with a height of 1.60 m walks from a distance of 4.4 m to 3.4 m towards the radar at a speed of around 0.50 ms^{-1}. Figure 6.6 (b) indicates the range profile showing the location and distance of the subjects to the radar for the corresponding time, and Figures 6.6 (d) and (f) show the results of applying 1-D block method to extract motions from each subject as time evolves (within two seconds). The results were validated using the Boulic model for the same setup (same height and speed of the subject) as well as the same relative time for each subject separately, and these results are shown in Figures 6.6 (c) and (e).

Preliminary results indicate that we are able to track different body components in multi-subject scenarios. It can be seen from the results too, that certain degradation exists in extracting the velocity of the two subjects' body parts, which is related to multipath effects and mutual coupling between the two subjects as the two subjects get closer to each other in the scene. Comparing the first experimental results and the second one shows that our results for standstill subjects with one hand movement were in good agreement with the Boulic model, but for a walking subject, it was kind of a blur which is a well-known problem because of both multipath and the relative motion between the radar and target.

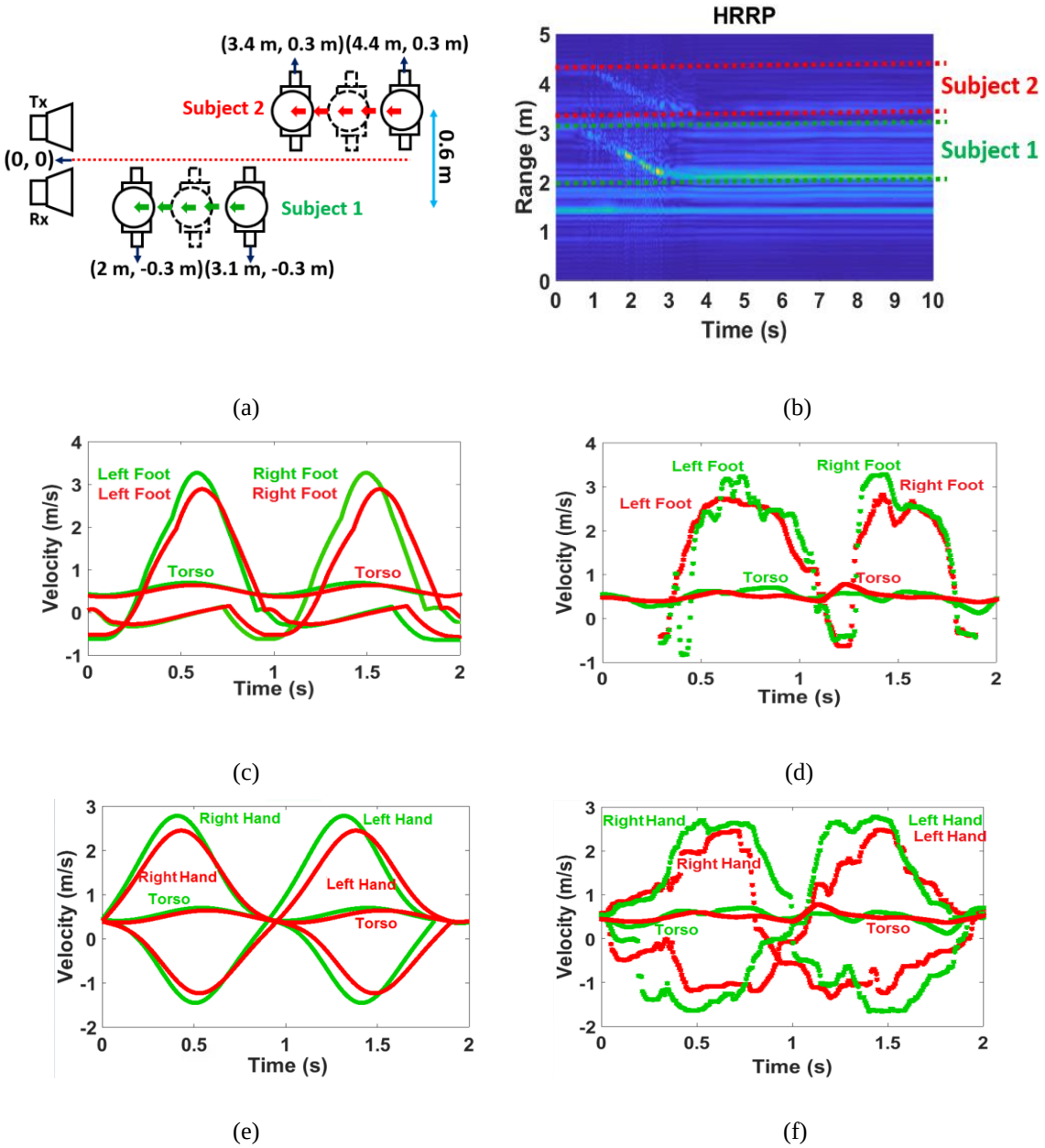

Figure 6.6 (a) Experimental setup for multi-subject gait analysis using SFCW radar system for normal walk (top view); (b) Extracted high range-resolution profile recognizing the two subjects and their motion ranges; (c) Extracted velocities from the feet of subject 1 (in green) and subject 2 (in red) using the Boulic model, and from (d) 1-D block processing; (e) Extracted velocities of the hands of subject 1 (in green) and subject 2 (in red) using the Boulic model, and from (f) 1-D block processing.

However, to improve the quality of the ISAR products, motion compensation is recommended. Reference [6.2], for example, used range-bin alignment for translational motion compensation to provide more robust images.

In the third scenario, we consider an experimental setup to address multipath/mutual coupling effects on human subjects tracking. In this scenario, one subject starts to walk towards the radar antenna, while the other subject is standstill in the scene as depicted in Figure 6.7 (a). Although the other subject standstill, the results have been degraded slightly due to the multipath/mutual coupling effects caused by the presence of a nearby human subject. The reason is that a static human subject still has tiny motions due to his/her respiration, heart beat, and body random motions that can increase the impact of multipath/mutual coupling effects in the scene. However, the results are better than the ones in Figure 6.6, since in that scenario both subjects are walking.

And in the last scenario, we show the capability of the 1-D block to retrieve the velocity curves from different subjects in the scene, when they are close in range or their ranges overlap. To show this fact, we have designed an experiment where the two subjects stand in front of the radar system and both are swinging only their right hands. The two subjects have the same radial distance to the radar antenna as shown in Figure 6.8 (a). 1-D block can retrieve the velocities of the swinging hands separately (Figure 6.8 (c)). Using the 1-D block processing technique enables separating the velocity of the moving components in a scene and it does not depend on the range information. It means even if the two subjects are in the same radial range, the 1-D block is still able to retrieve the velocities of the moving components from each subject separately, but we will not be able to relate that to

a specific subject. So, having two subjects at the same range, even though they are close to each other when using one antenna, we would still be able to detect the various velocities of the two subjects. However, we will not be able to relate these velocities to a specific subject. If the two subjects are at different ranges, then we can use range information to discern the two, as we did in the first and second experiments, but if they are at the same range, then we need to use an array of antennas to create a SAR image (2-D image of the scene) and identify subjects along the cross range, hence we can discern between the two subjects/movements using cross range information. However, handling the detection of two subjects when they are very close to each other makes distinguishing a subject's unique movements very challenging, especially when the subjects are moving. As mentioned before, motion compensation is recommended here; in [6.2], for example, a range-bin alignment is used for translational motion compensation, that provides more robust analysis.

To summarize, having two subjects at the same range, even they are close to each other when using one antenna, still allow us to detect the various velocities of the two subjects. However, we will not be able to relate these velocities to a specific subject. If the two subjects are at different ranges, then we can use range information to discriminate between the two, but if they have the same range then we need to use an array of antennas to identify subjects along the cross range, to discriminate between the two subjects using cross-range information.

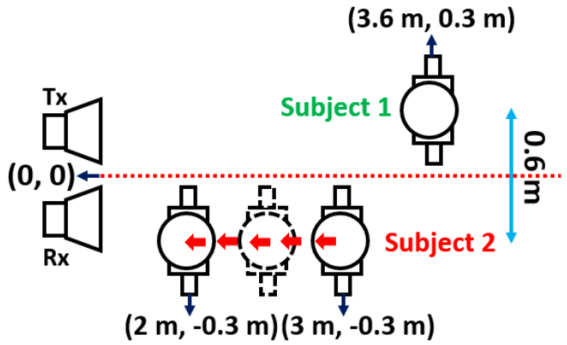

(a)

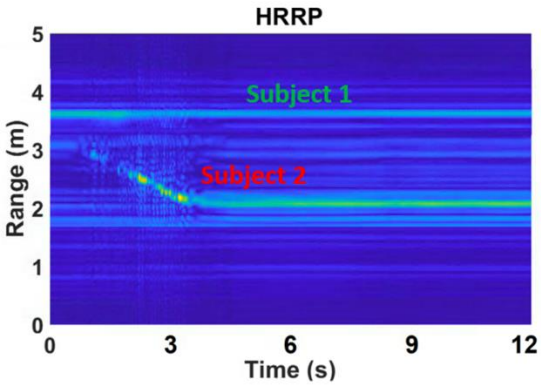

(b)

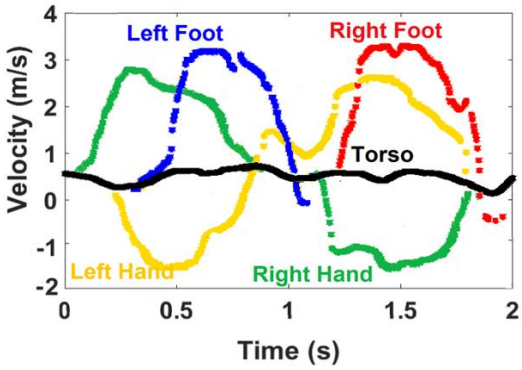

(c)

Figure 6.7 (a) Experimental setup for multi-subject gait analysis using SFCW radar system for normal walk, when one subject is still and static and the second one walks (top view); (b) Extracted high range-resolution profile recognizing both subjects and their motion ranges; (c) Extracted velocities from subject 2 using 1-D block processing.

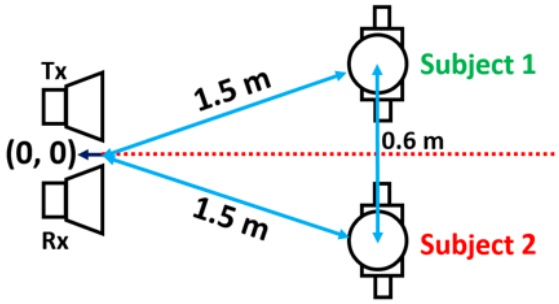

(a)

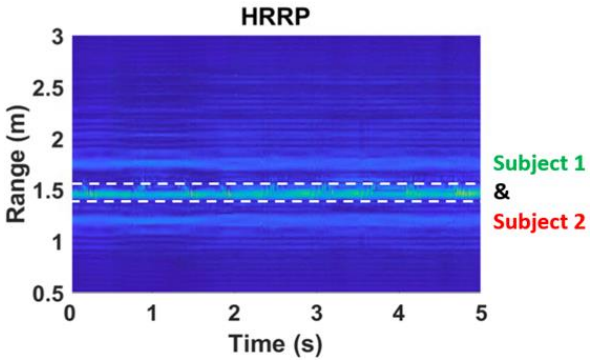

(b)

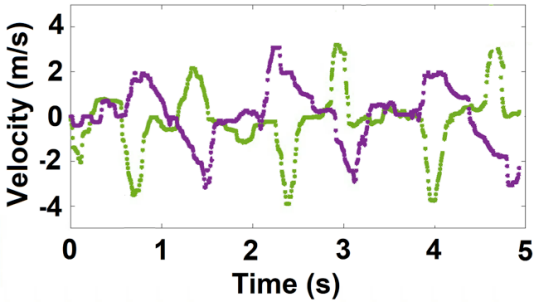

(c)

Figure 6.8 (a) Experimental setup for multi-subject motion analysis using SFCW radar system for the subjects at the same range and swinging only their right hands (top view); (b) Extracted high range-resolution profile showing the two subjects and their motion ranges; and (c) Extracted hand motions from 1-D block processing.

6.3 Comparison and Discussion of Results

Motion trajectories can be extracted by applying demodulation of the radar signal. In fact, phase information which is linearly proportional to target's motion can be achieved by applying arctangent demodulation to the radar signal. But when a subject is moving or walking in front of the radar, the motion is composed of two parts: one part is the macro motion due to the whole-body movements, and the other part is the micro motion due to the swing of the different body joints.

The motion trajectories display macro motions from the strongest moving components, which are very useful for motion sensing applications as they can give general characterization of the body posture. In Figure 6.9 we have demonstrated the motion trajectories of a moving human subject for different motion scenarios (swinging only one hand, and walking) using demodulation of the radar signal.

As it can be seen from the above figures, these motion trajectories display the general motion from the strongest moving components. Meanwhile, 1-D block processing technique (micro-Doppler processing), is used to extract the instantaneous velocities that are associated with the weak joint motions and can track each joint's motion separately. Thus, this μ-D information can be used for full motion analysis. As an example, there are clinical studies on the elderly which link changes in various gait characteristics such as poor balance, slower pace, shorter steps, lower walking velocity and higher cadence to gait deficiency. However, having both macro information and micro-Doppler features, would enable us to develop 3-D patterns of human motion which are very useful.

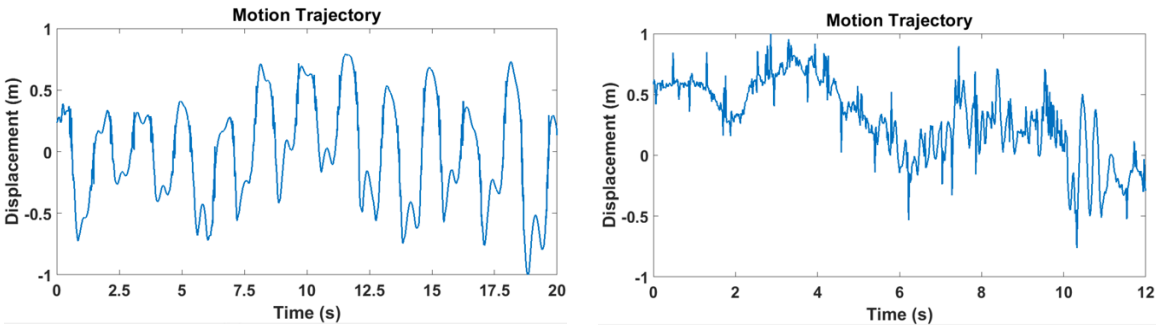

(a) (b)

Figure 6.9 Human motion trajectories for (a) swinging only one hand, and (b) walking.

The motion trajectories include both macro and micro motions. However, since the macro motions overwhelm the micro motions because they are much stronger and cause stronger effect, it is very hard to see micro motions from motion trajectories. In other words, micro motions exist in motion trajectories but they are hidden and covered by stronger signals associated with macro motions. As a matter of fact, motion trajectory is a time-amplitude plot., and we would need a way to extract these tiny motions and separate them from the body movement signals with larger amplitudes. That is the reason why we have developed 1-D block processing in two dimensions to be able to discern these tiny signals caused by swinging of body joints for example. In this way, we are looking for velocity curves (time-velocity plot) for each body joint, that enables us to classify the micro motions from macro motions by giving us more detailed information on the motion of different body components. 1-D block is capable of extracting very weak signals through multiple subtraction (many iterations) as explained in Chapter Five.

In fact, the novel approach of this work is the implementation of 1-D block processing on the 2-D data set by forming an enhanced Hankel matrix from this 2-D data set collected by an SFCW radar. In SSM-based signal processing methods, generally, the most important part is forming the Hankel matrices from the data to exploit the correlation between samples from rows/columns, estimate the model order or dimension of the system and compute the state matrices.

Previously, in [3.15], ST-SSM was implemented on the data collected by a UWB radar system. Although the UWB radar system gave us a 2-D data set, i.e., range profile (range-time intensity (RTI)), we collapsed this data set into a 1-D data set vector, due to the large

number of range bins that UWB radar gives; and that had resulted in a very expensive computational process. In this case, we summed up the range bins along the range axis and then formed the Hankel matrix from this new 1-D data set. Hence, SSM was carried out in the time direction because the data was compressed and the time series can be represented by a sum of sinusoids.

Alternatively, in [3.5], the 1-D block was implemented on the original data set collected by the CW radar, so it was a 1-D data set by itself as it came from a single-tone (single-frequency) radar. From this point of view, the Hankel matrices formed by both [3.15] and [3.5] are simple Hankel matrices formed from 1-D data set vectors. Therefore, in both cases, [3.5], [3.15], the 1-D data set vectors can be written as

$$Y = [y(1)\, y(2) \ldots y(N)] \tag{6.2}$$

and the forward Hankel matrix is formed using this 1-D data set vector according to

$$H = \begin{bmatrix} y(1) & y(2) & \ldots & y(L) \\ y(2) & y(3) & \ldots & y(L+1) \\ \vdots & \vdots & \vdots & \vdots \\ y(N-L+1) & y(N-L+2) & \ldots & y(N) \end{bmatrix} \tag{6.3}$$

The idea of this work is implementing SSM from a 2-D data set. To do that, we developed a SFCW radar, explained in Chapter Four, that could provide a 2-D data set, from which each row is like a CW data set and we have 50 rows (frequency steps) in our set-up that may be represented as (6.4).

$$Y = \begin{bmatrix} y(1,1) & \cdots & y(1,N) \\ y(2,1) & \cdots & y(2,N) \\ \vdots & \cdots & \vdots \\ y(M-1,1) & \cdots & y(M-1,N) \\ y(M,1) & \cdots & y(M,N) \end{bmatrix} \tag{6.4}$$

Therefore, a Hankel matrix is formed from each row or column of the 2-D data set given by (6.4).

In this work, the 1-D block consists of using a set of time series, i.e., vectors from the 2-D data set along the row direction. Next, a Hankel matrix (H_m^{row}) similar to the 1-D data set in (6.4) is formed from each row vector as described by (6.5) and the set of matrices are later concatenated into a block row matrix (H^{row}) as defined in (6.6). Finally, the matrix entries of (6.6) are casted into a meta-matrix that falls into the structure of a Hankel matrix that we called enhanced Hankel matrix (H_e^{row}) (6.7) that is used to compute the state transition matrix from which human subject's motions are estimated.

$$H_m^{row} = \begin{bmatrix} y(m,1) & L & y(m,L) \\ y(m,2) & L & y(m,L+1) \\ M & L & M \\ y(m,N-L+1) & L & y(m,N) \end{bmatrix} \tag{6.5}$$

$$H^{row} = [(H_1^{row})^T \ (H_2^{row})^T \ \ldots \ (H_M^{row})^T]^T \tag{6.6}$$

$$H_e^{row} = \begin{bmatrix} H_1^{row} & H_2^{row} & \cdots & H_J^{row} \\ H_2^{row} & H_3^{row} & \cdots & H_{J+1}^{row} \\ \vdots & \vdots & \cdots & \vdots \\ H_{M-J+1}^{row} & H_{M-J+2}^{row} & \cdots & H_M^{row} \end{bmatrix} \tag{6.7}$$

So, in this work the data sets are uncompressed and exploited in both directions (frequency/range and time (or fast time and slow time)) via the enhanced Hankel matrix to estimate the motions from a human subject. Because of the smoothness and coherency of the enhanced Hankel matrix, a more accurate model order leading to better motion estimates can be obtained from the 2-D data set exploited here than the 1-D data set presented in [3.5] and [3.15].

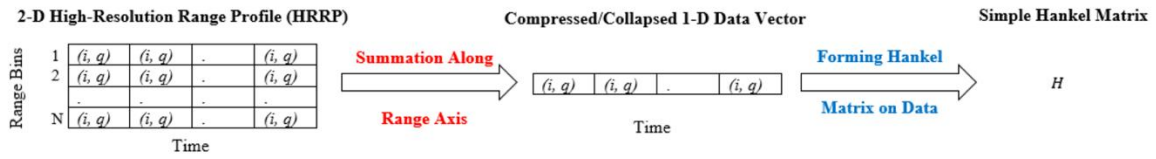

(a)

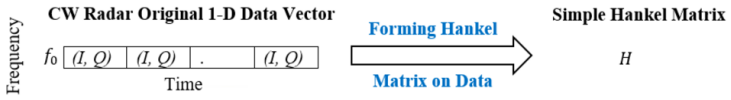

(b)

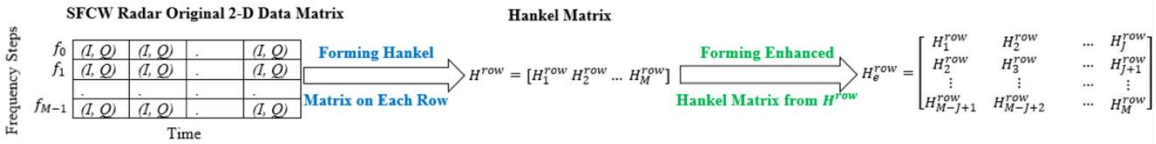

(c)

Figure 6.10 Summary of the steps taken by (a) ST-SSM, (b) 1-D block processing on the CW 1-D data vector, and (c) 1-D block processing on the 2-D data matrix collected from SFCW radar system ((i,q) → in time domain, and (I,Q) → in frequency domain).

In fact, use of the enhanced Hankel matrix with its full/complete structure of the 1-D block processing is novel and a more accurate approach.

Figure 6.10 summarizes ST-SSM, 1-D block on 1-D data set from CW radar, and 1-D block on the 2-D data set of SFCW radar. In this dissertation, we tackle the 2-D data set with an enhanced Hankel matrix instead of a simple Hankel matrix tailored for a 1-D data vector.

6.3.1 Combination of ST-SSM and 1-D Block Processing

As mentioned, ST-SSM needs the range profile inf, which is also a 2-D data matrix, and is used to form the simple Hankel matrix upon summing of the range bins, which is a 1-D data vector. While, the 1-D block is applied on the 2-D data obtained from the decimated data radar returns and the formed enhanced Hankel matrix. As a matter of fact, the 1-D block can be implemented on the range profile too. In this way, we form the range profile using the decimated 2-D raw data collected using SFCW radar by implementing inverse Fourier transform (iFFT). In the range profile, we subtracte the static background first, then we choose the effective range bins associated with the moving subject and generate a new 2-D data set with reduced dimensions. In this way, the combination of the two steps, the results of the enhanced Hankel matrix are more meaningful and slightly more accurate, again due to the subtraction of the noise (unrelated range bins and static background). It is obvious that in case of selecting large iFFT numbers, the computational cost of the processing would be expensive due to the huge row-enhanced Hankel matrix formed using high-resolution range profile (HRRP). Moreover, adding more steps would increase the total processing time. Figure 6.11 summarizes the combination of the two methods.

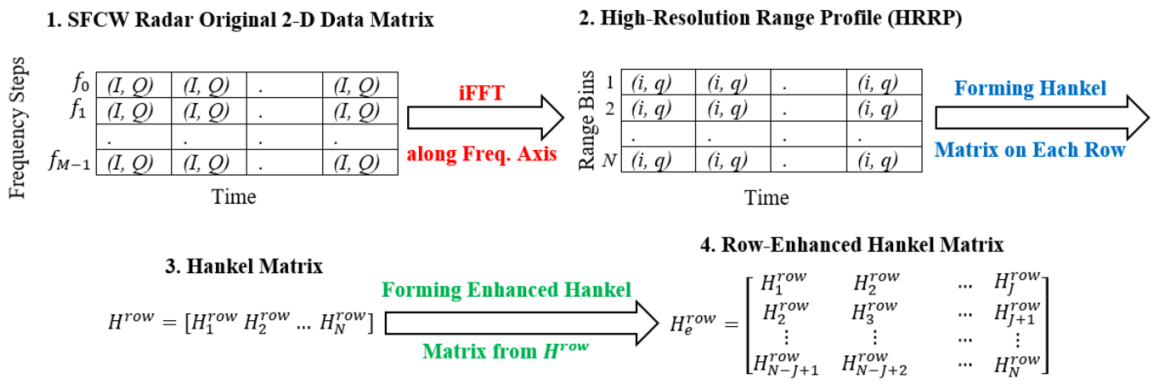

Figure 6.11 Summary of the four steps taken to extract the row-enhanced Hankel matrix where in step 2 only the effective range bins are used and static background is subtracted).

The beauty of implementing the proposed 1-D block method on 2-D data set is that it can be carried out on any 2-D datasets including those from SFCW radar that can be range profile, phase variation, STFT spectrogram, etc. Performance analyses of SSM and its comparison to Matrix Pencil were presented in the references [6.3-6.5]. Because the 1-D block processing technique outperforms ST-SSM that provides similar performance to Matrix Pencil; therefore, one can conclude that 1-D block processing outperforms also the Matrix Pencil approach. However, because the state matrices for the 1-D block processing are computed from an enhanced Hankel matrix obviously the computational cost is higher than ST-SSM, ESPRIT, MUSIC, etc.

6.3.2 Comparison of Results

To compare the performance of the SFCW and CW radars, we used the 1-D block processing technique. The limb joints' velocities were extracted from the 2-D data collected by the SFCW radar (shown in Figure 6.4 (c)) and the enhanced 1-D block representation was used. While implementing the conventional 1-D block processing on 1-D data vector collected by the CW radar, in a normal walking scenario is (shown in Figure 6.12 (b)) [3.5]. Then, their extracted velocities were compared with the relevant Boulic model results, and the deviation error values are listed in Table 6.2.

The comparison Table demonstrates that SFCW radar with 2-D data provides more detailed results than those of the CW radar with 1-D data especially at the points around the velocity peaks. Applying 1-D block on CW data, shows that the results of the velocity curves are kind of flat around the peaks and valleys.

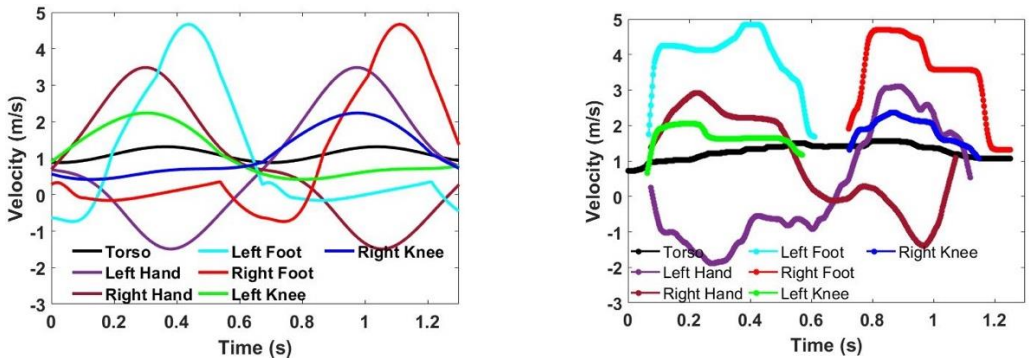

(a) (b)

Figure 6.12 Extracted velocities of the moving components for one cycle of a normal walk motion using (a) Boulic model, and (b) 1-D Block with 1-D CW data (The average velocity of moving: 1.1 ms^{-1}) [3.5].

Table 6.2 A Velocity Error Comparison for The Moving Components from The Boulic Model and 1-D Block Processing Applied to The Measured Data from The SFCW Radar in This Work and CW Radar in [3.5] for One Cycle of Walking

Time (s)	**Foots Error SFCW**	**Foots Error CW in [3.5]**	**Left Hand Error SFCW**	**Left Hand Error CW in [3.5]**	**Right Hand Error SFCW**	**Right Hand Error CW in [3.5]**
0.2	0.19	2.90	0.21	0.07	0.04	1.22
0.4	0.23	0.37	0.01	0.66	0.13	0.71
0.6	0.63	0.25	0.10	0.63	0.01	0.96
0.8	0.62	5.00	0.30	0.12	0.77	0.07
1.0	0.05	0.46	0.10	0.29	0.04	1.13
1.2	0.26	2.29	0.64	--	0.40	--
Sum	**1.98**	**11.27**	**1.36**	**1.77**	**1.39**	**4.09**

Table 6.2 Continued

Time (s)	Knees Error SFCW	Knees Error CW in [3.5]	Torso Error SFCW	Torso Error CW in [3.5]
0.2	0.25	0.04	0.20	0.07
0.4	0.20	0.38	0.08	0.04
0.6	0.26	0.31	0.08	0.46
0.8	0.01	0.33	0.25	0.59
1.0	0.01	0.25	0.22	0.07
1.2	0.18	0.21	0.42	0.04
Sum	**0.91**	**1.52**	**1.25**	**1.27**

While in case of using 2-D data matrix collected using SFCW radar system, the velocity results agree closer with the results from the Boulic model. The reason is that in SFCW system, the row-enhanced Hankel matrix is formed from a sequence of Hankel matrix entries carried out on the rows of the 2-D data matrix. Thus, it provides a state transition matrix from which accurate poles can be extracted coherently as time evolves; and consequently, provides smoothness of the velocity estimates. While the simple Hankel matrix formed from the 1-D data vector collected by the CW radar provides a state transition matrix that exhibits few poles that provide coarse velocity estimates and even fall short in coherency as time progresses. This simple Hankel matrix can be considered as the first element of the row-enhanced Hankel matrix computed from the 2-D data matrix, $H_e^{row} = H_1^{row}$ ($M = 1$ and $J = 1$), due to the fact that the data set collected using a CW (single-frequency) radar system has only one row or a frequency point. The data vector obtained using CW radar can be represented by

$$y(n) = \sum_{i=1}^{P} a_i p_i^n + w(n)\,,\ n = 1, \dots, N \tag{6.8}$$

when comparing (6.8) to (5.1), it is not difficult to see that CW data does not provide range information, therefore the related poles (s_i) and consequently the associated μ-D frequencies (r_i) are absent. Subsequently, lack of information from range index had resulted in flatness around the maximum and minimum velocities in the obtained velocity curves in [3.5] upon implementing the 1-D block processing on CW data set.

Moreover, in SFCW system, forming the enhanced Hankel matrix from 2-D data enhances the computation of the model order as explained in Chapter Five. Using the knees that occur on the plots of the singular values computed from the enhanced Hankel matrices

(carried out on the original 2-D data) and the residual 2-D data matrices (using the superposition algorithm) provide far much higher accuracy.

6.3.3 Static Human Subject vs. Other Static Targets

As we previously mentioned, in physical therapy for example, we can use a real deep depth camera to help in measuring the range and remotely identify the number of persons in the scene as long as they are not far away. But, in the dark or behind the wall, we can benefit from utilizing the radar system to identify human subjects in this situation. We can use this radar system, as well, for non-contact human vital sign detection including their respiratory rate and heart rate and also their range (distance to the radar system). Even when a human subject is static, we can still detect their respiratory rate and chest displacement very clearly, using phase-based method (arctangent demodulation) for example. In fact, respiration is the feature that other static targets like a floor lamp do not have, and there are some studies that claim breathing pattern can be used as an ID for a specific person. In [2.11], we have used the same radar system to extract static human subjects' vital signs.

Where we initially, subtract the static background, and analyze the remaining of the data (i.e. the dynamic part) to extract the μ-D frequencies. For example, in Figure 6.5, the subject is standing while swinging his left arm and we are going to analyze this motion. Therefore, in order to extract the velocity of the swinging hand, first we remove the reflections from all static objects in the scene, including static background and even the static parts of the human subject, upon simply subtracting the average of the radar received signal from the original received signal. Now the remaining (residual) signal is only

associated with the motions in the scene which is from swinging hand and is used to apply the 1-D block processing to retrieve its instantaneous velocities.

Here is the mean subtraction to remove the static background means the new data will be (data = data – mean (data)). However, the static background subtraction eliminates only non-human static targets in the scene. In fact, a static person still breathes and his/her heart is working, so we should be able to identify his/her breathing rate (respiratory rate) and heart beating from Doppler shift they cause; even if he/she stops breathing we can detect their heart beat even better.

Therefore, in order to detect human subjects in the scene, we use the fact that static human subjects are different from static targets in the scene, due to their tiny body motions (breathing and heart beating). This fact is the basis of all our analysis in detection, tracking, and extracting human-related features such as vital signs and motions. In all cases, before implementing any algorithm, we first, subtract the mean value of the received signal by radar. In this way, we can make sure that the residual signal is from human subject, that has the highest intensity in the range profile. Figure 6.13 shows an example of vital sign detection from a static human subject. In this specific experiment, we put a corner reflector in the scene next to the human subject. As it can be seen in Figure 6.13 (b), in the range profile, we can see both static human subject and corner reflector (static target). Then, we subtract the mean of the data and again plot the range profile (Figure 6.13 (c)). In Figure 6.13 (c), we see only the human subject because although he is static, due to the breathing and other biological signs, his body has very tiny motions which are affecting the phase of the reflected signal and therefore, is detectable in the range profile.

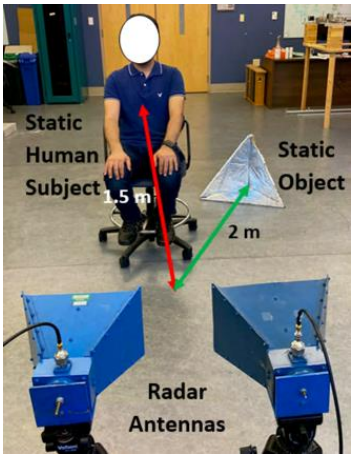

(a)

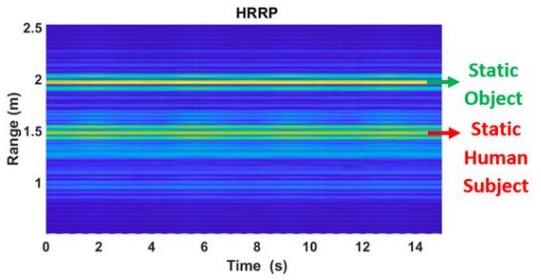

(b)

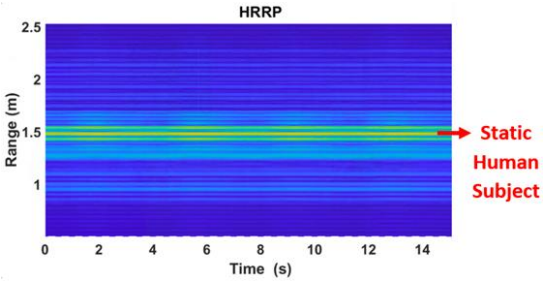

(c)

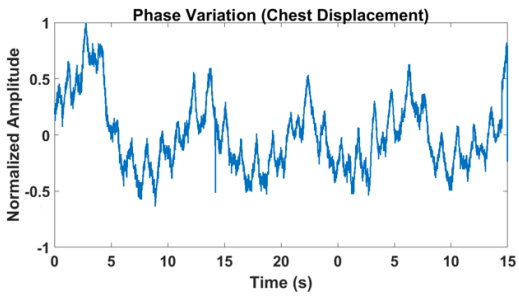

(d)

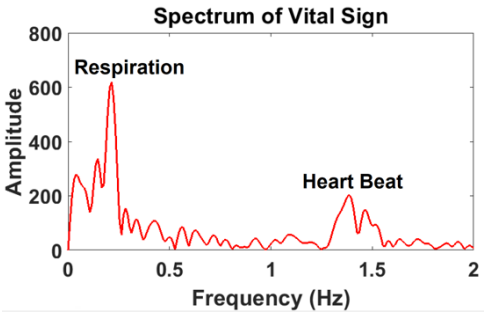

(e)

Figure 6.13 (a) Experimental setup for detecting static human subject using SFCW radar system; (b) High range-resolution profile (HRRP) (Range-Time-Intensity presentation) before removing the static background; (c) HRRP after removing the static background; (d) Extraction of tiny body motions due to the respiration and heart beat; (e) Vital signs extraction.

As a matter of fact, we use the range profile information to recognize the situation of two subjects existing in the scene. We need to emphasize here that we are looking for motions and motions analysis for these moving subjects. In this work, we have utilized the enhanced 1-D block processing to extract the velocity of "motion" caused by each limb joint. For example, if we consider that the total time of the experiment is T seconds, and a subject in the scene, has walked for t_1 seconds and was static for t_2 seconds, by implementing the mean subtraction step, we do not drop the information from this user for the period of t_1, because he/she was moving for that period, and by implementing the enhanced 1-D block on the remaining data for this period, we can extract his/her motion velocities. For the period of t_2, when the user is static, the velocities of all his/her body components are zero and we do not need to implement the 1-D block for this period of time to extract motion velocities. Therefore, by dropping the data of the period of t_2, we do not lose any information.

In fact, by subtracting the mean from the data, we remove the static background associated with the non-human targets in the scene. However, by mean subtraction and eliminating the static background, we cannot totally eliminate the static human subject from the range profile for the period of time he/she is static, because of the tiny motions of human body due to his/her heart beat, respiration, and body random motions. This fact is clear in Figure 6.14 (b) which is from the real experiment. Both subjects are moving for time period of t_1 and stop walking for period of t_2. However, by implementing the mean subtraction, still we can recognize them from the range profile for the period of t_2, and since their range does not change, we can figure out that they do not move (walk).

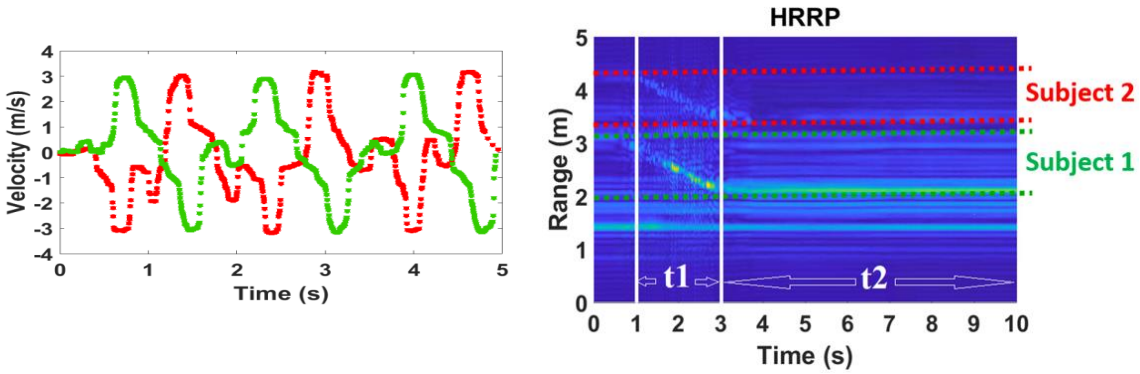

(a) (b)

Figure 6.14 (a) Experimental setup for multi-subject gait analysis using SFCW radar system; (b) Extracted high range-resolution profile recognizing the two subjects and their motion ranges. The two subjects walk for a period of t_1 and stand still for a period of t_2.

6.3.4 Signal-to-Noise Ratio (SNR) and Multi-Path Effect

To distinguish multiple subjects, the subjects need to be resolvable by the range resolution. Therefore, the far subject will surely lead to lower SNR. This low SNR problem could happen for a single-subject motion analysis or multi-subject analysis. In both cases, we first remove the static background by subtracting the average of the signal from the original data set.

For a single subject, we normally apply 1-D block on the original 2-D data set collected by SFCW radar. However, if the SNR is very low, we first form a range profile on the data set by applying inverse Fourier transform (iFFT) along the frequency (fast time) axis, and choose only the effective range bins related to the subject motions from the range profile. Afterwards, we apply 1-D block on each row (range bins) of this new 2-D data set and form the enhanced Hankel matrix using these effective range bins associated with the subject's motions. It helps us to de-noise the data set due to the subtraction of the noise (unrelated range bins and static background).

In case of multiple subjects, first we apply inverse Fourier Transform (iFFT) along the frequency axis to form the range profile. For example, Figure 6.5 (b) depicts the range profile that shows the separation between the two subjects in range directions (range-time intensity (RTI)). In the processing, first we separate the subjects by choosing the effective range bins. In this scenario, for the further subject with lower SNR, we choose the effective range bins among the red lines. We implement the 1-D block processing by forming the enhanced Hankel matrix from this new 2-D data set. The extracted hand velocities, for example, by the 1-D block processing technique are presented in Figure 6.5 (c). As it has

been shown in the range profile of the Figure 6.5 (b), the SNR related to the second subject is much lower than the first subject due to the second subject's further distance to the radar. However, as depicted in Figure 6.5 (c), 1-D block is set to retrieve the velocities of the different body components of the second subject as well as the first one. In fact, the 1-D block approach is a proper technique for gait analysis for SNR envirnoment. Given that the poles in the signal model in (6.9) contain the information of target motion and are critical for signal component separation in μ-D feature extraction. The poles automatically represent the roots of the denominator of the transfer function of an autoregressive moving average derived from the state-space equations [5.3], [5.4].

$$y(m,n) = \sum_{i=1}^{P} a_i s_i^m p_i^n + w(m,n) \quad m = 1, \dots, M \; and \; n = 1, \dots, N \qquad (6.9)$$

using these simole fact, the residual superposition technique when used in the 1-D block processing helps us to retrieve the μ-D features of all components including the strong (with higher SNR) and the weak (with lower SNR) ones. So, using the superposition approach, we first extract the strong components, followed by subtracting them from the model to retrieve the weaker components and then superpose them.

The 1-D block is being exploited in time direction to analyze the motions of the subjects. As long as the radar has sufficient PRF and the subjects are within the radar detectable (unambiguous) range, the 1-D block processing exploits the coherence between the consecutive time series and the smoothness provided by the inherent structure to provide μ-D features of the subject over time [5.4].

Here, the proposed method however is a multipath-limited, where in some cases the multipath signal could be even stronger than the one from the subject. In this case, the

direct signal model may assign most of its signal poles to the multipath. Hence, the motion estimates may be erroneous. Fortunately, one way to reduce this multipath effect is to thread the 2-D data set via a 2-D state-space model from which pole clusters - corresponding to multipath- can be first excised before carrying out the motion estimates. It is worth mentioning here that in our conducted experiments the radar was pointed directly to the subjects so multipath that occurred could be due to the short distance between the two human subjects. Other ways to reduce multipath effects include using antennas with very directive beams and steer the beam on each subject separately, or using MIMO arrays to reduce unwanted signals. Consequently, the radar's return signal would be only from the moving subject and does not include multipath signals if coherency is correctly utilized.

However, by having more subjects present in the scene (multi-subject scenarios), the multipath effect is stronger and affects the results as shown in Figures 6.6 (d) and (f); unless the subjects are clearly separated based on their range bins, and we will see some kind of distortion. As mentioned, to reduce multipath in these cases using antennas with very directive beams and steering the beam on each subject separately, or using MIMO arrays to reduce unwanted signals can help.

6.4 Conclusion

In this work, SFCW radar with PRF of 200 Hz was adequately used to investigate the feasibility of tracking relatively fast-moving body parts. The velocities are extracted by the enhanced 1-D block implemented on 2-D data sets by forming an enhanced Hankel matrix carried out on each row of the data matrix. Here, for a 1-GHz bandwidth system, the range

resolution capability of the SFCW radar is adequate to track multiple subjects' motions based on their range bins. Results agreed very well with the ground truth (Boulic model), though slight degradation was observed. This degradation is related to multipath and mutual coupling effects created by the two subjects being close in the scene.

Results achieved from the SFCW radar are robust, reliable and very encouraging. However, the process is computationally expensive. First, the use of the residual superposition algorithm that gives rise to extraction of weak motions throughout the block size selection and estimation of model order is computationally expensive. Second, forming the enhanced Hankel matrix from each row/column from a large 2-D data set also increases the computational cost. Thus, we need to implement smart, reliable algorithms to reduce the computational cost and automate the entire process. Intelligent schemes like machine learning including deep learning methods, could significantly help here. Moreover, dimensionality reduction could effectively cut down the computational intensity and execution time and bring the proposed technique to be carried out in quasi-real time.

Moreover, the most difficult challenge in indoor environments is the multipath effect. Specifically, wireless signals reflect off all subjects in the environment making it hard to associate the incoming signal with a particular location. The proposed method however is a multipath-limited, where in some cases the multipath signal could be even stronger than the one from the subject. Hence, the direct signal model may assign most of its signal poles to the multipath. And therefore, the motion estimates may be erroneous. Multipath effect is typically a big issue when we use time delays to discriminate between different targets as we do here. Although it is very challenging to eliminate the effect of multipath, there

are some ways to reduce its impact. For example, one way is to use correlation to see if it is the same signal or not. Other researchers used two radars (like in MIMO for example), to de-noise the real signals from clutter and multipath effects.

Interference is another factor that may severely impact the returns from the human subjects that reach the radar; thus, the signal model would give estimates that do not lie within the true motion values of the subjects, especially when the interference is strong and within the same frequency range, so it is fair to call the system interference limited.

One way to remedy the situation is for the radar to be equipped with an interference nulling process or multi-band frequency operation so the radar can either excise the interference or switch band to bypass it. Thus, returns from the human subjects can reach the radar with minimal interference, i.e., suppressed, and the proposed signal model can give reliable motion estimates.

Generally speaking, the beauty of the proposed 1-D block method implemented on a 2-D data set is that it can utilize any 2-D data sets including those from SFCW radar whatever it is a range profile, STFT spectrogram, etc. and would give reliable analysis from a human subject's motion, walking alone or with other subjects.

CHAPTER SEVEN
HUMAN VITAL SIGN DETECTION USING HIGH-PERFORMANCE RADAR SYSTEM AND SSM

Due to the reliable data collected using a high-performance SFCW radar system, and successful implementation of the state-space method (SSM) on the data collected using this radar system for gait analysis purposes, in this chapter, we use a high-performance SFCW radar and extend SSM for human vital sign detection in single- and multi-subject scenarios. Moreover, we use the high-performance SFCW radar system to develop multi-input multi-output (MIMO) system that can help to estimate human vital signs with higher accuracy.

7.1 Human Vital Sign Detection using High-Performance SFCW Radar and State-Space Method

In Chapter Five, we explained state-space method (SSM), and in Chapter Six, we applied SSM to the data collected using SFCW radar system to retrieve gait features from a single and multiple human moving subjects. Although, human gait is much more complex compared to human vital signs due to the respiration and heartbeat (a sort of body motion, i.e. the chest), SSM was capaable of diserning μ-D features of a human gait (or the velocity of different limb joints of a human body), successfully. Moreover, the developed high-performance SFCW radar system comprising fast-switching frequency hardware and adaptive data decimation algorithm was used to provide reliable data set as the input of a SSM-based signal processing technique. On the other hand, human body motion due to the respiration and heart beating are much simpler motions and have periodic nature.

Therefore, they impact the frequency of the radar signal and cause Doppler shift in the radar return signal, which can be extracted and retrieved from the radar phase variation signal. However, as mentioned in Chapter Two, respiration signal has a strong harmonic near the peak from heartbeat, which makes it really challenging to discern and identify heart rate. Almost there is no processing techniques that is completely immune to this issue. However, SSM-based techniques seem to show the most potential due to their nature. Hence, due to the promising results of SSM implementation for gait analysis, we have expanded SSM to retrieve human heart rate. In Chapter Two, we described the arctangent demodulation (AD) method [2.18] that benefits the information from the in-phase (I) and quadrature-phase (Q) down-converted signal received by the radar. Therefore, AD is using phase information of the radar signal which is sensitive to any motion to extract respiratory and heart rates. As we mentioned in Chapter Six, any kind of data can be used as the input of SSM, such as raw data or range profile data. Here, we use phase variation signals obtained from AD as the input to the SSM, since it includes motion information due to the subject's respiration and heartbeat. In fact, in this work, we use the combination of AD and ST-SSM to overcome the challenge of extracting the heartbeat peak from the harmonic of the respiration and identifying it to increase the accuracy of the results.

7.1.1 Short-Time State-Space Method (ST-SSM) for Human Vital Sign Detection

As we mentioned, state-space method refers to a signal processing technique used to extract frequency content of a signal. As described in [5.4], we assume that the scattered signal representing the subject's respiration and heart waveforms are of the form

$$y(k) = \sum_{i=1}^{M} a_i e^{-(\alpha_i + j2\pi\tau_i)f_k} + w_k \tag{7.1}$$

where the subscript $k = 1, \dots, N$ is used to denote the frequency content of the signal and w_k is the associated noise. In (7.1) a_i, and α_i are the amplitude and decay factors of the scattering center. Finally $\tau_i = -\frac{\varphi_i}{2\pi\Delta f}$, , where φ_i is the phase of the eigenvalue of the eigenvalue λ_i of the i^{th} scattering center. The objective of SSM is to determine these eigenvalues, as well as the amplitude and decay factors in order to reconstruct the measured signal and recover the frequency content therein. However, here we apply ST-SSM to the data vector (phase variation signal as the output of AD method) to retrieve HR.

7.1.2 Experimental Results

We begin by inspecting a typical range profile of a human subject shown in Figure 7.1 (a). Here, the range bin corresponds to the physical distance of the subject away from the radar. The range index containing the maximum intensity (absolute value) is selected and the corresponding phase variation is plotted in Figure 7.1 (b).

The frequency spectrum of the phase variation contains the information about the respiration and heart rates; however, looking at the spectrum directly can be misleading due to the presence of respiration harmonics and various measurements noise, especially in the case of automating heart rate estimation. Figure 7.2 (a) shows the normalized magnitude of the spectrum of the filtered phase variation from 0.8Hz to 3Hz. In this case, the subject's measured heart rate was 86.5 bpm, but the highest peak in the spectrum is around 107.8 bpm. Processing the phase variation using ST-SSM yields the spectrum in Figure 7.2 (b), with estimated heart rate of 84.4 bpm.

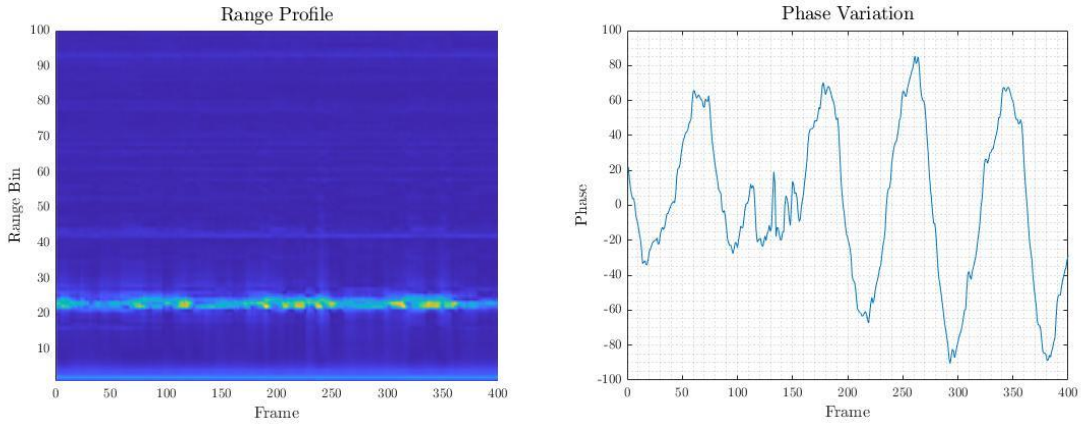

(a) (b)

Figure 7.1 (a) Range profile; (b) Phase variation.

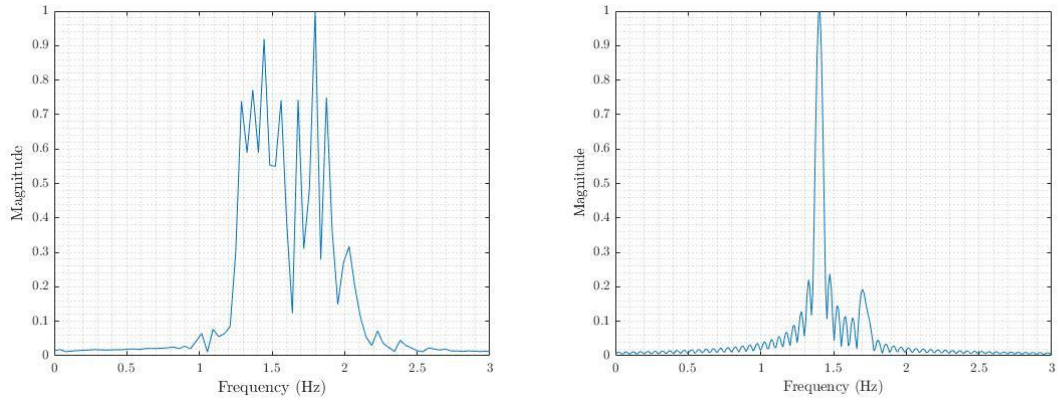

Figure 7.2 (a) FFT of Phase Variation; (b) ST-SSM.

7.1.3 Multi-Subject Human Vital Sign Detection

Since the results from the combination of AD and ST-SSM on SFCW radar data are very encouraging, my colleague, Tsotne Kvelashvili, and I used this high-performance radar system and ST-SSM applied on the phase variation signal achieved using AD method for multi-subject vital sign detection. In this work, we set the experiments with two human subjects in front of the radar and used the belt sensor and pulse sensor as our references while collecting data from the subjects using SFCW radar system. The subjects are in front of the radar and have at least 50-cm radial distance from each other. Figure 7.3 indicates the experimental setup.

In this way, after removing the static background first, then we form the range profile or HRRP. From HRRP we can differentiate the subjects from each other and identify them. After forming HRRP, we select the effective range bins associated with each subject and separate the HRRP data into two data sets. Then, we apply AD to each set of effective range bins. Afterwards, we apply ST-SSM on the phase variation signals (AD output) and retrieve each subject's HR. The results from the pulse sensor and SFCW radar data for different situations (subjects' distances to the radar) are shown in Figures 7.4 to 7.10.

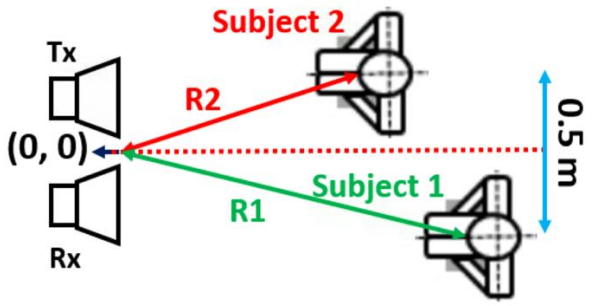

Figure 7.3 Experimental setup for multi-subject human vital sign detection.

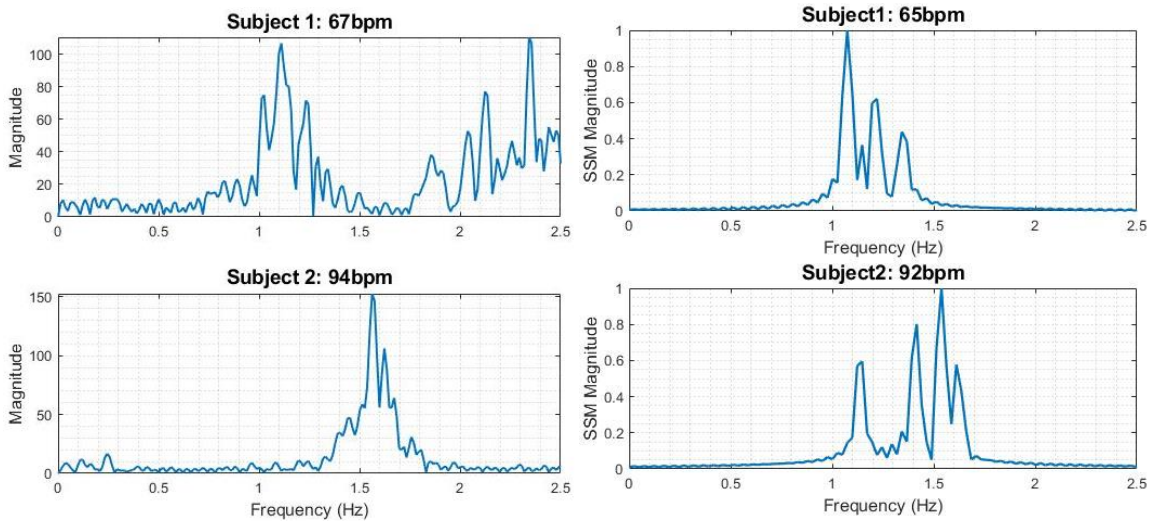

(a) (b)

Figure 7.4 Results of multi-subject human vital sign detection (HR) from applying AD and ST-SSM to the data collected using (a) reference sensor, and (b) SFCW radar system. Subject 1 range: 170 cm, and Subject 2 range: 210 cm.

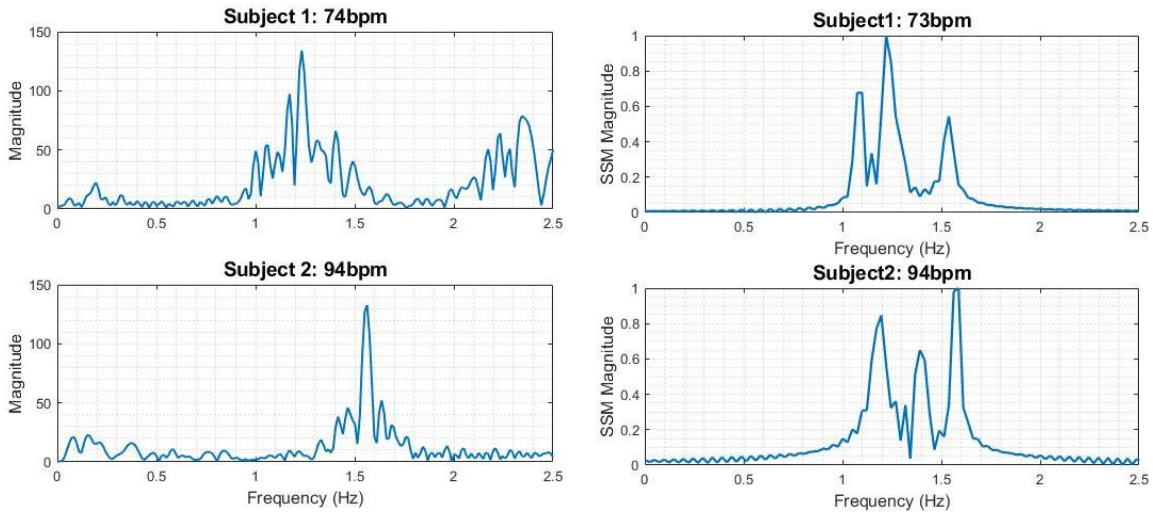

(a) (b)

Figure 7.5 Results of multi-subject human vital sign detection (HR) from applying AD and ST-SSM to the data collected using (a) reference sensor, and (b) SFCW radar system. Subject 1 range: 170 cm, and Subject 2 range: 190 cm.

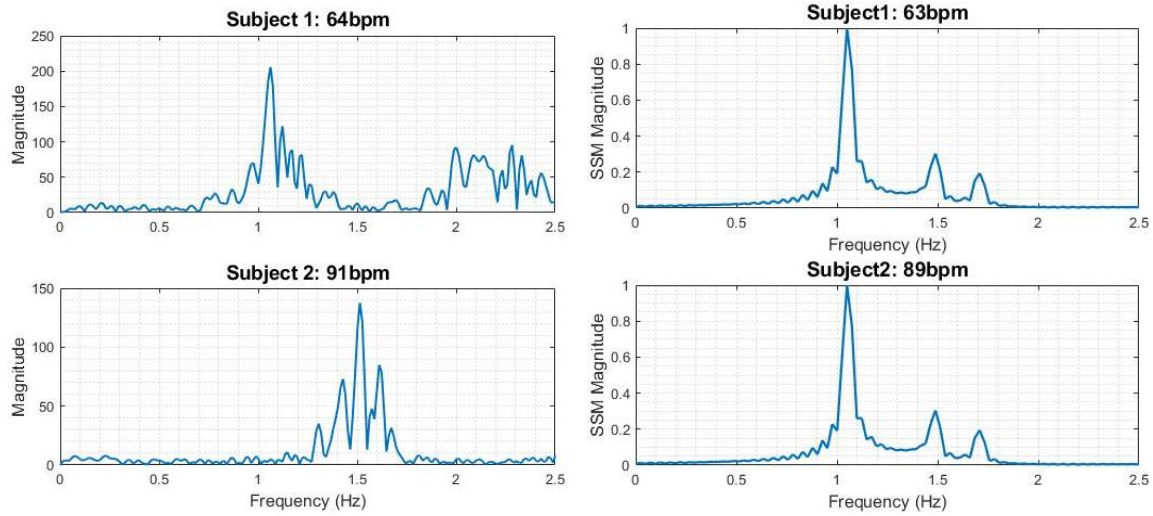

Figure 7.6 Results of multi-subject human vital sign detection (HR) from applying AD and ST-SSM to the data collected using (a) reference sensor, and (b) SFCW radar system. Subject 1 range: 170 cm, and Subject 2 range: 170 cm.

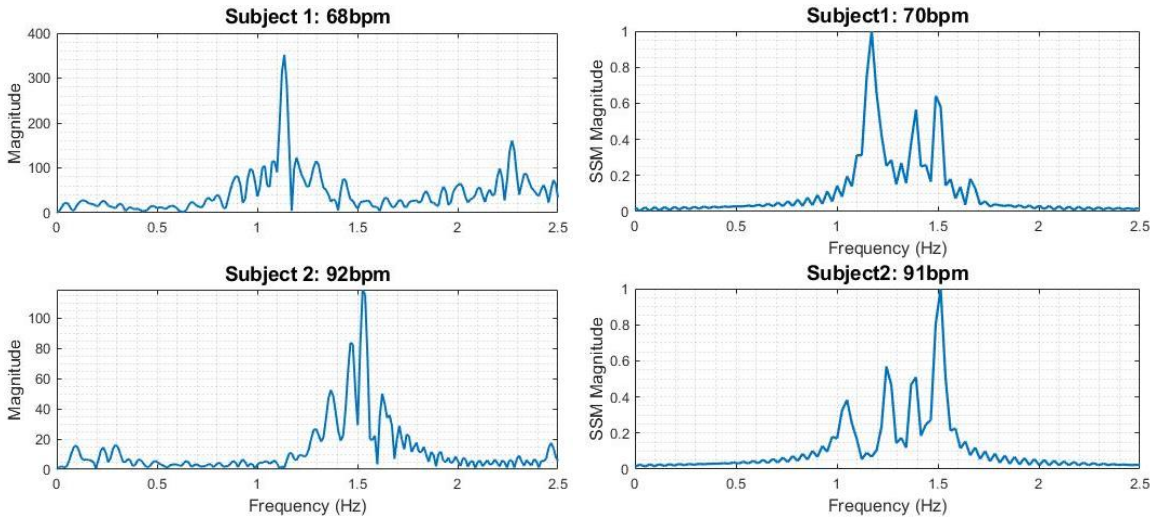

Figure 7.7 Results of multi-subject human vital sign detection (HR) from applying AD and ST-SSM to the data collected using (a) reference sensor, and (b) SFCW radar system. Subject 1 range: 170 cm, and Subject 2 range: 150 cm.

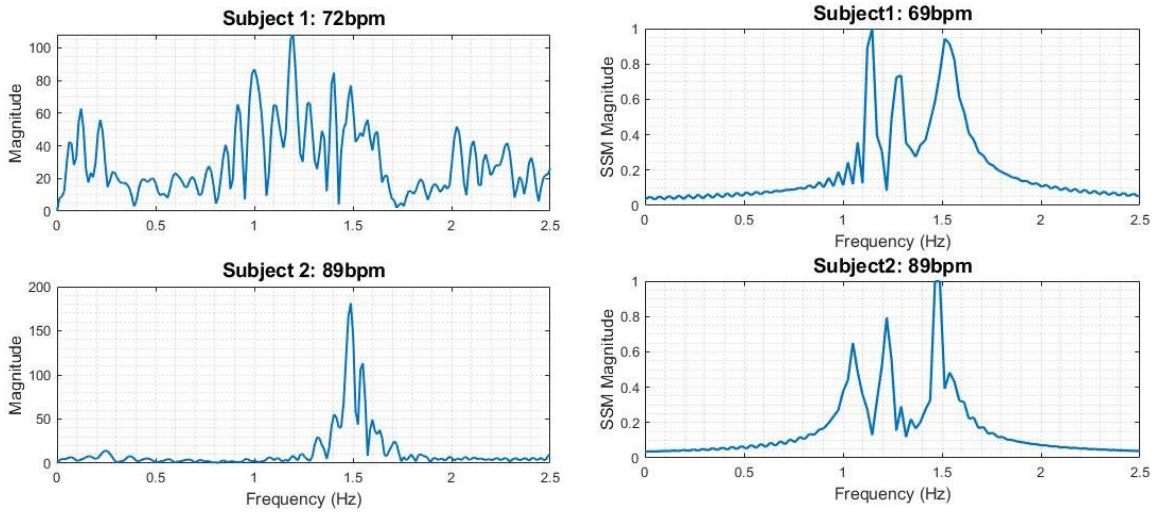

Figure 7.8 Figure Results of multi-subject human vital sign detection (HR) from applying AD and ST-SSM to the data collected using (a) reference sensor, and (b) SFCW radar system. Subject 1 range: 170 cm, and Subject 2 range: 130 cm.

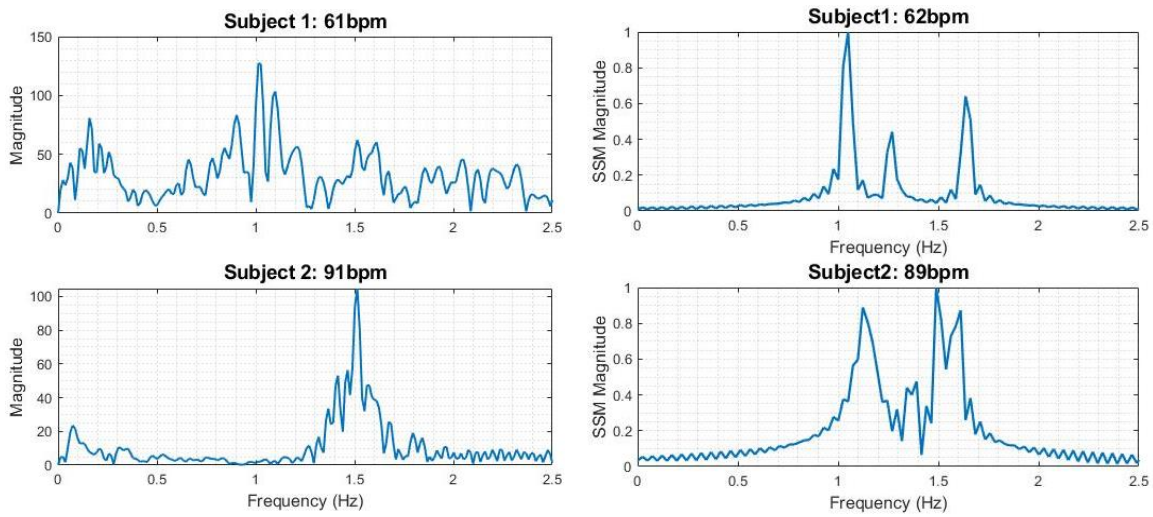

Figure 7.9 Results of multi-subject human vital sign detection (HR) from applying AD and ST-SSM to the data collected using (a) reference sensor, and (b) SFCW radar system. Subject 1 range: 170 cm, and Subject 2 range: 110 cm.

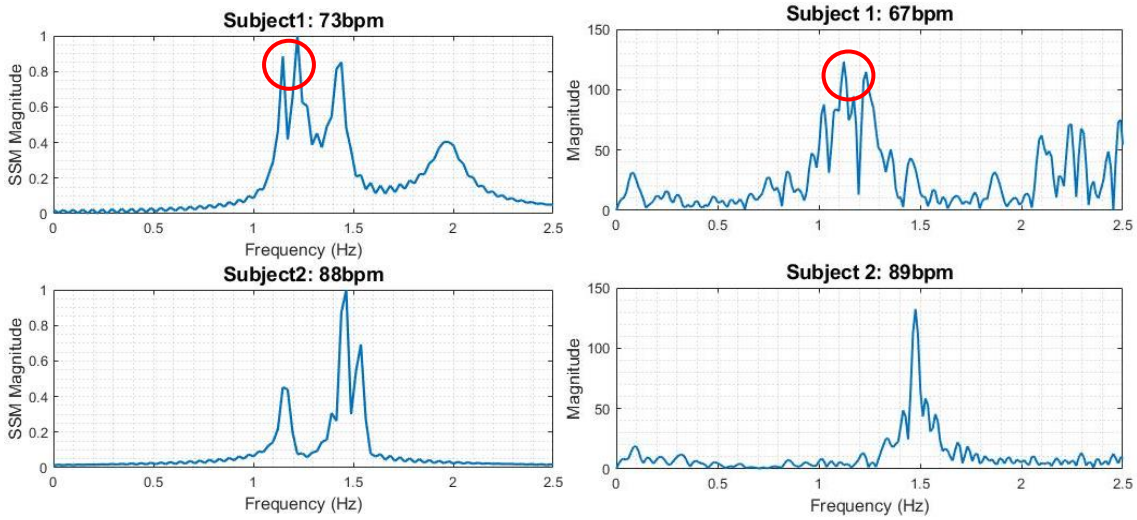

Figure 7.10 Results of multi-subject human vital sign detection (HR) from applying AD and ST-SSM to the data collected using (a) reference sensor, and (b) SFCW radar system. Subject 1 range: 170 cm, and Subject 2 range: 90 cm.

The results are very promising and show that ST-SSM that uses the phase variation signal, obtained from AD method, as an input is capable of retrieving HR in multi-subject scenarios with good accuracy.

However, as previously mentioned even SSM is not immune from the strong harmonic of the RR issue, especially when we have more subjects in the scene and the multi-path effect and mutual coupling between the subjects have stronger impact on the data. As it can be seen from Figure 7.10, there are two close peaks in both results from pulse sensor and SFCW radar for Subject 1. In these cases, deep learning techniques for non-contact human vital sign monitoring are recommended.

7.2 Multi-Input Multi-Output (MIMO) SFCW Radar System

Although the developed high-performance SFCW radar system provides reliable data from the subject, there is a situation, in which retrieving subject's vital sign is very challenging. This situation likes when the subject is not facing the radar antenna and has a different orientation or angle with respect to the radar antenna boresight, and happens often in real situations.

To address this problem, we conducted a complete set of experiments, as explained in Chapter Two, Section 2.5 [2.11]. In that set of experiments, data of one subject at different distances to the experimental instruments was collected with four orientations (front, back, right, and left) of the subject to the radar antenna and camera. From these results, shown in Figure 2.17, we can see that the results when the subject has an angle to the radar estimations are not as accurate as the ones when the subject is facing the radar. However, in many cases and situations that not only the subject is not facing the radar system, but

also is not in front of the radar (has an offset to the right or left) or is in a far distance, the estimated vital signs from the measurements are completely wrong and off from the reference results. Therefore, using multi-input multi-output (MIMO), in which instead of one transmitting antenna and one receiving antenna, there are several of each in different locations, can help us to collect data and information from the subject from different locations (point of views). In this work, we reconfigured the SFCW radar system as a MIMO, to have one transmitter and four receivers. All four receivers, collect data from the subject, simultaneously.

7.2.1 Hardware Development

It is very common to use RF switches for MIMO configurations. In this way, data is collected by each receiving antenna by switching between them very fast. However, due to the nature of SFCW signal, which is a sinusoidal contiguous-wave signal, using RF switches causes to lose part of signal and data, even if the switch is very fast and high-performance one. Therefore, in this work, to create a MIMO SFCW radar with one transmitting channel and four receiving channels, we used a 1-to-4 power splitter to divide the SFCW signal generated in transmitter path into four equal parts and with the same phases and inject each part into the signal that is received by each receiving antenna to down-convert it. On the other hand, at the receiver path, each receiving antenna is connected to an LNA and then goes to a mixer to mix with the in-phase and quadrature-phase RF received signal with the injected LO signal coming from the transmitter side and divided by 1-to-4 power splitter to create I and Q signals.

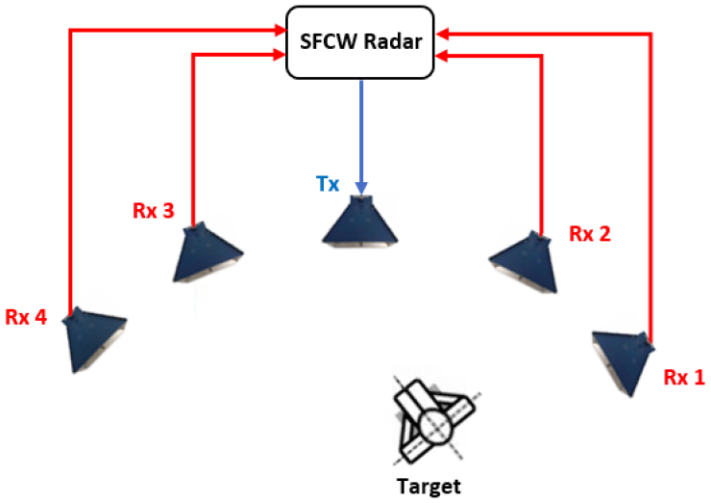

(a)

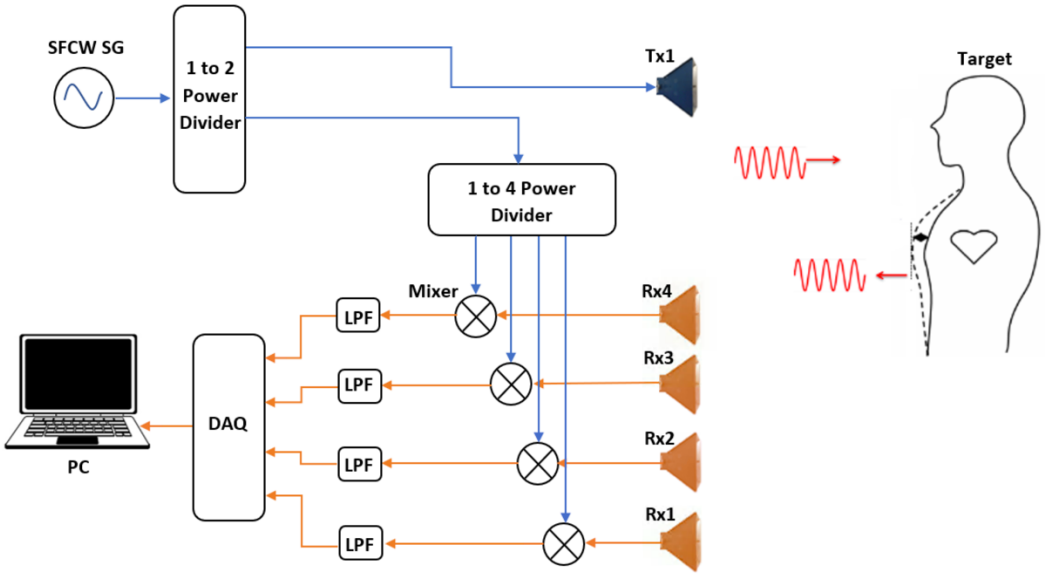

(b)

Figure 7.11 (a) MIMO SFCW radar system with one transmitter and four receivers (top view); (b) Block diagram of the MIMO SFCW radar with one transmitter and four receivers.

Therefore, each receiving channel includes I and Q channels that are filtered using low-pass filters and are digitized using an ADC. Here, we use the same ADC mentioned in Chapter Four, since it has 8 channels and is able to sample the data very fast. Figure 7.11 shows the block diagram of the developed MIMO SFCW radar.

7.2.2 Signal Processing

MIMO system results in a channel diversity of the system and can be used to improve SNR of the signals. In order to combine all the information and data sets collected using different receiving channels of the MIMO system, we can use the conventional method of averaging all the channels information. However, in this way, if the error of one channel is high, it increases the error of the results obtained from averaging all channels. A well-known method that improves the SNR of the signal is Maximum Ratio Combining (MRC) [7.1], that was implemented by my colleague, Kellen Oleksak, successfully on the data collected using a commercial MIMO (comprising two transmitters and four receivers) mm-wave FMCW radar system from TI. Therefore, we applied MRC on our MIMO SFCW radar system data. The MRC model for combining channels is given in [7.1] by

$$f(t) = \sum_{i=1}^{N} a_i f_i(t) \tag{7.2}$$

in which each f_i is weighted by a combining coefficient a_i which is proportional to the channel gain and may be allowed to vary in accordance with the fluctuating local statistics of the $f_i(t)$. The value a_i is also described as $\frac{x_i}{n_j^2}$ where x_i is the channel rms voltage and n_i^2 is the mean square noise source at the channel. In effect, this summation reduces the channels which are noisy prior to combining so they do not contribute to the summation as much.

The MRC processing first calculates a cross correlation matrix from time domain signals of multiple channels

$$R_{XY} = \sum_{k=1}^{N} X_k Y_{k+n}^T \tag{7.3}$$

where superscript T is a transpose operator. Now that a square matrix has been created, eigenvalue decomposition is performed resulting in,

$$R_{XY} = [v_1 v_2 \dots v_N] diag[\sigma_1 \sigma_2 \dots \sigma_N][v_1^* v_2^* \dots v_N^*]^T \tag{7.4}$$

where σ_{1-N} are the eigenvalues and v_{1-N} are the eigenvectors for N channels. This MRC method uses the first eigenvector as weights for the received signal on all Tx-Rx pairs such that

$$f_{MRC}(t) = v_1^H f(t) \tag{7.5}$$

where H represents a complex conjugate transpose.

7.2.3 Experimental Results

Figure 7.12 shows the experimental setup using the MIMO SFCW radar system with one transmitter and four receivers in an indoor lab environment. The performance of the MIMO SFCW radar system and algorithm mentioned above were assessed through measurements with different participants. The measurement time was 20 seconds in each experiment. Respiration monitor belt sensor and pulse sensor were used as respiratory and heart rate ground truths, correspondingly. The radar system mentioned above was used to record data from the human subject at the same time to quantify its performance error on the basis of the ground truth. In these set of experiments, we consider the worst situation, where not

only the subject has angle to the antenna, but also has an offset to the right and is not in front of the transmitting antenna (is not in receiving channel boresight).

After collecting data using MIMO SFCW radar system from the subject, we process the data of each receiver using phase-based method (here AD) separately, and using MRC. Figures 7.13 to 7.16 show the results of heart rate for each receiver and Figure 7.17 shows the MRC results. Moreover, the received power from the four channels of the receiver and MRC are shown in Figure 7.18.

MRC plays an important role in improving SNR of the combined signals as well as eliminating uncorrelated channels from the process to make sure those bad channels do not contribute significantly to the compiled estimation results. As can be seen from Figure 7.18, the SNR has been improved significantly using MRC compared to the SNR of channel 4.

In order to evaluate MRC performance, we have summarized the performance of MRC, the best, and the worst channel by calculating the error from each (compared with the contact sensor).

Although the error of applying MRC is relatively larger than the one from the best channel, we need to remember the fact that in real situations, we do not use the contact sensor as our reference. Therefore, we do not know which channel is really the best channel. In this way, MRC helps us to avoid overestimating or underestimating the heart rate. However, MRC is not the best way of heart rate estimation in case of using MIMO system.

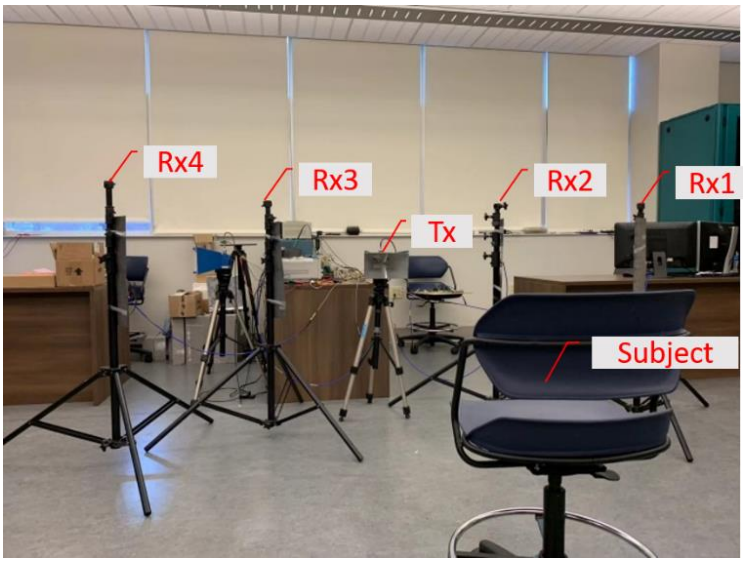

Figure 7.12 Experimental setup using the MIMO SFCW radar system with one transmitter and four receivers in an indoor lab environment.

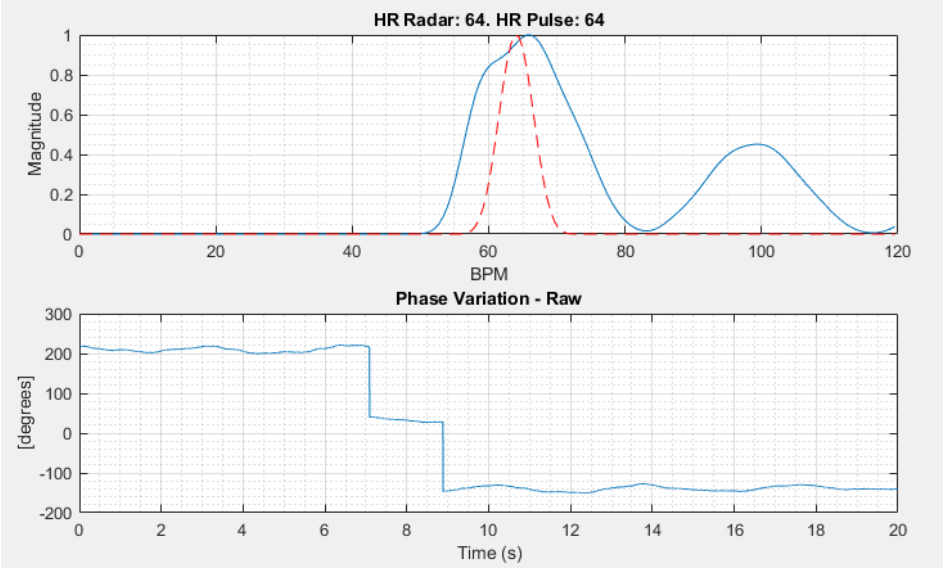

Figure 7.13 Heart rate estimation (top) and phase variation signal (bottom) from receiving channel 1 (Rx1) (Red curve: reference sensor).

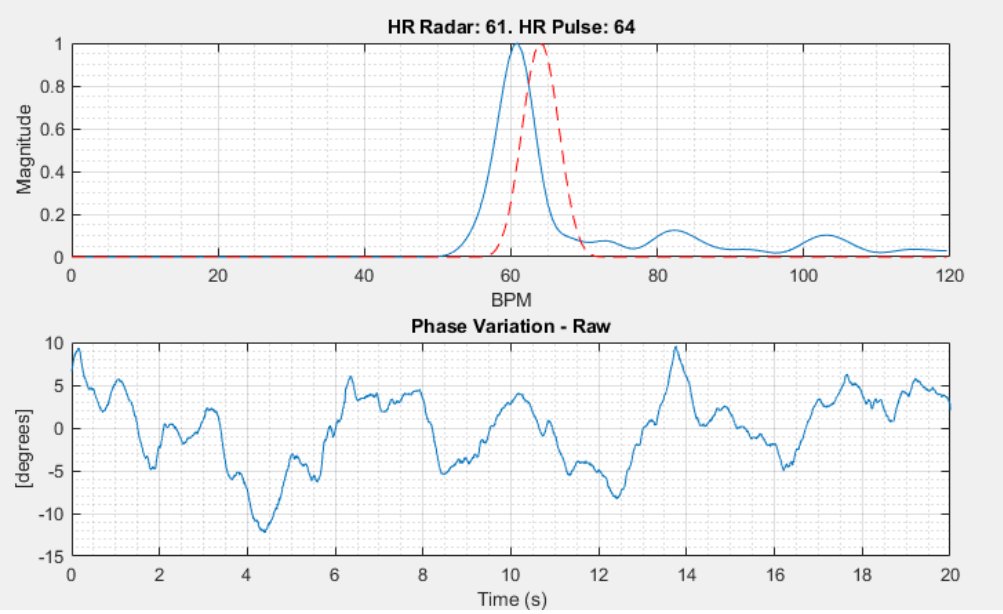

Figure 7.14 Heart rate estimation (top) and phase variation signal (bottom) from receiving channel 2 (Rx2).

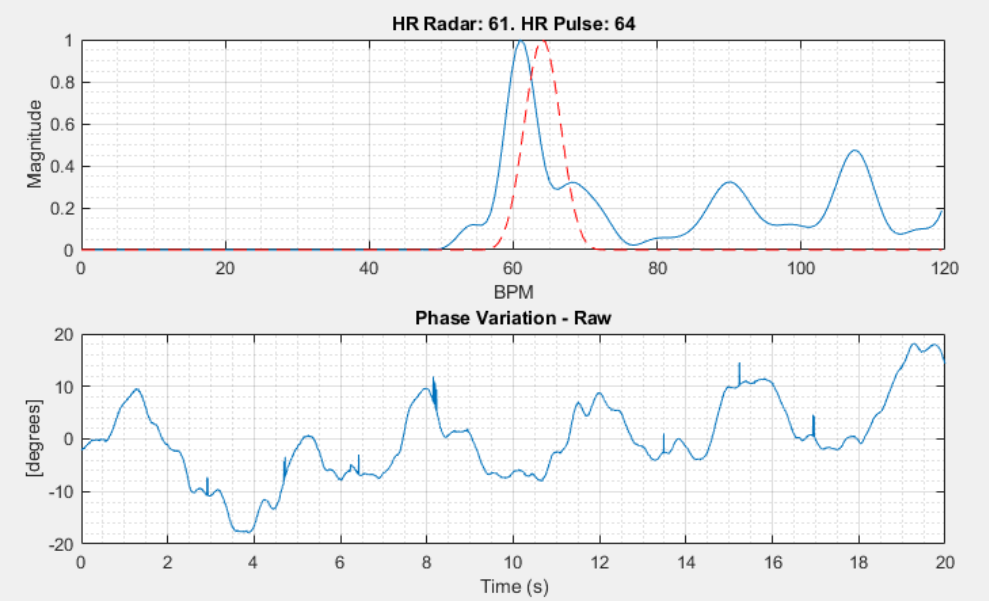

Figure 7.15 Heart rate estimation (top) and phase variation signal (bottom) from receiving channel 3 (Rx3).

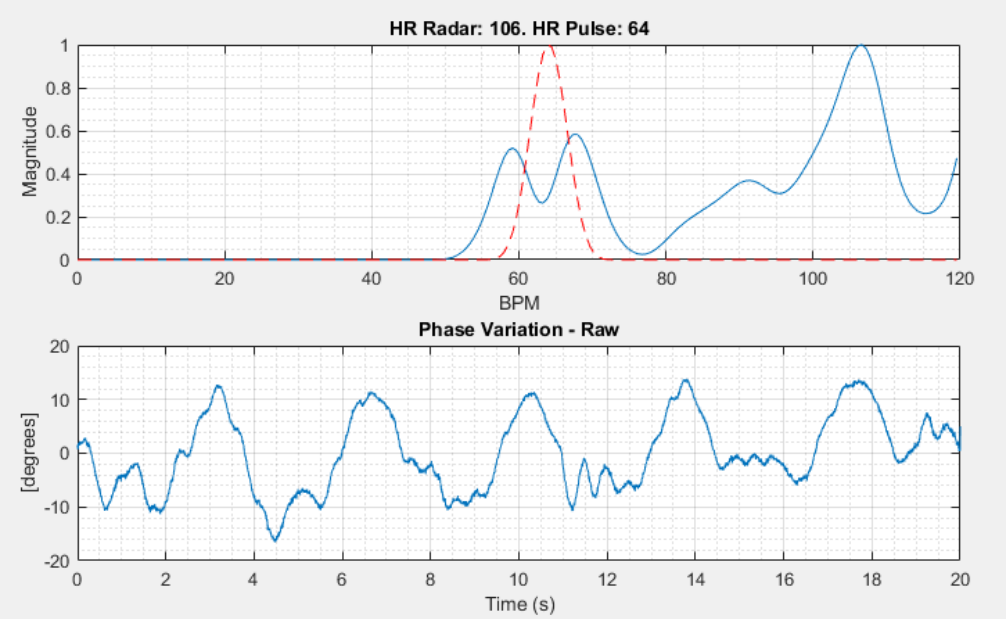

Figure 7.16 Heart rate estimation (top) and phase variation signal (bottom) from receiving channel 4 (Rx4).

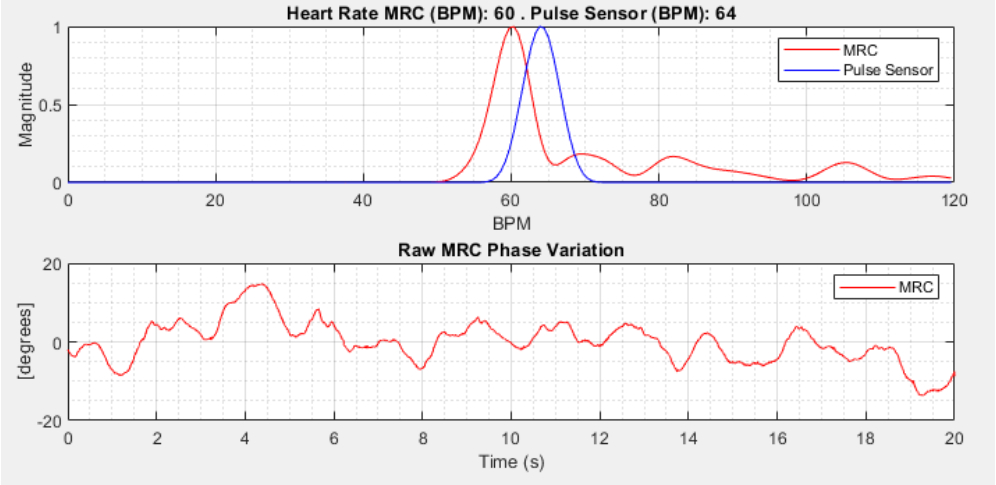

Figure 7.17 Heart rate estimation (top) and phase variation signal (bottom) from MRC.

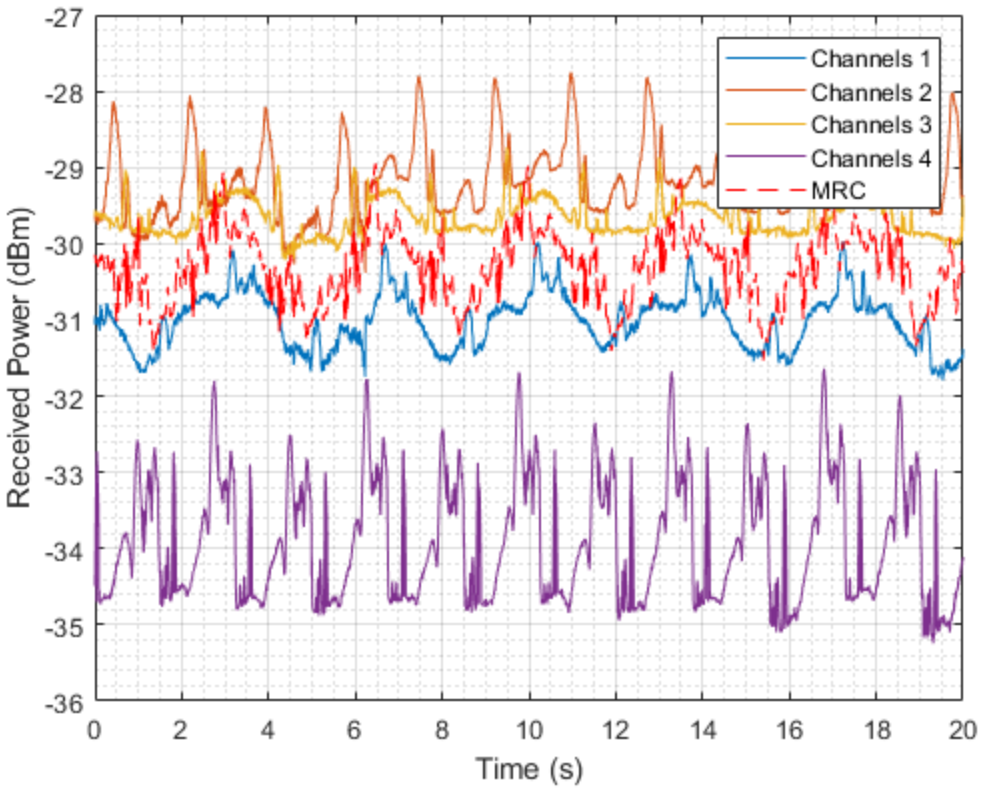

Figure 7.18 Received Power comparison between MRC and separate receiving channels.

Table 7.1 Error (BPM) Comparison between MRC, The Best, and The Worst Receiving Channels.

MRC Error (bpm)	**Best Channel Error (bpm)**	**Worst Channel Error (bpm)**
4	0	42

7.3 Conclusion

In this chapter, we used the developed high-performance SFCW radar system explained in Chapter Four to collect data from human subject(s). Then, we took advantage of SSM to estimate vital sign parameters, specifically heart rate which is really challenging compared to the respiratory rate. In this way, we used the output of AD method, which is phase variation signal, as the input of ST-SSM to estimate HR. Moreover, due to the encouraging results for single subject, we applied this method to the multi-subject scenarios and could retrieve the HR of each subject with a good accuracy.

However, as mentioned, none of these techniques are immune to the strong respiration rate harmonic. Using artificial intelligence (AI) can help to identify the heart beat peak from the adjacent peaks from the harmonic of RR and noise from other sources. However, compared to the traditional approach such as Fast Fourier Transform (FFT), State Space Method (SSM), etc., AI techniques usually require long data acquisition time to produce accurate estimation of respiration rate (RR) and heart rate (HR).

Another challenge of retrieving HR in real situations, is that the subject is not always facing the radar or in front of the radar. Therefore, we developed a MIMO SFCW radar system with one transmitter and four receivers to collect data from human subject from different locations. MRC is one of the combining techniques that can help avoiding wrong estimation. The results show that the MIMO SFCW radar data are reliable and the feasibility of using MIMO for vital sign detection when the subject is in different situation in an indoor environment, especially for elderly care. In these cases, different antennas of receiving channels can be located in different locations of a room (e.g. each edge of the

room at the ceiling) and collect the information from human subject. However, MRC is not the best way of data combining. There is still room for improvement using other techniques of data fusion to improve SNR and estimate HR much more accurately or even in implementing MRC.

CHAPTER EIGHT
CONCLUSIONS AND FUTURE WORKS

This work has been supported by the US Army Medical Research and Materiel Command under Contract No. W81XWH-14-C-0004 (Title: VitalWave: Remote Triage of Combat Casualties.) Army SIRB Phase I and Phase II and eligible for funding for Phase III. (Primary contractor: MaXentric Technologies LLC).

In the conduct of research where humans are the subjects, I adhered to the policies regarding the protection of human subjects as provided by Code of Federal Regulations (CFR) Title 45, Volume 1, Part 46; Title 32, Chapter 1, Part 219; and Title 21, Chapter 1, Part 50 (protection of Human Subjects).

This project has been the focus of our research group at UT. It involved many colleagues and collaboration with other universities and companies. Our group collaborated with Catholic University of America (CUA) for developing EM analysis that has been used extensively in the early stage of the project. We, collaborated extensively with MIT Lincoln Laboratory (MITLL) to implement their SMM and 1-D block algorithms to enhance and complement our experimental radar studies. Meanwhile, MaXentric Technologies LLC was the prime contractor in all these SBIR projects.

My lab partner (Lingyun Ren) was tasked with investigating use of impulse radars for both vital sign detection and simple body motion, while Farhan Quaiyum was interested in pushing the use of CW radars to detect motions and vital signs as well. My main task was the use of SFCW radars, but worked closely with Lingyun Ren then Chandler Bouder to implement optical techniques for RR, HR, BP, and SpO_2 as well.

I have initialized multi-subject gait analysis, and Tsotne Kvelashvili joined forces recently to extend multi-subject vital sign in standstill position and in motion as well. This work is still in progress. Meanwhile, Kellen Oleksak, Toan Vo Dai, and Tsotne Kvelashvili have been tasked by realizing this effort at mm-Waves to provide portable radars systems. In my tasks, I have studied and explored non-contact methods for human vital sign detection using both camera-based imaging photoplethysmography and radar-based techniques and a full comparison study was published at IEEE. I concluded from this extensive study that optical techniques using two cameras or even one can help in detecting vital signs, BP and SpO_2 for close by stand-still subjects in adequately lit regions. For long distances then, radar techniques are favored especially in dark areas, or behind walls. My early work on impulse radars and Farhan on CW radars led the way to analyze simple single subjects but were not adequate for complex motions. Based on extensive trouble shooting, and use of advanced signal processing implemented on 2-D data, I was able to discern fast moving body parts like toes. I utilized the 1-D block algorithm to even monitor the motion of more than one subject.

Lingyun Ren previously used SSM for vital sign detection of a single subject, Sabikun Nahar used SFCW to detect vital signs of multi-subjects. She was successful in detecting RR but was not able to track HR. Here, I was able to use SSM to discern the motion and HR of multi-subject using the high performance SFCW radars.

So in this work, a high-PRF SFCW radar system were developed to retrieve the velocity of fast moving components of human body while walking. In fact, SFCW radar with PRF

of 200 Hz was adequately used to investigate the feasibility of tracking relatively fast-moving body parts;

The enhanced 1-D block processing technique were developed on two dimensions to extract the velocity of different body components more accurately by forming the enhanced Hankel matrix. The velocities were extracted by the enhanced 1-D block implemented on 2-D data sets by forming an enhanced Hankel matrix carried out on each row of the data matrix;

And the experiments were expanded successfully to multi-subject motion scenarios. For a 1-GHz bandwidth system, the range resolution capability of the SFCW radar is adequate to track multiple subjects' motions based on their range bins;

Results agreed very well with the ground truth (Boulic model), though slight degradation was observed. This degradation is related to multipath and mutual coupling effects created by the two subjects being close in the scene; The most difficult challenge in indoor environments is the multipath effect.

In dark or from behind the wall we recognize static human subjects from other static background using mean subtraction, due to the vital signs;

Moreover, I developed mono-static SFCW radar configuration and real time demo for vital sign detection, successfully.

8.1 Accomplishments

1) I was able to build an optical system using two cameras and used iPPG signals from the two small and light cameras to retrieve human vital signs including HR, RR, SpO_2, and BP. I conducted many exhaustive experiments in indoor laboratory environment to validate

the system and develop signal processing algorithms for accurate HR, RR, and SpO_2 detection. Algorithms required the empirical constant coefficients for BP and SpO_2 calibration.

2) I extended the system to be robust and addressed its sensitivity upon using different wavelengths and new band-pass filters to extract SpO_2 accurately.

3) I investigated the feasibility of BP extraction using 60-GHz radars first that was not practical as it required using blood samples, then I initiated experiments to extract BP using two cameras which is promising and could be a good candidate for non-contact detection of BP.

4) I compared results from the optical system to results obtained by a SFCW radar system with a PRF of 20 Hz that were conducted with different human subjects for various situations. Results were published in collaboration with Dr. Ren who led the SFCW radar development.

5) Upon figuring out that we needed a higher performance SFCW radar, I developed a SFCW radar system with 200 Hz, an order of magnitude improvement. I was able to retrieve the fast moving components of the human body.

6) In collaboration with MITLL, I implemented 1-D block algorithm on a 2-D data matrix collected using the high-performance SFCW radar system for detecting a walking subject. The enhanced Hankel matrices were formed using the 2-D data set and the gait features of various body components including slow-moving and fast-moving ones were retrieved for a single- and multi-subject motion scenarios with a good accuracy.

7) Then, I utilized the high performance SFCW to retrieve human vital signs including HR and RR with higher accuracy for multi-subjects. The results are very promising and the used method used for multi-subject vital sign detection scenario have been very successful as well.

8) Recognizing orientation of the subject with respect to the radar and the high-performance SFCW radar system, I reconfigured the radar system to be utilized as a MIMO system with one transmitting and four receiving channels to address the aiming problem. The initial results of applying MRC are promising and validated the hardware performance.

9) Besides, I developed mono-static wideband SFCW radar configuration utilizing only one antenna for transmitting and receiving SFCW signal simultaneously, and a near real-time demo for human vital sign detection using the high-performance SFCW radar system.

8.2 List of Publications

8.2.1 Journal Papers

- **F. Foroughian,** F. Quaiyum, P. Theilmann, B. Ghajari, J. E. Piou, O. Kilic, and A. E. Fathy, "Non-Contact Multi-Subject Human Gait Analysis using A State-Space Method with Enhanced 1-D Block Representation," accepted for publication in *IEEE Journal of Electromagnetics, RF, and Microwaves in Medicine and Biolog,* September 2020 [5.2].

- L. Ren, N. Tran, **F. Foroughian,** K. Naishadham, J. E. Piou, O. Kilic, A. E. Fathy, "Short-Time State-Space Method for Micro-Doppler Identification of Walking Subject using UWB Impulse Doppler Radar," *IEEE Transactions on Microwave Theory and Techniques,* vol. 66, no. 7, pp. 3521 - 3534, 2018 [3.15].

- L. Ren, L. Kong, **F. Foroughian,** H. Wang, P. Theilmann, A. E. Fathy, "Comparison Study of Noncontact Vital Signs Detection Using a Doppler Stepped-Frequency Continuous-Wave Radar and Camera-Based Imaging Photoplethysmography," *IEEE Transactions on Microwave Theory and Techniques*, vol. 65, no. 9, pp. 3519 - 3529, 2017 [2.11].

8.2.2 Conference Papers

- **F. Foroughian,** and A. E. Fathy, "Wideband Leakage Cancellation Network for Monostatic Continuous-Wave Radars," *National Radio Science Meeting,* Boulder, CO, 2019 [2.30].

- A. E. Fathy, O. Kilic, L. Ren, N. Tran, T. Vo Dai, **F. Foroughian,** and F. Quaiyum, "Continuous Long Term Patient Motion Monitoring Using Ultra Wide Band Radar," *IEEE International Symposium on Antennas and Propagation & USNC/URSI National Radio Science Meeting,* Boston, MA, 2018 [8.1].

- **F. Foroughian,** C. J. Bauder, P. T. Theilmann, A. E. Fathy, "The Wavelength Selection for Calibrating Non- Contact Detection of Blood Oxygen Saturation using Imaging Photoplethysmography," *National Radio Science Meeting,* Boulder, CO, 2018 [2.8].

- F. Quaiyum, L. Ren, S. Nahar, **F. Foroughian,** A. E. Fathy, "Development of a Reconfigurable Low Cost Multi-Mode Radar System for Contactless Vital Signs Detection," *2017 IEEE MTT-S International Microwave Symposium (IMS),* Honolulu, HI, pp. 1245 – 1247, 2017 [8.2].

8.2.3 Other Journal and Conference Publications

Journal: - F. Tamjid, **F. Foroughian,** C. M. Thomas, A. Gahramani, and A. E. Fathy "Towards High Performance Wideband GNSS Antennas-Design Tradeoffs and Development of Wideband Feed Network Structures," *IEEE Transactions on Antennas and Propagation,* vol. 68, no. 8, pp. 5796 - 5806, 2020 [8.3].

Conference: - F. **Foroughian,** A. Ghahremani, A. E. Fathy, "Flexible RF-Antennas Coated by a Super Hydrophobic Paint for Minimal Water Absorption," *2016 IEEE International Symposium on Antennas and Propagation (APSURSI),* Fajardo, Puerto Rico, pp. 1947 - 1948, 2016 [8.4].

8.3 Future Works

In order to extract human BP accurately, as mentioned in Chapter Two, many improvements needed to be done to significantly increase the accuracy and robustness of this technique. Like, there is a need to include a much larger number of subjects to be evaluated in order to extract unique calibration coefficients, b and γ values, for both SBP and DBP. So, there is a need to conduct many exhaustive experiments with different subjects to extract calibration coefficients with more accuracy.

For human gait analysis, for example, we need to enhance and speed the motion classification using machine learning methods to speed up extracting the model order and block size selection while sustaining high accuracy. Another hurdle is multi-path impact specially in multi-subject scenarios, we need to further study ways to reduce this adverse effect. In addition, we are still shooting to develop algorithms that can extend human gait

features retrieval for other different motions such as hand gesturing like motions to control the computer system instead of using mouse, keypad, or touching the screen.

Another open problem is detecting human vital signs when the subject is walking or moving. Preliminary efforts to detect vital signs for walking subject were not successful even though early on we were able to discern vital signs in the presence of tiny body random motion.

Definitely, the trend nowadays to develop portable radar systems upon utilizing mm-Wave radars. Many FMCW and even impulse radars have been developed on chips and can be used for vital signal analysis. Although we used the 1-D block and other signal processing schemes on the data collected from SFCW radar system with 2-4 GHz operating frequency, these algorithms can be easily used to analyze to the data collected using the mm-wave systems or UWB impulse chips with very small sizes and light weight as well.

LIST OF REFERENCES

[1.1] L. Kong et al., "Non-contact detection of oxygen saturation based on visible light imaging device using ambient light," *Opt. Exp.*, vol. 21, no. 15, pp. 17464–17471, 2013.

[1.2] M. Kumar, A. Veeraraghavan, and A. Sabharwal, "DistancePPG: Robust non-contact vital signs monitoring using a camera," *Biomed. Opt. Exp.*, vol. 6, no. 5, pp. 1565–1588, 2015.

[1.3] C. Li, V. M. Lubecke, O. Boric-Lubecke, and J. Lin, "A review on recent advances in Doppler radar sensors for noncontact healthcare monitor- ing," *IEEE Trans. Microw. Theory Techn.*, vol. 61, no. 5, pp. 2046–2060, May 2013.

[1.4] J. Tu, T. Hwang, and J. Lin, "Respiration rate measurement under 1-D body motion using single continuous-wave Doppler radar vital sign detection system," *IEEE Trans. Microw. Theory Techn.*, vol. 64, no. 6, pp. 1937–1946, Jun. 2016.

[1.5] C. Li and J. Lin, "Random body movement cancellation in Doppler radar vital sign detection," *IEEE Trans. Microw. Theory Techn.*, vol. 56, no. 12, pp. 3143–3152, Dec. 2008.

[1.6] C. Gu, G. Wang, Y. Li, T. Inoue, and C. Li, "A hybrid radar-camera sensing system with phase compensation for random body movement cancellation in Doppler vital sign detection," *IEEE Trans. Microw. Theory Techn.*, vol. 61, no. 12, pp. 4678–4688, Dec. 2013.

[1.7] H.-C. Kuo et al., "A fully integrated 60-GHz CMOS direct-conversion Doppler radar RF sensor with clutter canceller for single-antenna noncontact human vital-signs detection," *IEEE Trans. Microw. Theory Techn.*, vol. 64, no. 4, pp. 1018–1028, Apr. 2016.

[1.8] T.-Y. J. Kao, Y. Yan, T.-M. Shen, A. Y.-K. Chen, and J. Lin, "Design and analysis of a 60-GHz CMOS Doppler micro-radar system-in-package for vital-sign and vibration detection," *IEEE Trans. Microw. Theory Techn.*, vol. 61, no. 4, pp. 1649–1659, Apr. 2013.

[1.9] H.-R. Chuang, H.-C. Kuo, F.-L. Lin, T.-H. Huang, C.-S. Kuo, and Y.-W. Ou, "60-GHz millimeter-wave life detection system (MLDS) for noncontact human vital-signal monitoring," *IEEE Sensors J.*, vol. 12, no. 3, pp. 602–609, Mar. 2012.

[1.10] M.-C. Huang, J. J. Liu, W. Xu, C. Gu, C. Li, and M. Sarrafzadeh, "A self-calibrating radar sensor system for measuring vital signs," *IEEE Trans. Biomed. Circuits Syst.*, vol. 10, no. 2, pp. 352–363, Apr. 2016.

[1.11] L. Chioukh, H. Boutayeb, D. Deslandes, and K. Wu, "Noise and sensitivity of harmonic radar architecture for remote sensing and detection of vital signs," *IEEE Trans. Microw. Theory Techn.*, vol. 62, no. 9, pp. 1847–1855, Sep. 2014.

[1.12] P.-H. Wu, J.-K. Jau, C.-J. Li, T.-S. Horng, and P. Hsu, "Phase- and self- injection-locked radar for detecting vital signs with efficient elimination of DC offsets and null points," *IEEE Trans. Microw. Theory Techn.*, vol. 61, no. 1, pp. 685–695, Jan. 2013.

[1.13] F.-K. Wang, T.-S. Horng, K.-C. Peng, J.-K. Jau, J.-Y. Li, and C.-C. Chen, "Single-antenna Doppler radars using self and mutual injection locking for vital sign

detection with random body movement cancellation," *IEEE Trans. Microw. Theory Techn.,* vol. 59, no. 12, pp. 3577–3587, Dec. 2011.

[1.14] G. Vinci et al., "Six-port radar sensor for remote respiration rate and heartbeat vital-sign monitoring," IEEE Trans. Microw. Theory Techn., vol. 61, no. 5, pp. 2093–2100, May 2013.

[1.15] B.-K. Park, O. Boric-Lubecke, and V. M. Lubecke, "Arctangent demodulation with DC offset compensation in quadrature Doppler radar receiver systems," *IEEE Trans. Microw. Theory Techn.,* vol. 55, no. 5, pp. 1073–1079, May 2007.

[1.16] M. Baboli, A. Singh, N. Hafner, and V. Lubecke, "Parametric study of antennas for long range Doppler radar heart rate detection," in *Proc. IEEE Annu. Int. Conf. Eng. Med. Biol. Soc. (EMBC),* Aug. 2012, pp. 3764–3767.

[1.17] Y. Wang, Q. Liu, and A. E. Fathy, "CW and pulse—Doppler radar processing based on FPGA for human sensing applications," *IEEE Trans. Geosci. Remote Sens.,* vol. 51, no. 5, pp. 3097–3107, May 2013.

[1.18] B. Schleicher, I. Nasr, A. Trasser, and H. Schumacher, "IR-UWB radar demonstrator for ultra-fine movement detection and vital-sign monitor- ing," *IEEE Trans. Microw. Theory Techn.,* vol. 61, no. 5, pp. 2076–2085, May 2013.

[1.19] A. Lazaro, D. Girbau, and R. Villarino, "Analysis of vital signs mon- itoring using an IR-UWB radar," *Prog. Electromagn. Res.,* vol. 100, pp. 265–284, 2010.

[1.20] A. Nezirovic, A. G. Yarovoy, and L. P. Ligthart, "Signal processing for improved detection of trapped victims using UWB radar," *IEEE Trans. Geosci. Remote Sens.,* vol. 48, no. 4, pp. 2005–2014, Apr. 2010.

[1.21] S. Wang et al., "A novel ultra-wideband 80 GHz FMCW radar system for contactless monitoring of vital signs," in *Proc. IEEE 37th Annu. Int. Conf. Eng. Med. Biol. Soc. (EMBC),* Aug. 2015, pp. 4978–4981.

[1.22] G. Wang, C. Gu, T. Inoue, and C. Li, "A hybrid FMCW-interferometry radar for indoor precise positioning and versatile life activity mon- itoring," *IEEE Trans. Microw. Theory Techn.,* vol. 62, no. 11, pp. 2812–2822, Nov. 2014.

[1.23] G. Wang, J.-M. Muñoz-Ferreras, C. Gu, C. Li, and R. Gómez-García, "Application of linear-frequency-modulated continuous-wave (LFMCW) radars for tracking of vital signs," *IEEE Trans. Microw. Theory Techn.,* vol. 62, no. 6, pp. 1387–1399, Jun. 2014.

[1.24] M. Mercuri et al., "Optimized SFCW radar sensor aiming at fall detection in a real room environment," in *Proc. IEEE Topical Conf. Biomed. Wireless Technol., Netw., Sens. Syst. (BioWireleSS),* Jan. 2013, pp. 4–6.

[1.25] M. Mercuri et al., "Analysis of an indoor biomedical radar-based system for health monitoring," *IEEE Trans. Microw. Theory Techn.,* vol. 61, no. 5, pp. 2061–2068, May 2013.

[1.26] L. Ren, H. Wang, K. Naishadham, Q. Liu, and A. E. Fathy, "Non-invasive detection of cardiac and respiratory rates from stepped frequency continuous wave radar measurements using the state space method," in *IEEE MTT-S Int. Microw. Symp. Dig.,* May 2015, pp. 1–4.

[1.27] L. Liu and S. Liu, "Remote detection of human vital sign with stepped- frequency continuous wave radar," *IEEE J. Sel. Topics Appl. Earth Observ. Remote Sens.,* vol. 7, no. 3, pp. 775–782, Mar. 2014.

[1.28] H. Wang et al., “An elegant solution: An alternative ultra-wideband transceiver based on stepped-frequency continuous-wave operation and compressive sensing,” *IEEE Microw. Mag.,* vol. 17, no. 7, pp. 53–63, Jul. 2016.
[1.29] D. H. Sutherland, “The evolution of clinical gait analysis part I: Kinesiological EMG,” *Gait Posture,* vol. 14, no. 1, 2001, pp. 61–70.
[1.30] D. H. Sutherland, “The evolution of clinical gait analysis Part II kinematics,” *Gait Posture,* vol. 16, no. 2, 2002, pp. 159–179.
[1.31] D. H. Sutherland, “The evolution of clinical gait analysis part III—kinetics and energy assessment,” *Gait Posture,* vol. 21, no. 4, 2005, pp. 447–461.
[1.32] B. Najafi, et al., “Ambulatory system for human motion analysis using a kinematic sensor: monitoring of daily physical activity in the elderly,” *IEEE Trans. Biomed. Eng.,* vol. 50, no. 6, pp. 711-723, June 2003.
[1.33] J. K. Aggarwal, Q. Cai, “Human Motion Analysis: A Review,” *Computer Vision and Image Understanding,* vol. 73, no. 3, 1999, pp 428-440.
[1.34] Y. Wahab, N. A. Bakar, “Gait Analysis Measurement for Sport Application Based on Ultrasonic System,” *Proceedings of 2011 IEEE 15th International Symposium on Consumer Electronics (ISCE),* Singapore, June 2011, pp. 20–24.
[1.35] A. Muro-de-la-Herran, B. Garcia-Zapirain, A. Mendez-Zorrilla, “Gait analysis methods: an overview of wearable and non-wearable systems, highlighting clinical applications” *Sensors (Basel, Switzerland),* 2014, 14(2), pp. 3362-3394.
[1.36] V. C. Chen, “Detection and analysis of human motion by radar,” in *Proc. IEEE Radar Conf.,* Rome, Italy, May 2008, pp. 1–4.
[1.37] A. Lin and H. Ling, “Doppler and direction-of-arrival (DDOA) radar for multiple-mover sensing,” *IEEE Trans. Aerosp. Electron. Syst.,* vol. 43, no. 4, pp. 1496–1509, Oct. 2007.
[1.38] M. Otero, “Application of a continuous wave radar for human gait recognition,” *Proc. SPIE,* vol. 5809, pp. 538–548, May 2005.
[1.39] B. G. Mobasseri and M. G. Amin, “A time-frequency classifier for human gait recognition,” Proc. SPIE, vol. 7306, pp. 730628-1–730628-9, May 2009.
[1.40] A. R. Hunt, “Use of a frequency-hopping radar for imaging and motion detection through walls,” *IEEE Trans. Geosci. Remote Sens.,* vol. 47, no. 5, pp. 1402–1408, May 2009.
[1.41] M. L. Lees, “Digital beamforming calibration for FMCW radar,” *IEEE Trans. Aerosp. Electron. Syst.,* vol. 25, no. 2, pp. 281–284, Mar. 1989.
[1.42] J. Fuchs, K. D. Ward, M. P. Tulin, and R. A. York, “Simple techniques to correct for VCO nonlinearities in short range FMCW radars,” in *IEEE MTT-S Int. Microw. Symp. Dig.,* Jun. 1996, pp. 1175–1178.

[2.1] H. S. Zhu, Y. J. Zhao, and L. Q. Dong, “Non cardiac rate based on visible light imaging device,” *Proc. SPIE 8498,* 849806-7, 2012.
[2.2] K. Humphreys, T. Ward, and C. Markham, “Noncontact simultaneous noncontact pulse oximetry,” *Rev. Sci. Instrum.,* 78(4), 044304.
[2.3] https://www.theimagingsource.com/products/industrial-cameras/usb-3.0 monochrome/dmk23u618/
[2.4] http://www.thorlabs.com/thorproduct.cfm?partnumber=SM1P1

https://www.thorlabs.com/thorproduct.cfm?partnumber=SM1A36
[2.5] http://www.thorlabs.com/newgrouppage9.cfm?objectgroup_id=1822&pn=MVL8M23#5347
[2.6] http://www.omegafilters.com/products/filters/520bp20-rapidband.html
[2.7] https://www.ti.com/product/AFE4490
[2.8] F. Foroughian, C. J. Bauder, P. T. Theilmann, A. E. Fathy, "The Wavelength Selection for Calibrating Non- Contact Detection of Blood Oxygen Satuartion using Imaging Photoplethysmography," *National Radio Science Meeting,* Boulder, CO, 2018
[2.9] M. Kumar, A. Veeraraghavan, and A. Sabharwal, "DistancePPG: robustnon-contact vital signs monitoring using a camera," *Biomed. Opt. Express,* 6(5) 1565–1488 (2015).
[2.10] A. R. Guazzi, M.Villarroel, J. Jorge, J. Daly, M. C. Frise, P. A. Robbins, and L. Tarassenko, "Non-contact measurement of oxygensaturation with n RGB camera" *Biomed. Opt. Express,* 6(9) 3320–3338 (2015).
[2.11] L. Ren, L. Kong, F. Foroughian, H. Wang, P. Theilmann, A. E. Fathy, "Comparison Study of Noncontact Vital Signs Detection Using a Doppler Stepped-Frequency Continuous-Wave Radar and Camera-Based Imaging Photoplethysmography," *IEEE Transactions on Microwave Theory and Techniques,* vol. 65, no. 9, pp. 3519 - 3529, 2017.
[2.12] I.C. Jeong, J. Finkelstein, "Introducing Contactless Blood Pressure Assessment Using a High Speed Video Camera," *J Med Syst*, 40, 77 (2016). https://doi.org/10.1007/s10916-016-0439-z.
[2.13] Ying Guo, Xiaohua Liu, Lingqin Kong, Ming Liu, Yuejin Zhao, Liquan Dong, "Non-contact continuous blood pressure measurement based on imaging equipment," *Proc. SPIE 11438, 2019 International Conference on Optical Instruments and Technology: Optoelectronic Imaging/Spectroscopy and Signal Processing Technology,* 1143802 (12 March 2020); doi: 10.1117/12.2540316.
[2.14] W. Lin, H. Wang, O. W. Samuel and G. Li, "Using a new PPG indicator to increase the accuracy of PTT-based continuous cuffless blood pressure estimation," *2017 39th Annual International Conference of the IEEE Engineering in Medicine and Biology Society (EMBC),* Seogwipo, 2017, pp. 738-741, doi: 10.1109/EMBC.2017.8036930.
[2.15] M. Yoshioka and S. Bounyong, "Regression-forests-based estimation of blood pressure using the pulse transit time obtained by facial photoplethysmogram," *2017 International Joint Conference on Neural Networks (IJCNN),* Anchorage, AK, 2017, pp. 3248-3253, doi: 10.1109/IJCNN.2017.7966262.
[2.16] N. G. Roald, "Estimation of vital signs from ambient-light non-contact photoplethysmography," 2013.
[2.17] H. Luo et al., "Smartphone-Based Blood Pressure Measurement Using Transdermal Optical Imaging Technology," *Cardiovascular Imaging,* 2019, doi: 10.1161/CIRCIMAGING.119.008857.
[2.18] Tu, Jianxuan, and Jenshan Lin. "Respiration harmonics cancellation for accurate heart rate measurement in non-contact vital sign detection." *2013 IEEE MTT-S International Microwave Symposium Digest (MTT),* IEEE, 2013.

[2.19] Ren, Lingyun, et al. "Phase-based methods for heart rate detection using UWB impulse Doppler radar." *IEEE Transactions on Microwave Theory and Techniques*, 64.10 (2016): 3319-3331.
[2.20] https://neulog.com/respiration-monitor-belt/
[2.21] https://www.sparkfun.com/products/11574
[2.22] https://www.testequipmentdepot.com/extech/light-meters/standard-light-meters/light-meter-digital-analog-display-lt300.htm?gclid=CjwKCAiAt9z-BRBCEiwA_bWv-Hauvdvr42nfJPfKpzk5NcvvCGEEsXRo7z-uaIAqSm00GkOZjfUVOxoC7MIQAvD_BwE.
[2.23] S. Magoon, A. E. Fathy, "Compact monostatic/bistatic UWB radar for wall characterization," *2014 IEEE BenMAS*, 2014, 1-3.
[2.24] H.A. Songcheol, "Quadrature radar topology with Tx leakage canceller for 24-GHz radar applications," *IEEE Trans. Microw. Theory Tech.*, 55 (2007), 1438–1444.
[2.25] K. Choul-Young, K. Jeong-Geun, D. Baek, H. Songcheol, "A circularly polarized balanced radar front-end with a single antenna for 24-GHz radar applications," *IEEE Trans. Microw. Theory Tech.*, 57 (2007), 293–297.
[2.26] L. Han Lim, L. Won-Gyu, K.-S. Oh, Y. Jong-Won, "24 GHz balanced Doppler radar front-end with Tx leakage canceller for antenna impedance variation and mutual coupling," *IEEE Trans. Antennas Propag.*, 59 (2011), 4497–4504.
[2.27] K. Jeong-Geun, K. Sangsoo, J. Sanghoon, P. Jae-Woo, H. Songcheol, "Balanced topology to cancel Tx leakage in CW radar," *IEEE Microw. Compon. Lett.*, 14 (2004), 443–445.
[2.28] M. Mercuri, P. Barmuta, P. J. Soh, P. Leroux, D. Schreurs, "Monostatic continuous-wave radar integrating a tunable wideband leakage canceler for indoor tagless localization," *International Journal of Microwave and Wireless Technologies*, 2017.
[2.29] E. Öztürk, D. Genschow, U. Yodprasit, B. Yilmaz, D. Kissinger, W. Debski, W. Winkler, "A 60 GHz SiGe BiCMOS monostatic transceiver for radar applications, " *2017 IEEE MTT-S International Microwave Symposium (IMS)*, 1408-1411.
[2.30] F. Foroughian, and A. E. Fathy, "Wideband Leakage Cancellation Network for Monostatic Continuous-Wave Radars," *National Radio Science Meeting, Boulder*, CO, 2019.
[2.31] A. Srivastava, "Cost and performance benefits of cascading single junction circulators for duplex applications," www.mpdigest.com.
[2.32] L. Chiu, Q. Xue, "A parallel-strip ring power divider with high isolation and arbitrary power-dividing ratio," *IEEE Trans. Microw. Theory Tech.*, 55 (2011), 2419-2426.

[3.1] D. Gouwanda and S. Senanayake, "Emerging trends of body-mounted sensors in sports and human gait analysis," in *4th Kuala Lumpur International Conference on Biomedical Engineering 2008*, 2008: Springer, pp. 715-718.
[3.2] L. Wang, T. Tan, H. Ning, and W. Hu, "Silhouette analysis-based gait recognition for human identification," *IEEE transactions on pattern analysis and machine intelligence*, vol. 25, no. 12, pp. 1505-1518, 2003.

[3.3] D. M. Gavrila, "The visual analysis of human movement: A survey," *Computer vision and image understanding,* vol. 73, no. 1, pp. 82-98, 1999.
[3.4] Z. Yu and Y. Nakamura, "Smart meeting systems: A survey of state-of-the-art and open issues," *ACM Computing Surveys (CSUR),* vol. 42, no. 2, p. 8, 2010.
[3.5] F. Quaiyum, N. Tran, J. E. Piou, O. Kilic, and A. E. Fathy, "Noncontact Human Gait Analysis and Limb Joint Tracking Using Doppler Radar," *IEEE Journal of Electromagnetics, RF and Microwaves in Medicine and Biology,* vol. 3, no. 1, pp. 61-70, 2018.
[3.6] https://www.microwavejournal.com/articles/28002-novelda-launches-easy-to-use-single-chip-uwb-radar.
[3.7] H. Wang, L. Ren, E. Mao, and A. E. Fathy, "Phase based motion characteristics measurement for fall detection by using stepped-frequency continuous wave radar," in *2016 IEEE Topical Conference on Biomedical Wireless Technologies,* Networks, and Sensing Systems (BioWireleSS), 2016: IEEE, pp. 43-45.
[3.8] F. Qi, H. Lv, F. Liang, Z. Li, X. Yu, and J. Wang, "MHHT-based method for analysis of micro-Doppler signatures for human finer-grained activity using through-wall SFCW radar," *Remote Sensing,* vol. 9, no. 3, p. 260, 2017.
[3.9] J. L. Geisheimer, W. S. Marshall, and E. Greneker, "A continuous-wave (CW) radar for gait analysis," in *Conference Record of Thirty-Fifth Asilomar Conference on Signals, Systems and Computers (Cat. No. 01CH37256),* 2001, vol. 1: IEEE, pp. 834-838.
[3.10] J. Niu, Y. Liu, W. Jiang, X. Li, and G. Kuang, "Weighted average frequency algorithm for Hilbert–Huang spectrum and its application to micro-Doppler estimation," *IET Radar, Sonar & Navigation,* vol. 6, no. 7, pp. 595-602, 2012.
[3.11] L. Stankovic, M. Dakovic, T. Thayaparan, and V. Popovic-Bugarin, "Inverse radon transform–based micro-Doppler analysis from a reduced set of observations," *IEEE Transactions on Aerospace and Electronic Systems,* vol. 51, no. 2, pp. 1155-1169, 2015.
[3.12] B. Godana, A. Barroso, and G. Leus, "Estimating human movement parameters using a software radio-based radar," *International Journal on Advances in Systems and Measurements,* 4 (1-2), 2011, 2011.
[3.13] T. Thayaparan, S. Abrol, E. Riseborough, L. Stankovic, D. Lamothe, and G. Duff, "Analysis of radar micro-Doppler signatures from experimental helicopter and human data," *IET Radar, Sonar & Navigation,* vol. 1, no. 4, pp. 289-299, 2007.
[3.14] Y. Kim and H. Ling, "Through-wall human tracking with multiple Doppler sensors using an artificial neural network," *IEEE Transactions on Antennas and Propagation,* vol. 57, no. 7, pp. 2116-2122, 2009.
[3.15] L. Ren et al., "Short-time state-space method for micro-Doppler identification of walking subject using UWB impulse Doppler radar," *IEEE Transactions on Microwave Theory and Techniques,* vol. 66, no. 7, pp. 3521-3534, 2018.
[3.16] G. Greneker, "Very low cost stand-off suicide bomber detection system using human gait analysis to screen potential bomb carrying individuals," Proc. SPIE, Radar Sensor Technology IX, May 2005.

[3.17] T. Thayaparan, L. Stanković, and I. Djurović, "Micro-Doppler-based target detection and feature extraction in indoor and outdoor environments," *Journal of the Franklin Institute,* vol. 345, no. 6, pp. 700-722, 2008.
[3.18] N. Maaref, P. Millot, C. Pichot, and O. Picon, "A study of UWB FM-CW radar for the detection of human beings in motion inside a building," *IEEE Transactions on Geoscience and Remote Sensing,* vol. 47, no. 5, pp. 1297-1300, 2009.
[3.19] B. Lu, Q. Song, Z. Zhou, and H. Wang, "A SFCW radar for through wall imaging and motion detection," in *2011 8th European Radar Conference,* 2011: IEEE, pp. 325-328.
[3.20] O. R. Fogle and B. D. Rigling, "Micro-range/micro-Doppler decomposition of human radar signatures," *IEEE Transactions on Aerospace and Electronic Systems,* vol. 48, no. 4, pp. 3058-3072, 2012.
[3.21] Y. Tang, J. Wang and C. Li, "Short-range indoor localization using a hybrid doppler-UWB system," *2017 IEEE MTT-S International Microwave Symposium (IMS),* Honololu, HI, pp. 1011-1014, 2017.
[3.22] Z. Peng, C. Li, J.-M. Muñoz-Ferreras, and R. Gómez-García, "An FMCW radar sensor for human gesture recognition in the presence of multiple targets," in *2017 First IEEE MTT-S International Microwave Bio Conference (IMBIOC),* 2017: IEEE, pp. 1-3.
[3.23] S. Abdulatif, F. Aziz, B. Kleiner, and U. Schneider, "Real-time capable micro-Doppler signature decomposition of walking human limbs," in *2017 IEEE Radar Conference (RadarConf),* IEEE, pp. 1093-1098, 2017.
[3.24] K. Naishadham and J. E. Piou, "A novel 1-D block processing approach to 2-D NMR spectroscopy," in *2007 4th IEEE International Symposium on Biomedical Imaging: From Nano to Macro,* 2007: IEEE, pp. 1352-1355.
[3.25] R. G. Raj, V. C. Chen and R. Lipps, "Analysis of radar human gait signatures," in *IET Signal Processing,* vol. 4, no. 3, pp. 234-244, June 2010.
[3.26] R. Roy, T. Kailath, "ESPRIT – Estimation of Signal Parameters via Rotational Invariance Techniques," *IEEE Transactions on Acoustics, Speech, and Signal Processing,* Vol. ASSP–37, 1989, pp. 984–995.

[4.1] Ridenour,"Radar System Engineering", *MIT Radiation Lab series,* vol 1, year 1947, page 629.
[4.2] J. M. Garcia-Rubia, O. Kilic, V. Dang, Q. M. Nguyen, and N. Tran, "Analysis of moving human micro-Doppler signature in forest environments," *Progress In Electromagnetics Research,* vol. 148, pp. 1-14, 2014.
[4.3] ADF4152HV PLL Datasheet from Analog Device. Link: https://www.analog.com/media/en/technical-documentation/data sheets/ADF4152HV.pdf.
[4.4] DCYS200400-5 VCO Datasheet from Synergy Microwave Corporations. Link: https://synergymwave.com/products/vco/datasheet/DCYS200400-5.pdf.
[4.5] D. Banerjee, "PLL Fundamentals, Part 2: PLL Behavior", Texas Instruments Literature Number: SNAP002.
[4.6] D. Banerjee, "PLL Fundamentals, Part 3: PLL Design", Texas Instruments Literature Number: SNAP003.

[4.7] https://form.analog.com/Form_Pages/RFComms/ADISimPll.aspx.
[4.8] https://www.mccdaq.com/pdfs/manuals/USB-205.pdf.
[4.9] F. Gardner, "A BPSK/QPSK timing-error detector for sampled receivers," IEEE Transactions on communications, vol. 34, no. 5, pp. 423-429, 1986.
[4.10] M. Mercuri, "Development of Contactless Health Monitoring Sensors and Integration in Wireless Sensor Networks," *Ph.D. Dissertation,* KU Leuven, 2015.

[5.1] J. M. Garcia-Rubia, O. Kilic, V. Dang, Q. M. Nguyen, and N. Tran, "Analysis of moving human micro-Doppler signature in forest environments," *Progress In Electromagnetics Research,* vol. 148, pp. 1-14, 2014.
[5.2] F. Foroughian, F. Quaiyum, P. Theilmann, B. Ghajari, J. E. Piou, O. Kilic, and A. E. Fathy, "Non-Contact Multi-Subject Human Gait Analysis using A State-Space Method with Enhanced 1-D Block Representation," accepted for publication in *IEEE Journal of Electromagnetics, RF, and Microwaves in Medicine and Biolog,* September 2020.
[5.3] J. E. Piou, "A state identification method for 1-D measurements with gaps," in *Proc. AIAA Guid., Navigat., Control Conf. Exhib.,* pp. 1–11, 2005.
[5.4] K. Naishadham and J. E. Piou, "A robust state space model for the characterization of extended returns in radar target signatures," *IEEE Trans. Antennas Propag.,* vol. 56, no. 6, pp. 1742–1751, Jun. 2008.
[5.5] H. Bozdogan, "Model selection and Akaike's information criterion (AIC): The general theory and its analytical extensions," *Psychometrika,* vol. 52, no. 3, pp.345-370, 1987.
[5.6] S. Wang, F. Qi, and H. Li, "Minimum description length shape model based on elliptic fourier descriptors," in *International Symposium on Neural Networks (pp. 646-651). Springer,* Berlin, Heidelberg, 2006.

[6.1] https://www.videograbber.net/motion-tracking-software.html.
[6.2] J.M. Muñoz-Ferreras, F. Pérez-Martínez, "Subinteger Range-Bin Alignment Method for ISAR Imaging of Noncooperative Targets," *EURASIP J. Adv. Signal Process.,* 438615, pp. 1-16, 2010.
[6.3] B. D. Rao, "Sensitivity considerations in state space model-based harmonic retrieval methods," *IEEE Trans. Acoust. Speech Signal Process.,* vol. 37, no. 11, pp. 1789–1794, Nov. 1989.
[6.4] Y. Hua and T. K. Sarkar, "Matrix pencil method and its performance," in *Proc. IEEE Int. Conf. Acoust. Speech Signal Process. (ICASSP),* Apr.1988, pp. 2476–2479.
[6.5] Y. Hua and T. K. Sarkar, "On SVD for estimating generalized eigenvalues of singular matrix pencil in noise," *IEEE Trans. Acoust. Speech Signal Process.,* vol. ASSP-39, no. 4, pp. 892–900, Apr. 1991.

[7.1] Sakamoto, Takuya. "Noncontact Measurement of Human Vital Signs during Sleep Using Low-power Millimeter-wave Ultrawideband MIMO Array Radar." *2019 IEEE MTT-S International Microwave Biomedical Conference (IMBioC),* Vol. 1. IEEE, 2019.

[8.1] A. E. Fathy, O. Kilic, L. Ren, N. Tran, T. Vo Dai, F. Foroughian, and F. Quaiyum, “Continuous Long Term Patient Motion Monitoring Using Ultra Wide Band Radar,” *IEEE International Symposium on Antennas and Propagation & USNC/URSI National Radio Science Meeting,* Boston, MA, 2018.

[8.2] F. Quaiyum, L. Ren, S. Nahar, F. Foroughian, A. E. Fathy, “Development of a Reconfigurable Low Cost Multi-Mode Radar System for Contactless Vital Signs Detection,” *2017 IEEE MTT-S International Microwave Symposium (IMS),* Honolulu, HI, pp. 1245 – 1247, 2017.

[8.3] F. Tamjid, F. Foroughian, C. M. Thomas, A. Gahramani, and A. E. Fathy “Towards High Performance Wideband GNSS Antennas-Design Tradeoffs and Development of Wideband Feed Network Structures,” *IEEE Transactions on Antennas and Propagation,* vol. 68, no. 8, pp. 5796 - 5806, 2020.

[8.4] F. Foroughian, A. Ghahremani, A. E. Fathy, “Flexible RF-Antennas Coated by a Super Hydrophobic Paint for Minimal Water Absorption,” *2016 IEEE International Symposium on Antennas and Propagation (APSURSI),* Fajardo, Puerto Rico, pp. 1947 - 1948, 2016.

VITA

Farnaz Foroughian was born in Tehran, Iran, in 1984. She received her B.Sc. degree in Electrical Engineering from Technical and Vocational University (Dr. Shariaty College) in 2007 and her M.Sc. degree in Electrical Engineering from Amirkabir University of Technology (Tehran Polytechnic) in 2012. She joined the University of Tennessee, Knoxville in August 2015. She is studying toward her Ph.D. degree in Electrical Engineering at the University of Tennessee, Knoxville, with expected completion date in December 2020. She was an RF and EMC Intern with Intel Corporation in Hillsboro, OR from May 2020 to November 2020. She has authored or coauthored numerous journal/conference papers and has presented at numerous international conferences.

Mrs. Foroughian was the recipient of the EECS Department Excellence Fellowship Award in August 2015, Excellence in Graduate Student Teaching Award for Extraordinary Performance in Teaching in 2019, Gonzalez Family Award for Outstanding Graduate Teaching Assistant in 2019, and EECS Department One-Time Fellowship Award in 2020, at the University of Tennessee, Knoxville. She was also the recipient of the Chancellor's Citation Award for Extraordinary Professional Promise, in the years 2018, 2019 and 2020 from the University of Tennessee, Knoxville.